Theses and Dissertations

Spring 2010

Spectroscopic evidence for interfacial Fe(II)-Fe(III) electron transfer in clay minerals

Michael Vernon Schaefer

University of Iowa

Recommended Citation

Schaefer, Michael Vernon. "Spectroscopic evidence for interfacial Fe(II)-Fe(III) electron transfer in clay minerals." MS (Master of Science) thesis, University of Iowa, 2010.
https://doi.org/10.17077/etd.jw0wyhrq.

SPECTROSCOPIC EVIDENCE FOR INTERFACIAL FE(II)-FE(III) ELECTRON TRANSFER IN CLAY MINERALS

by

Michael Vernon Schaefer

A thesis submitted in partial fulfillment of the
requirements for the Master of Science
degree in Civil and Environmental Engineering
in the Graduate College of
The University of Iowa

May 2010

Thesis Supervisor: Associate Professor Michelle M. Scherer

Graduate College
The University of Iowa
Iowa City, Iowa

CERTIFICATE OF APPROVAL

_____

MASTERS THESIS

_____

This is to certify that the Masters thesis of

Michael Vernon Schaefer

has been approved by the Examining Committee
for the thesis requirement for the Master of Science
degree in Civil and Environmental Engineering at the May 2010
graduation.

Thesis Committee: _____
                       Michelle M. Scherer, Thesis Supervisor

                _____
                       Gene F. Parkin

                _____
                       Craig L. Just

To my parents for providing a stable, healthy foundation

To learn to see below the surface,
You must adjust your altitude

Robbie Robertson, *The Saga of Pepote Rouge*

ACKNOWLEDGMENTS

When I was a sophomore and decided to switch to civil engineering, I was assigned a new academic advisor, Professor Wu. When I went to meet with him, the first thing he told me was that he was retiring and I should ask for a different advisor. Soon I had been assigned Michelle Scherer. How fortunate for me she gave me a job and let me keep coming back for the next four years. Michelle, you have taught me many things through your example, most importantly what is important in science and in many cases life.

The basis of any laboratory know-how I have is from the opportunity to work with David Cwiertny and Robert Handler. I was fortunate enough to work with and learn from them for most of my time in the lab. Additionally, Chris Gorski entertained me with various challenges involving pennies and foam balls, amongst other things. Later he held my hand learning about Mössbauer spectroscopy. If not for all of the great students in the Scherer lab I know I would not have continued studying iron for four years (and beyond), no matter how interesting it is!

Another special thanks to the two other members of my thesis committee, Gene Parkin and Craig Just. Gene, I took every environmental engineering class at Iowa with you, and you tempted me into environmental engineering even if you couldn't persuade me into bacteria. Craig, you have helped me learn how I can actually use this knowledge I am getting to effect some good change in the world.

Finally, the biggest thanks to my family, who have always shown me unconditional love and support.

ABSTRACT

Although interfacial electron transfer has been shown to occur for sorbed Fe(II) and Fe(III)-oxides, it is unclear if a similar reaction occurs between sorbed Fe(II) and Fe(III)-bearing clay minerals. Here, we use the isotope specificity of ^{57}Fe Mössbauer spectroscopy to demonstrate electron transfer between sorbed Fe(II) and structural Fe(III) in a nontronite clay mineral (NAu-2). Appearance of an Fe(II) doublet in the NAu-2 spectra after reaction with aqueous ^{56}Fe(II) (^{56}Fe is transparent in Mössbauer spectra) provided evidence for reduction of structural Fe(III). Mössbauer spectra using enriched ^{57}Fe(II) reveal that Fe(II) is oxidized upon sorption to NAu-2, and the oxidation product of this reaction is a ferric oxide with spectral parameters similar to lepidocrocite. The reduction of structural Fe(III) by Fe(II) induces electron delocalization in the clay structure, which we observe by variable-temperature Mössbauer spectra and macroscopic color change indicative of Fe(II)-Fe(III) pairs. The extent of structural Fe(III) reduction in NAu-2 is equal to the amount of Fe(II) sorbed until approximately 15% reduction, after which point reduction is no longer concomitant with the amount of sorbed Fe(II).

TABLE OF CONTENTS

LIST OF TABLES

LIST OF FIGURES

xiii

CHAPTER I. INTRODUCTION

Iron In The Environment

Iron (Fe) is one of the most important reactants in the environment due to its abundance and ability to exist in different oxidation states under environmental conditions. Iron is the most abundant element in the earth and the fourth most abundant in the earth's crust [1]. It commonly exists in the 0, +II, and +III oxidation states, and the Fe(II)/Fe(III) (ferrous/ferric) aqueous standard reduction potential is +0.77 V. Because this reduction potential is approximately midway between common environmental standard reduction potentials (-1.1 to +1.8 V), both ferrous and ferric Fe are commonly found in the environment [2]. Further, redox conditions in the environment often fluctuate around the ferrous/ferric couple, leading to conditions where Fe can easily change its oxidation state. This property has the effect of providing a "redox buffer" in aquatic systems with high Fe contents (e.g. Fe-rich aquifers).

Iron in Clay Minerals

Fe is the fourth most abundant element in the earth's crust; the three more abundant elements are aluminum (Al), silicon (Si), and oxygen (O). Quartz (SiO_2) and other silicate minerals, which are typically composed of Si bonded to O in various coordinations (i.e. bonding arrangements), make up the majority of the earth's crust. Al-substitution for Si is common, as is Fe-substitution. As a result, Fe-bearing primary minerals (e.g. olivine, pyroxene) compose approximately 20% of the earth's crust, and these minerals are chiefly silicate minerals [2]. In primary minerals, Fe generally exists in the +II oxidation state [2]. More relevant from an environmental chemistry point of view are the secondary clay minerals, which make up 4-5% of the earth's crust and are generally classified into three different layer silicate (sheets structures dominated by silicate bonded to oxygen) groups: illites, kaolins, and smectites. Of these, illite generally has the highest Fe content and kaolin the lowest; however, smectites can also have appreciable Fe contents [2]. These minerals dominate the pedosphere, the interface

between the lithosphere and atmosphere, hydrosphere and biosphere, essentially the human environment.

The focus here is restricted to the study of smectites. Smectites are a group of phyllosilicates that exhibit a layer charge between 0.2 and 0.6 units per half unit cell. They are perhaps best-known for their high swellability [3], which is the cause of most unstable building foundations and even have influence on some natural hazards such as landslides. Smectites also exhibit high specific surface area and cation exchange capacity (CEC) due to their small primary particle size. As with all phyllosilicates, smectites have a layer sheet structure based on linked Si or Al tetrahedra. In smectites, these tetrahedrally-coordinated sheets can also be linked to octahedrally-coordinated Al, which is often substituted by other cations such as Fe(III). 1:1 smectites have one tetrahedral sheet linked to one octahedral sheet, while 2:1 smectites have one octahedral sheet sandwiched between two tetrahedral sheets (Figure 1.1). 2:1 smectites occur stacked on top of one another, where interlayer cations balance the negative layer charge. When water or more strongly hydrated cations are substituted in this interlayer, 2:1 smectites can swell to occupy a volume much larger than their dehydrated volume; interlayer cations can have a great effect on macroscopic swelling properties of clays [4], as can the oxidation state of Fe [5].

Smectites are ubiquitous, and occur readily in diverse environments such as soils, aquatic sediments, and non-marine weathering environments [3]. Their ubiquity can be traced to their non-specific formation processes—smectites form from weathering of a variety of primary minerals and can also directly crystallize from geologic solutions [3].

It is worth mentioning that both dioctahedral and trioctahedral smectites occur. Given a unit cell containing three octahedrally-coordinated atoms in a clay, trioctahedral identifies clays where the charge on the central atom in the octahedra is such that all three spaces are occupied in order to satisfy charge balance. Dioctahedral means that the positive charge of the octahedrally-coordinated atom is larger, and thus only 2/3 octahedra are occupied to achieve charge balance. This nomenclature is somewhat

confusing given the example of Fe, where Fe(III) clays are dioctahedral and Fe(II) clays are trioctahedral, since the lower positive charge on Fe(II) requires more atoms to fill the octahedral sites to balance the negative charge.

Here the focus is on 2:1 dioctahedral smectites. Figure 1.2 provides the classification of different compositions of this series. Nontronite is the end-member of this series with complete tetrahedral substitution by Al and complete octahedral substitution by Fe(III), and is the focus of this study. In some nontronites, Fe(III) can also substitute in the tetrahedral layer [6-8]. NAu-2 is a reference nontronite from the Uley Mine in Australia and is used throughout the following study [9].

<u>Interfacial Electron Transfer</u>

The Fe(II)/Fe(III) redox couple plays an important role in environmental cycling of electrons, and thus trace elements (e.g. arsenic and uranium), carbon, and nutrients (e.g. phosphorus and nitrogen). Although oxidation state markedly changes the reactivity of Fe, changes in bonding and coordination also determine how it reacts in the environment. An important example of this is that adsorption of Fe(II) to mineral surfaces can lower the reduction potential of the Fe(II) [2]. What this means from an environmental standpoint is that Fe(II) adsorbed to mineral surfaces may be capable of reducing species it is unable to reduce in aqueous solution. Further, Fe(II) atoms adsorbed to adjacent surface sites may contact contaminants in ways that allow multiple (2+) electron transfers for the same species, extending the reactivity of Fe(II) to contaminants that require more than one electron transfer step [2].

Recently, it has been demonstrated that Fe(II) sorption onto Fe-oxides does not produce a stable Fe(II) surface species, but rather interfacial Fe(II)-Fe(III) electron transfer occurs [10]. Subsequent work has shown that electron transfer involves sorption, transfer of an electron into bulk material, and reductive dissolution of the bulk material—this effectively allows mineral turnover on the order of 30 days to occur in goethite [11]. Combined with observations of preferential face dissolution and reprecipitation on hematite [12], the prevailing idea is of an "electron conveyor belt" that is certainly not consistent with stable Fe(II) sorption onto Fe-oxide surfaces, and

thus also inconsistent with traditional surface complexation modeling (SCM). Fe(II)-Fe(III) charge transfer has been speculated to also occur for clay minerals [13], but current literature still uses SCM to describe Fe(II) sorption to Fe-bearing clay minerals [13, 14].

Interaction of Clays and Environmental Contaminants

Clays are ubiquitous, and in many subsurface environments control the transport of environmental contaminants due to their relatively high surface areas, and thus sorption capacities. Fe-rich clays additionally provide the potential to transform contaminants under reducing conditions through reaction with clay-associated Fe(II)[15]. It has been shown that not all "clay Fe(II)" is equal, but rather that at least in the case of nitroaromatic compound reduction structural Fe(II) is reactive while ion exchanged Fe(II) is not [15]. Since Fe can exist in and on clay minerals, as well is in solution surrounding them in reduced subsurface environments, it is pertinent to examine what role Fe(II) plays in the overall process of contaminant fate and transport in the environment. Clay minerals are also used in the design of radioactive waste confinement facilities, where long-term feasibility studies must account for flux of Fe(II) as a container corrosion product into the containment clay.

Hofstetter *et al.* studied the reactivity of reduced clay minerals toward nitroaromatic compounds (NACs) by exchanging different clay sites (ion exchanged, surface hydroxyl complexed) with Fe(II) or by reducing structural Fe(III) to Fe(II) by dithionite [15]. They were cleverly able to selectively exchange sites with Fe(II) by first saturating clay surfaces with either more weakly hydrated (e.g. K^+ or NH_4^+) or more strongly hydrated (e.g. Na^+, Mg^{2+}, Ca^{2+}) cations. The sorption of different cations to the basal siloxane surface changes the sorption properties, or "access" of NACs to the clay. Various cations were sorbed and used in combination with two NAC isomers. "Sorbing" NAC, 4-acetyl nitrobenzene, is planar and has a high affinity for basal sites, readily sorbing to the basal plane. "Non-sorbing" NAC, 2-acetyl nitrobenzene, does not show preference for any specific site due to diminished coplanarity arising from ortho substitution of the NO_2 group. In this way, different combinations of sorbing or

nonsorbing NACs could be used to probe the reactivity of Fe(II) exchanged on different clay sites. Further, a synthetic clay devoid of structural Fe(III) was used to eliminate structural Fe in some reactors. The conclusion of this work was that basal surface-bound (or ion exchanged) Fe(II) was not reactive toward NACs, while edge or OH-complexed and structural Fe(II) were reactive, reducing NACs to aniline end products (complete reduction of the NO_2 group to NH_2).

Subsequent work by Hofstetter's group used the same sorbing and nonsorbing isomers of acetylnitrobenzene to show that electron transfer between NACs and structural Fe(II) occurs predominantly through the basal siloxane plane (the plane of apical oxygens in the layer silicate structure), and that octahedral Fe(II) is the most reactive Fe(II) species toward NAC reduction [16]. Further work also suggested that two different Fe(II) sites exist after reduction of structural Fe in smectite as evidenced by biphasic reduction kinetics of NACs, and that the NAC reduction rates differ by three orders of magnitude between the sites [17]. They further showed in this work that a minimum Fe content, or threshold, exists to develop highly reactive Fe(II) sites [17]. The Fe(II) sites that do develop in the low-Fe clay exhibit pseudo-first order kinetics and are even less reactive than either of the two previously mentioned sites [17]. Extending their work, this group also investigated reduction of polychlorinated alkanes and concluded that the alkanes were reduced by the reduction kinetics were again biphasic (indicating two distinct Fe(II) sites), but that smectite Fe(II) is likely an important reductant towards alkanes only after Fe(III) oxides have been reductively dissolved [18].

An earlier study of 4-Cl-nitrobenzene reduction by Fe(II) sorbed onto nontronite showed a rather strong pH-dependence for both Fe(II) sorption extent and NAC reduction kinetics [19]. A model argued for two distinct surface sites, S1 and S2 sites, where the S2 site was only available for sorption above about pH 7. Additionally, the FeOH$^+$ ion was suggested to be a major source of reducing potential above pH 7.5, and the authors argue that it is the most effective reductant for 4-Cl-nitrobenzene of the three Fe(II) species.

Another interesting study on the role of Fe-bearing clay minerals provided evidence for clay-catalyzed conversion of pentachlorophenol (PCP) to octachlorodibenzodioxin (OCDD) under environmental conditions [20]. Such a conversion was explained through a one-electron transfer from PCP to Fe(III) contained in montmorillonite, resulting in formation of a PCP radical cation and subsequent reactions that result in formation of OCDD. OCDD is often the most abundant congener of the polychlorinated dibenzo-*p*-dioxins (PCDDs) found in soils, and these results explain why OCDD, through clay catalyzed formation, is the most abundant congener of PCDDs in soils and geologic formations. In this instance, Fe(III) clays catalyze the oxidation of PCP to OCDD, explaining the unique dominance of one PCDD congener in soils.

Another important area pertaining to contaminants and clay minerals is the safe storage of high-level radioactive nuclear waste. Typical storage schemes consist of storage in metal canisters in excavated solid-rock chambers, which would be backfilled with bentonite (rock form of montmorillonite) [21]. Clay backfill is used for a number of reasons, primarily due to its low hydraulic conductivity and high cation exchange capacity (CEC) and sorption capacity. The implications of Fe-bearing clays in high-level waste containment are really two-fold. The first is that Fe-content and oxidation state play a major role in clay properties and stability. Fe oxidation state affects clay properties such as CEC [22], surface area [23], surface charge and dissolution extent [24], structural arrangement [25], and swellability [5]. Alternating redox conditions are expected in high-level waste confinement storage facilities over their design lifetimes (10^4+ years). It is thus important to understand how alternating redox conditions, and potential Fe(II) flux from container erosion, may affect a backfill materials' performance.

Aside from influencing the physical alteration of clay properties, Fe in clay minerals has a second capacity in terms of high-level waste storage. A few studies have shown the ability of clay-associated Fe(II) to reduce Tc(VII), effectively immobilizing it in groundwater [26-28]. Another study found reduction of uranyl to UO_2 by Fe(II) in clay interlayers [29]. These discoveries have implications for Tc and U storage and potential

leaching into clay backfill materials under alternating redox conditions, and may help in design of high-level waste facility backfill materials with regard to predicting leaching ability of radioactive elements.

Reduced clay minerals have also been shown to reduce a number of agricultural chemicals, including chloroacetanilide herbicides (propachlor, alachlor, acetochlor, metolachlor) [30]. Here dithionite amendment of contaminanted groundwater is proposed as a remediation technique with the concept that dithionite will reduce native Fe(III) minerals and clays, which subsequently can reduce chloroacetanilides even in the absence of aqueous or surface-bound Fe(II) or excess dithionite [30]. Commercial pesticides oxamyl and alachlor were shown to have significantly reduced cytotoxicity potential after reaction with reduced nontronite [31]. In contrast, the pesticide dicamba transformed to more toxic products after the same reaction [31]. Another pesticide, 2,4-D, showed no change in toxicity after exposure to reduced nontronite [31]. In the same study, exposure of these four pesticides to oxidized clay resulted in no apparent change in toxicity, indicating that the redox state of clay minerals has important implications for the transformation and ultimate toxicity of pesticides. Structural Fe(II) in clay minerals has also been shown to provide an abiotic pathway for nitrate reduction [32].

Reduced nontronites have been touted as a potential "renewable" source of reductants in the environment due to their resistance to Fe dissolution [33]. The following work in Chapter II of this thesis may help to explain some of the observed behavior of various Fe(II) sites in clays, their reducing potential toward contaminants, and potentially even how a minimum Fe content or Fe(II)/Fe(III) ratio in clay minerals is related to contaminant reactivity.

Mössbauer Spectroscopy in Clay Science

Mössbauer spectroscopy is used throughout this study, and although its use, and specifically its application in clay science, has been extensively reviewed [34-37], it is pertinent to give a brief overview. Here the theory of the Mössbauer effect and spectroscopy will only be touched on briefly, with the focus of this section on the application and interpretation of spectra relevant to environmental samples.

Mössbauer spectroscopy utilizes the Mössbauer effect, which is a phenomenon involving resonant absorption of gamma rays. The emission and absorption of gamma rays can be recoilless in some instances, and one of the nuclear transitions with the correct conditions is the 57-isotope of Fe. This effect is only observed in solid state transitions because for recoilless absorption and emission, the energy of the gamma ray should be small compared to the mass of the receiving body because the basis of the effect is on the conservation of momentum. In gases, the receiving body is an individual atom and recoilless emission is not observed. However in solids, the mass of the entire lattice is used in the calculation because atoms are tightly bound and can transfer energy within the lattice. In the case of solid-state samples, the absorption energy imparted on the *entire lattice* is negligible. The Mössbauer effect is the basis of Mössbauer spectroscopy.

Any spectroscopy is the correlation of radiation intensity (counts) as a function of energy [34]. Mössbauer spectrometers are almost always configured in transmission mode (as it is in this study), where the spectroscopic geometry is set up so that the sample is absorbing radiation. In this setup, a ^{57}Co source decays to ^{57}Fe and gamma radiation, where the gamma radiation can be resonantly absorbed and re-emitted (instead of simply scattered as in X-ray diffraction) only by an atom with the same nuclide as the emitting source (in this case, ^{57}Co). Thus, Mössbauer spectroscopy is a technique specific to ^{57}Fe atoms in the solid state.

When the Mössbauer effect is combined with the Doppler shift, one is able to vary the velocity of emitted gamma rays relative to the nonmoving sample by oscillating the source toward and away from the sample. As the source is moving toward the sample, the relative velocity (and thus the energy via the Doppler shift formula) of the emitted gamma rays increases; as the source moves away from the sample the gamma ray velocity is decreased. This is why the energy of Mössbauer spectra is recorded in units of velocity, generally in mm/s. The resonant absorption of gamma rays is dependent on both the energy of the gamma ray and specific environment of the ^{57}Fe

nucleus, so for a given sample varying the energy of the gamma ray produces a Mössbauer spectrum.

Mössbauer spectra are unique in that they provide information on bulk properties of a material, but selectively probe the nuclear environment of the 57-isotope of Fe. Pertinent to this study, Mössbauer spectra can provide information on the oxidation state and local coordination of ^{57}Fe in clay minerals. Fitting of Mössbauer spectra involves modeling spectra with different Fe sites (e.g. *cis* or *trans* coordination, Fe(II) or Fe(III), Fe-oxide or Fe bound in clay minerals). Using statistical modeling programs, one may fit spectra to interpret subtle characteristics of Fe. The most important information Mössbauer spectra provide for Fe in clay minerals is oxidation state of Fe and differentiation between Fe-oxides and Fe in clay structures. Fe(II) is differentiated from Fe(III) by larger center shift (CS) and quadrupole splitting (QS). Fe(III)-oxides are differentiated from clay-bound Fe(III) by magnetic ordering only of the ferric oxides at low temperatures, resulting in six peaks for Fe-oxides and 1-2 peaks for clay Fe. Discussion of the specific details of how Mössbauer spectra of how clay minerals are fit are readily available elsewhere [36].

<u>Objectives and Hypothesis</u>

Objectives

The main objective of this study was to evaluate the oxidation-reduction reaction of Fe(II) after sorption onto environmental surfaces. Previous studies have shown that Fe(II) can form stable surface complexes with certain surfaces such as Al- and Ti-oxides [38, 39], but after sorption with Fe-oxides the Fe(II) transfers an electron into the bulk mineral [10, 11, 40, 41]. To further investigate the nature of sorbed Fe(II) on Fe-bearing clay minerals, the following hypothesis was developed:

Hypothesis

1. Fe(II) sorbed onto Fe(III)-containing clay minerals will transfer an electron to the structural Fe(III) in the clay.

a. Interfacial electron transfer occurs when Fe(II) is taken up by Fe(III)-containing clay, where the sorbed Fe phase is oxidized and the structural Fe(III) in the clay is reduced.

b. The extent of clay Fe(III) reduction is related to the amount of Fe(II) that is taken up by the clay.

c. Reduction of clay containing high amounts of Fe(III) induces Fe(II)-Fe(III) pairing, and subsequent electron delocalization between these pairs.

<u>Thesis Overview</u>

Chapter II addresses the above hypothesis. Chapter III provides engineering and scientific significance of the work performed in Chapter II.

Chapter II examines the sorption of Fe(II) with a natural sample of nontronite clay, NAu-2. Mössbauer spectroscopy is used in combination with enriched isotopic Fe to selectively probe the fate of the sorbed Fe(II) as well as the clay Fe(III). We unambiguously show that sorbed Fe(II) is oxidized upon sorption to NAu-2, and the Fe(III) originally contained in the NAu-2 is reduced. Reduction of clay Fe(III) induces electron delocalization, and the extent of reduction is related to the amount of Fe(II) that sorbs. Sorbed Fe(II) oxidizes to form lepidocrocite, which is confirmed with Mössbauer, pXRD, and TEM analyses. These findings have implications for Fe and electron cycling, as well as contaminant transformation in subsurface environments.

Appendix A contains a manuscript published in *Geochimica et Cosmochimia Acta* that I contributed to. Appendix B contains a manuscript in preparation for submission to *Environmental Science and Technology* that I contributed to.
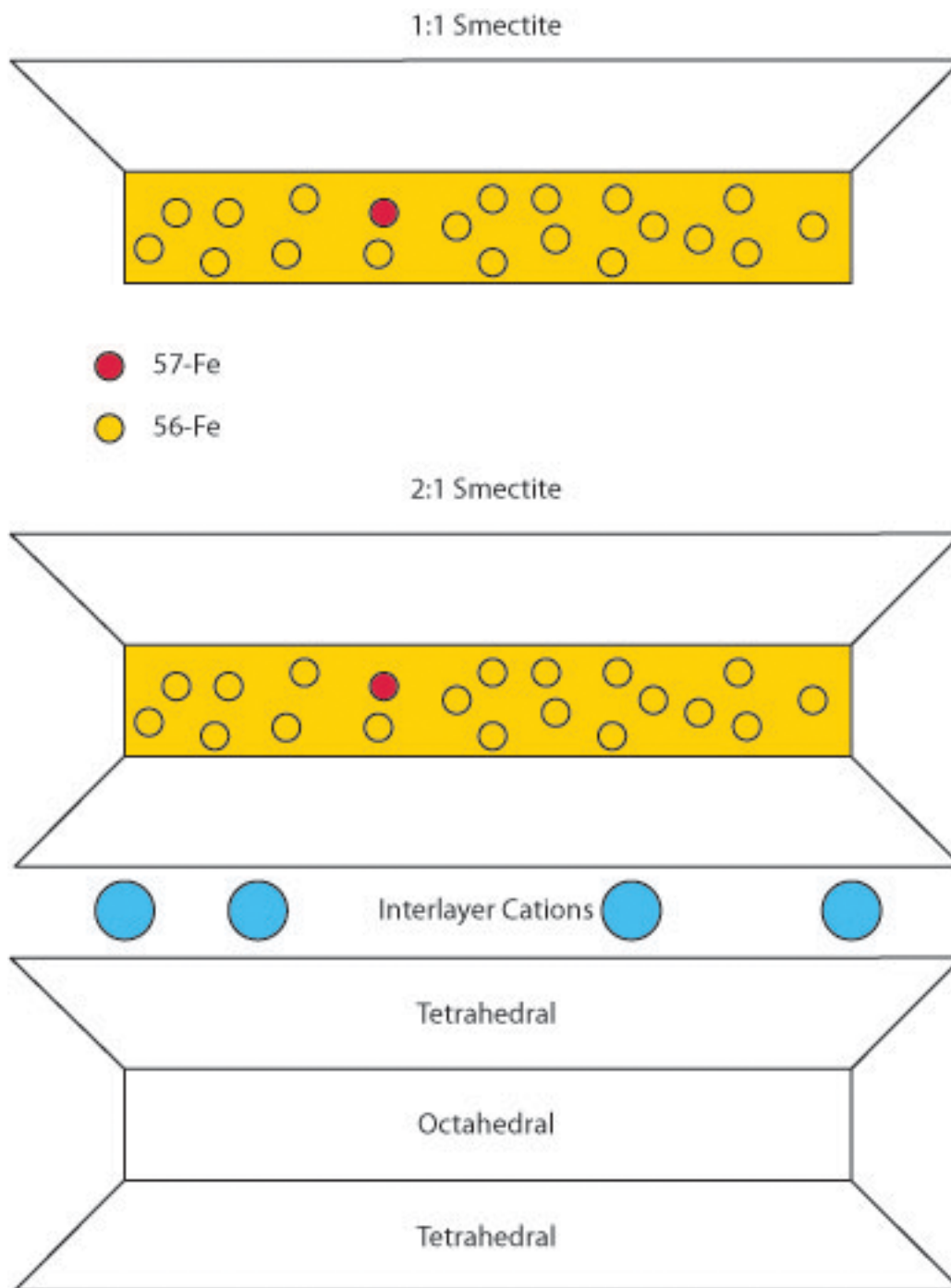
Figure 1.1. Structure of 1:1 and 2:1 phyllosilicates showing abundance of ^{57}Fe isotope (exaggerated 5% shown, 2.2% actual abundance).
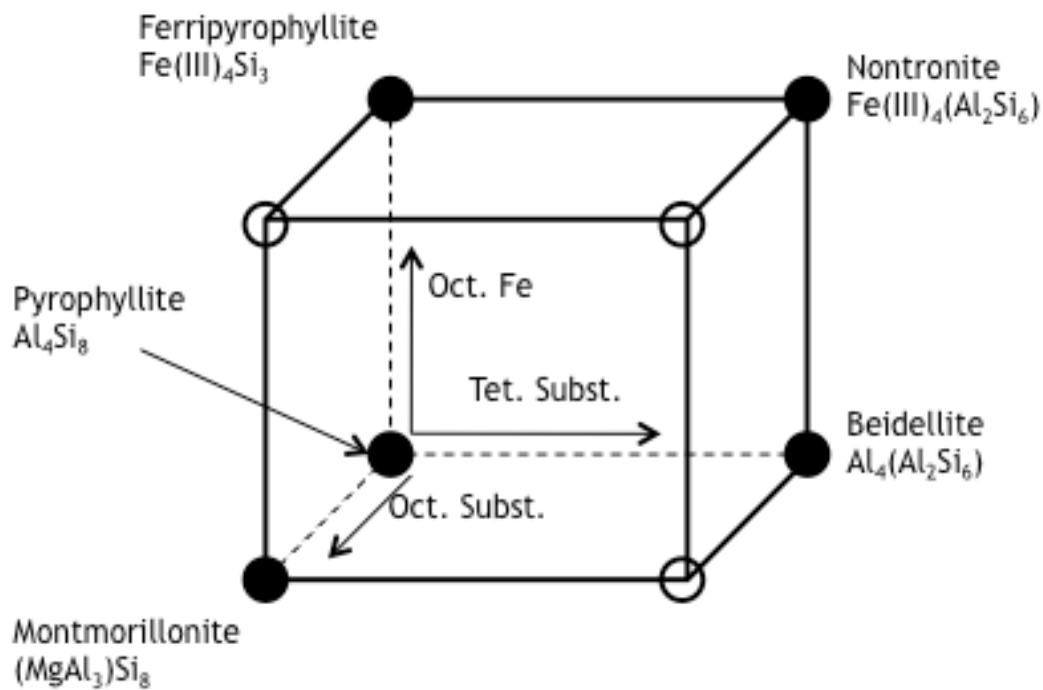
Figure 1.2. Composition of known end-members of dioctahedral (heptaphyllitic) smectites. Open circles represent theoretical but unknown end-members. Adapted from [3].

CHAPTER II: SPECTROSCPIC EVIDENCE FOR INTERFACIAL FE(II)-FE(III) ELECTRON TRANSFER IN CLAY MINERALS

Abstract

Although interfacial electron transfer has been shown to occur for sorbed Fe(II) and Fe-oxides, it is unclear if a similar reaction occurs between sorbed Fe(II) and Fe(III)-bearing clay minerals. Here, we use the isotope specificity of ^{57}Fe Mössbauer spectroscopy to demonstrate electron transfer between sorbed Fe(II) and structural Fe(III) in a nontronite clay mineral (NAu-2). Appearance of an Fe(II) doublet in the NAu-2 spectra after reaction with aqueous ^{56}Fe(II) (^{56}Fe is transparent in Mössbauer spectra) provided evidence for reduction of structural Fe(III). Mössbauer spectra using enriched ^{57}Fe(II) reveal that Fe(II) is oxidized upon sorption to NAu-2, and the oxidation product of this reaction is a ferric oxide with spectral parameters similar to lepidocrocite. The reduction of structural Fe(III) by Fe(II) induces electron delocalization in the clay structure, which we observe by variable-temperature Mössbauer spectra and macroscopic color change indicative of Fe(II)-Fe(III) pairs. Spectral measurements indicate that the rate of Fe(II)-Fe(III) electron hopping is very fast at environmentally ambient temperatures. The extent of structural Fe(III) reduction in NAu-2 is equal to the amount of Fe(II) sorbed until approximately 15% reduction, after which point reduction is no longer concomitant with the amount of sorbed Fe(II).

Introduction

Iron (Fe) is ubiquitous in the environment, where it is most commonly found in the form of oxide, oxyhydroxide, and layered silicate minerals [2, 42]. Layered silicates, referred to as clay minerals hereafter, are thought to be the most abundant Fe-bearing phase in the Earth's crust [1, 2]. In addition to the prevalence of Fe-bearing clay minerals, clays are also important due to their role of dictating groundwater redox conditions arising

---

from the ferrous/ferric (Fe(II)/Fe(III)) redox couple. Because the Fe(II)/Fe(III) redox couple is strongly dependent upon local phase (e.g., aqueous, complexed, sorbed, and structural Fe(II) can have markedly different reduction potentials) and speciation, it is important to understand how Fe-bearing clay minerals react with dissolved Fe(II) to model subsurface environments with contaminant fate in mind.

Surface complexation models have been shown to accurately describe the uptake of Fe(II) on Al- and Ti-oxide surfaces [38, 39, 43, 44]. In such reactions, it is thought that stable, sorbed Fe(II) atoms are bound at the oxide surface via inner-sphere complexation. Recent work, however, has shown that Fe(II) sorption on Fe oxide and oxyhydroxide phases is more complex [10-12, 40]. For Fe oxides and oxyhydroxides, several steps are thought to occur as a result of sorption: the sorbed Fe(II) oxidizes, transferring the electron into the underlying solid; the electron is then mobilized in the solid; and finally the electron may react with aqueous substituents or result in reductive dissolution of another Fe(III) atom [11, 45].

Previous work has emphasized that not all Fe(II) reacts similarly: Hofstetter et al. demonstrated that structural Fe(II) in clays is capable reducing nitroaromatics, while sorbed Fe(II) is not [15]. Several other contaminants have been shown to be reactive with structural Fe(II) in clays, including chlorinated alphatics [18], agricultural chemicals [30, 31, 46, 47], nitrate [32], and technetium [26-28]. Many of these studies utilized dithionite, which is capable of reducing all the structural Fe in the clay [48]. Several other reductants, however, including dissimatory Fe-reducing bacteria, hydrazine, hydroquinone, sulfide, and absorbic acid have been shown to only partially reduce the structural Fe [49, 50]. The reactivity of the partially reduced clays, which are likely more environmentally relevant, has not been investigated.

On the one hand, ion exchange and surface complexation models have been used successfully to model Fe(II) sorption on NAu-2 nontronite, a Fe-bearing clay [14]; on the other hand, a recent study has spectroscopically shown that Fe(II) is oxidized on an Fe-free montmorillonite surface in the absence of an oxidant [51], and studies have speculated that sorbed Fe(II) can participate in charge transfer with clay surfaces via

inner-sphere complexation [2, 13]. Currently, only indirect evidence exists exploring if Fe(II) taken up by Fe(III)-bearing clay minerals undergoes interfacial electron transfer.

In the present study we unambiguously examined a natural nontronite, NAu-2, before and after sorption of Fe(II). Our goal was to use the isotope specificity of ^{57}Fe Mössbauer spectroscopy to determine if electron transfer happens between Fe(II) and Fe(III) in nontronite. We examined NAu-2 before and after exposure to ^{57}Fe(II) to examine the fate of the sorbed Fe(II). To probe the fate of clay Fe(III), we reacted NAu-2 with ^{56}Fe(II), which is invisible to Mössbauer spectroscopy. The experiments clearly indicated that Fe(II) taken up by NAu-2 was oxidized to Fe(III), with the coupled reduction of structural Fe(III) in the clay structure. This clearly shows that Fe(II)-Fe(III) electron transfer occurs. Using variable-temperature Mössbauer spectroscopy, we also probed the effect of Fe(II) sorption on the local crystal environment of the clay, especially with regard to electron mobility within the clay structure.

Materials and Methods

Preparation of Clay Minerals

Samples of NAu-2 nontronite (about 25% Fe, all of which is Fe(III)) were obtained from the Source Clays Repository, IN, USA. The clay was minimally treated by grinding (pestle and mortar) and sieving (100 mesh) in the atmosphere. Although a small amount of quartz was present in this preparation, replicate sorption control experiments showed that any resulting sample heterogeneity did not affect the sorption properties of the samples significantly (1.53±0.02 mmol/g Fe(II) sorbed, n=6).

Chemical Analyses

All experiments were performed under anoxic conditions in an N_2/H_2 atmosphere with reagent grade or higher chemicals and deoxygenated, deionized water (>18 MΩ-cm). Aqueous Fe(II) was measured using the 1,10 phenanthroline method at 510 nm [52].

Fe(II) Sorption Experiments

Solutions with various concentrations of aqueous Fe(II) were prepared by addition of a small amount of concentrated stock to 15 mL of 25 mM HEPES buffer adjusted to pH 7.5. No additional background electrolyte was used to avoid cation exchange on the clay. Fe(II) suspensions were allowed to equilibrate a minimum of two hours before being filtered to remove trace precipitates. 30 mg of NAu-2 was added to Fe(II) solutions, which were mixed end-over-end. Experiments with isotopically enriched ^{56}Fe or ^{57}Fe were performed in the same way.

Mössbauer Analysis

^{56}Fe(II) and ^{57}Fe(II) stocks were prepared from isotopically enriched metal purchased from Chemgas (Boulogne, France) as previously described [10, 40]. Mössbauer measurements were performed using the same system described in our previous work [41]. Spectra were fit using the commercial software Recoil™ (Ottawa, Canada) using Voigt based fitting [53].

Results and Discussion

Reduction of NAu-2 by ^{56}Fe(II)

To investigate whether aqueous Fe(II) could reduce structural Fe(III) in a clay mineral, we exposed NAu-2 nontronite to 2 mM ^{56}Fe(II). The Mössbauer spectrum of NAu-2 before reaction with ^{56}Fe(II) is consistent with previous reports [49] and reveals that the Fe in NAu-2 was predominantly Fe(III) with no observable Fe(II) as indicated by the QS and CS. The absence of magnetic ordering at 13 K also indicates that the sample does not contain significant Fe(III)-oxides, but rather the Fe(III) exists as octahedral (6-coordinate) and tetrahedral (4-coordinate) Fe(III) within the structure of the clay mineral [49]. Previous studies have shown that NAu-2 contains 20-25% structural Fe of which >99% is Fe(III) [9, 49].

After reaction with 2 mM ^{56}Fe(II), a new doublet emerged in the spectrum at 13 K with peaks observed at approximately 2.5 and -0.1 mm/s (Figure 2.1). The hyperfine parameters of the doublet (CS = 1.24 mm/s, QS = 2.73 mm/s) are characteristic of an

Fe(II) phase. Recall that the ^{56}Fe(II) reacted with the clay is transparent in the Mössbauer spectrum, and the origin of the Fe(II) doublet must be from reduction of the structural ^{57}Fe in the clay; the presence of a Fe(II) doublet indicates that the sorbed ^{56}Fe(II) reduced the structural Fe(III) in the NAu-2. A similar Fe(II) doublet has been observed when nontronite was reduced either biotically [49] or abiotically (i.e., by dithionite) [49, 54]. This partial reduction of structural Fe(III) is further supported by a color change of the suspension from brown to green-blue, which has been observed after nontronite reduction with dithionite, and indicates the presence of Fe(II)-Fe(III) pairing [8, 13, 55].

Oxidation of sorbed ^{57}Fe(II) by NAu-2

Similar to our previous research examining electron transfer between sorbed Fe(II) and Fe(III)-oxides [10, 40, 41, 56], we also exposed NAu-2 to aqueous ^{57}Fe(II) at pH 7.5. No appreciable sorbed Fe(II) signal was observed (characterized by a doublet with CS = 1.2 mm/s, QS = 2.7 mm/s, which results in peaks at approximately -0.2 and 2.5 mm/s). Instead, we observed a doublet with hyperfine parameters consistent with an Fe(III) phase. Because the clay contains a natural abundance of approximately 2.2% ^{57}Fe atoms, it is impossible to completely exclude Fe atoms originally present in natural clay samples from Mössbauer analysis. By measuring the amount of ^{57}Fe(II) taken up by the clay we calculated that 15% of the spectral area was due to ^{57}Fe in the NAu-2, and 85% was due to the sorbed ^{57}Fe phase. In spectra collected at temperatures of 77 K and above, a ferric doublet is observed, with a very small percentage of Fe(II) as observed by a small peak at approximately 2.5 mm/s (Figure 2.2, top). The 77 K spectrum unambiguously indicates that the ^{57}Fe(II) taken up by NAu-2 is oxidized to Fe(III).

To better characterize the newly formed Fe(III) phase, Mössbauer spectra were collected at additional temperatures. For the spectrum collected at 13 K (Figure 2.2, bottom), the Fe(III) doublet magnetically orders to a sextet, indicating significant Fe-Fe interactions, a characteristic which suggests the formation of an Fe(III) oxide [36, 57]. In the 13 K spectrum, 80% of the total ^{57}Fe is attributed to the sextet, 17.5% to the singlet (clay Fe(III), spectra collected at a velocity scale between -12 and + 12 mm/s do not have the resolution to observe clay doublets, so they appear as singlets), and 2.5% to Fe(II).

Note that if the sorbed ^{57}Fe(II) transferred its electrons to the underlying clay, approximately 97.8% of the structural Fe(II) would not be observed in the spectrum because the NAu-2 only contains about 2.2% structural ^{57}Fe. The observed sextet, which accounts for 80% of the spectral area, is in good agreement with the spectral area attributed to the sorbed ^{57}Fe phase (85%). The minor Fe(II) signal in the 13 K spectrum can be attributed either to reduction of clay structural ^{57}Fe(III) similar to observations in Figure 2.1 (^{57}Fe(II) can still reduce ^{57}Fe in the clay in the same manner as ^{56}Fe(II) can!), or to a small amount of unoxidized sorbed ^{57}Fe(II) associated with the mineral surface.

An ordering temperature of 40 K – 60 K (Figure 2.3) is indicative of Fe-oxides and not of clay minerals, which typically order below 13 K, if at all [58]. Fe(II) oxidized by Fe(III) in NAu-2 nontronite produces an Fe-oxide phase with spectral parameters similar to lepidocrocite as an oxidation product (this study: CS = 0.50 mm/s, QS = 0.01 mm/s, H = 39.2 T; Murad and Schwertmann: CS = 0.34 mm/s, QS = 0.02, H = 45.6 T) [59]. The smaller hyperfine field (H) observed here is likely due to poor-crystallinity or cation substitution, both of which will influence the strength of the internal magnetic field [42]. To confirm the presence of lepidocrocite, powder X-ray diffraction (pXRD) and transmission electron microscopy (TEM) were used to characterize the NAu-2 before and after exposure to 3 mM Fe(II). The pXRD pattern for NAu-2 reacted with Fe(II) showed additional peaks not present in the untreated spectrum that were only consistent with lepidocrocite (ICDD pattern 44-1415) (Figure 4). Transmission electron microscopy (TEM) images of NAu-2 collected before and after reaction with Fe(II) reveal the emergence of small particles dispersed among the clay particles after reaction with Fe(II) (Figure 2.5). Their rod-like morphology is consistent with either lepidocrocite or goethite [42]. Collectively assessing the data, it is clear that a ferric oxide phase forms after exposure of NAu-2 to Fe(II), which is most likely lepidocrocite.

Electron Delocalization in NAu-2

In our previous works, careful inspection of the Mössbauer spectra of Fe-oxides reduced by sorbed Fe(II) has provided insight to the nature of the transferred electron [10, 40, 56]. For example, the spectra of ^{57}hematite exposed to ^{56}Fe(II) indicated that the

transferred electrons in the [57]hematite phase were likely delocalized and mobile within the oxide [56]. Here, a similar analysis of the newly formed structural Fe(II) can be performed by examining the Mössbauer spectra at a series of temperatures. The temperature at which a Mössbauer spectrum is collected can greatly alter its spectral features due to the amount of thermal energy in the sample, which affects electron mobility and spin flipping, as well as the rigidity of the sample. As a result, decreasing the temperature has several effects: it decreases electron mobility (i.e., lower valence electron hopping rates), lowers the amount of thermal energy present which allows for magnetic ordering to occur, and increases spectral quality due to a higher number of atoms which undergo recoilless emission of the incident gamma-ray [35, 57]. Variable-temperature Mössbauer studies have previously provided information regarding charge delocalization and electron hopping rates in mixed-valence minerals such as magnetite or mixed-valence clays [60]. Because layer silicates are thought to be poor conductors, changes to the local crystal environment have implications for electron availability at interfacial surfaces [25, 61], and thus contaminant transformation.

To examine crystallographic changes to NAu-2 after reaction with Fe(II), we suspended the clay in 1.5 mM [56]Fe(II) for 71 hours and collected Mössbauer spectra at a series of temperatures between 250 K and 13 K (Figure 2.6). A comparison of the spectra reveals a number of differences, most notably the disappearance of the Fe(II) doublet at T > 100 K (seen most vividly in the peak at approximately 2.5 mm/s), and splitting of the central singlet, which is thought to be tetrahedral Fe(III), to a narrow doublet (at 0.5 mm/s) [49]. Coey et al. showed similar thermally-induced Mössbauer spectral changes (i.e., disappearance of the Fe(II) signal and collapse of the central doublet to a singlet with increasing temperature) between 35 K and 470 K for a 1:1 mixed-valence iron-rich silicate, cronstedtite [62]. They argued that thermally activated electron hopping between sites required adjacent, equivalent cations of the same element, but electron hopping is not guaranteed under these conditions due to the presence of an activation energy barrier [62]. Thermally-induced electron hopping is rarely observed in silicates, but it is not clear if this is due to Mg(II), Al(III), and Ti(IV)

blocking [60], or because temperature profiling is less commonly performed in studies. At elevated temperatures (>100 K), where the Fe(II) doublet is not clearly observed in Figure 2.6, the electron hopping rate is faster than the Mössbauer characteristic time of 10^{-8} sec. At lower temperatures (< 100 K), the hopping rate is sufficiently slowed (>> 10^{-8} sec) that Fe(II) and Fe(III) atoms can be discretely separated. This data indicates that at room temperature, where most environmentally relevant experiments are conducted, the electron hopping rate of Fe(II) in NAu-2 is very fast (<< 10^{-8} sec). Additionally, this data indicates that interpretation of room temperature spectra, and even spectra collected at liquid nitrogen temperatures (77 K), may lead to incorrect quantification of the amount of Fe(II) in mixed-valence, Fe-bearing samples.

In light of these observations, we argue that previously reported data is in need of some reinterpretation. Jaisi et al. reported Mössbauer spectra of biologically reduced NAu-2 at room temperature (RT) and 12 K [49]. The 12 K spectrum had spectral properties nearly identical to the reduced spectrum in Figure 2.1 and the 13 K spectrum in Figure 2.6, except that the modeled Fe(II) area contribution in their sample was 39% as opposed to 15-18% in our spectra. However, their RT spectrum exhibits a decrease in Fe(II) area of 14% (to 25%) and collapse of the central doublet to a singlet, which they attribute to "the presence of surface adsorbed Fe(II), since surface adsorbed Fe(II) becomes visible at low temperature because of increase in the recoil-free fraction." While it is true that the recoilless fraction increases with decreasing temperature, close inspection of the two spectra also reveals that at the higher temperature the right Fe(II) peak shifts to the left (decreased QS) and becomes less symmetric, broadening on the left side. This broadening could be due to a distribution of Fe(II)-Fe(III) electron hopping rates at RT, resulting in an observed Fe valence state between +II and +III. This is further supported by an unassigned spectral area below background levels between the Fe(III) and Fe(II) signals. In their spectra of unreacted NAu-2, which includes trans-octahedral Fe(III) with the largest Fe(III) QS (extends area furthest right), no Fe(III) area extends beyond about 1.8 mm/s (Fig 2 Jaisi et al.). However, in the reduced spectra (Fig 11 Jaisi et al), the data never reach (or come close) to the background level between the Fe(II)

and Fe(III) peaks. This is despite the observed removal of trans-Fe(III), which should actually further separate the Fe(III) peak from the right Fe(II) peak (since trans-Fe(III) has the larger QS, creating the shoulder on the right side of the clay peak). These changes are consistent with our observations in Figure 2.6, and we believe that these spectra could be reinterpreted to show that biological reduction of Fe in NAu-2 (or reduction by produced biogenic Fe(II)) induces electron delocalization in the clay similar to reduction by Fe(II) under abiotic conditions in this study. However, we also believe that the observation of 39% Fe reduction is still likely valid since the fitted spectrum was collected at 12 K, where the electron hopping rate is sufficiently slowed to allow disambiguation of Fe(II) and Fe(III).

In their analysis, Jaisi et al. also report that trans-octahedral and tetrahedral Fe(III) are reduced, while cis-octahedral Fe(III) is not [49]. This claim is based on changes between the unreacted and bioreduced Mössbauer spectra. The first change is the removal of trans-octahedral Fe(III), which we also observe in Figures 2.1 and 2.6, where the right shoulder of the central peak disappears after reduction. The other is splitting of the central singlet to a doublet with spectral parameters of CS = .41 QS = .44 (this study) and CS = 0.48 mm/s and QS = 0.41 mm/s in Jaisi *et al.* [49].They argue that this is consistent with removal of tetrahedral Fe(III), which exhibits lower values of CS and QS than those of the observed doublet (here they cite Goodman, 1978, Clay Minerals; 13, 351-356). Interestingly, earlier in this paper the authors acknowledge differences in the CS of unreacted NAu-2 (which appears to be a change of about 0.2 mm/s and also observed in our data) which "were due to second-order Doppler shifts" between RT and 12 K. We agree that tetrahedral Fe(III) is likely reduced in their sample, but the observed collapse of the central doublet (12 K) to a singlet at RT for the same bioreduced sample is not intuitively consistent with removal of tetrahedral Fe(III) since the suggested reasoning (splitting of the singlet to a doublet) is only observed at 12 K and not at RT. However, we believe this collapse is due to two synergistic (and unfortunate) reasons: (1) to a decrease in QS of the Fe(II) signal clearly observed in the peak at ~2.5 mm/s, but less clearly observed in the left peak and (2) a decrease in CS of the clay at lower

temperature due to second-order Doppler shift effects. As QS decreases, the left peak of the Fe(II) signal will shift right into the clay Fe(III) area, and at higher temperature (i.e. RT) could move to occupy an area similar to that previously occupied by tetrahedral Fe(III), with additional broadening on the inner (this time right) side. At the same time, the clay Fe(III) area is moving to the left at colder temperatures due to second-order Doppler shift effects. This means that at higher temperatures the left Fe(II) peak is moving to the right due to faster ET rates (blurring of Fe(II) and Fe(III) signal) and the clay cis-octahedral Fe(III) doublet is moving to the left due to CS decrease induced by second-order Doppler shifts; the peaks are moving together and when they converge appear as a singlet due to overlap. Here this decrease in QS for the Fe(II) signal can more clearly be seen in Jaisi et al.'s data because of the greater reduction extent and thus larger proportion of Fe(II)/Fe(III) relative area.

Extent of NAu-2 Reduction by Fe(II)

To probe the extent of Fe(III) reduction by ^{56}Fe(II), we performed a series of experiments where 0-3 mM ^{56}Fe(II) was sorbed onto NAu-2. The extent of clay Fe(III) reduction measured by Mössbauer relative areas increased concomitantly with the addition of ^{56}Fe(II) until about 15% reduction of the structural Fe(III) (Figure 2.7, Figure 2.8 contains the Mössbauer spectra). After this point, as more ^{56}Fe(II) was added, the observed structural Fe(III) reduction was less than the amount of ^{56}Fe(II) sorbed. We did observe some kinetic effects at higher Fe(II) loadings: when 2.5 mM 56Fe(II) was added to the NAu-2 suspension, Fe(II) sorption increased from 1.75 mM to 2.02 mM after 25 and 134 hours, respectively; this caused a 2.9±0.5% increase in theoretical Fe(III) reduction, and an observed 3.8% increase in Fe(III) reduction in the Mössbauer spectrum. Another sample was allowed to equilibrate for 62 days under the same conditions, and no difference was observed in Fe(II) uptake or Fe(III) reduction extent compared to the 134 hour sample (Figures 2.9 and 2.10). Interestingly, in a study examining NAu-2 reduction by *Shewanella putrefaciens* CN32, 14-18% Fe(III) reduction was observed in the absence of AQDS, in good agreement with the 15% observed here [49].

One possible explanation for the extent of Fe(III) reduction reaching a plateau near 15% is that some Fe(III) sites are more labile to reduction than others. In a study that examined biological reduction of NAu-2, the researchers observed qualitatively that tetrahedral and trans-octahedral Fe(III) was preferentially reduced using Mössbauer spectroscopy [49]; a similar preferential abiotic reduction was observed using optical absorbance spectroscopy [8]. Yet in another study the opposite conclusion was drawn: tetrahedral Fe(III) was found to be unreactive, and octahedral Fe(III) was preferentially reduced [63]. When examining the spectral changes in Figure 2.1 before and after the addition of ^{56}Fe(II), the untreated spectrum contains a single peak at 0.5 mm/s, while the reduced spectrum contains two doublet peaks at 0.3 and 0.7 mm/s. Tetrahedral Fe(III) exhibits a singlet peak with a CS of approximately 0.5 mm/s [49], and thus the spectral changes are consistent with the preferential reduction of tetrahedral Fe(III). As argued earlier, however, attempting to differentiate between octahedral and tetrahedral Fe(III) in the Mössbauer spectrum results in non-unique solutions, and is thus limited to qualitative assessment. The additional reduction observed when the experiment was extended from 1 to 5.5 to 62 days suggests that the 15% observed reduction is not a thermodynamical endpoint, but is instead an indication that kinetic rates are impacting the observations. In summary, the results observed here are in agreement with the hypothesis that tetrahedral Fe(III) is preferentially reduced over octahedral Fe(III), but this cannot be concluded from this data set alone.

Environmental Implications

The observation that Fe(II) sorbed to a nontronite surface undergoes interfacial electron transfer resulting in the formation of a mobile, reactive electron in the clay structure has several implications. Aqueous Fe(II) appears to be a capable reductant of structural-Fe in the clay surface, and may subsequently be a better model reductant than dithionite for environmentally relevant conditions (although dithionite is used in remediation techniques). Dithionite is traditionally used because it is capable of fully reducing all the structural Fe, but since reduction by dissimilatory iron-reducing bacteria, aqueous Fe(II), and other chemical reductants (e.g., hydrazine, sulfide) only partially reduce the

structural Fe(III) [49, 50, 64], experiments using excess dithionite may overestimate the reactivity of Fe-bearing clay minerals with contaminants under natural conditions.

This work also draws into the question the applicability of surface complexation models in explaining Fe(II) uptake on Fe-bearing clays. Despite the accuracy with which these models have been used in the past to explain Fe(II) uptake [14], they appear to be physically inaccurate descriptors of the reactions. For magnetite, we have argued for a semiconductor-based modeling approach to explain the extent of Fe(II) uptake [40], which is likely also applicable to Fe(II)-clay electron transfer reactions, based on the results presented here.

Table 2.1. Fe(II) sorption data and Mössbauer parameters for fitted spectra in this study.

Sample Name	pH	FeII Init (mM)	FeII Sorb (mM)	Eq. Time (hrs)	Temp (K)	Chi2	CS	QS	stdev (QS)	Fe(III) doublet?	Rel. Area (%)	A+/A- floated?	Comments
NAu-2	---	---	---	---	13					No		No	Dry Powder
	---	---	---	---	298					No		No	Dry Powder
	7.5	0	0	115	13								
	7.5	0	0	115	298								
3 mM 56	7.5	2.729189189	2.382756757	15	13	0.56952	1.244	2.73473	0.014991	Yes	16.586	No	
	7.5	2.7	2.160324324	42.5	13	0.548271	1.23256	2.75932	0.0321379		17.3837	No	
2.5 mM 56	7.5	2.324189189	1.753594595	25	13	1.725	1.23776	2.74562	0.0060337	Yes	15.2272	No	
	7.5	2.324189189	2.023432432	134	13	1.47	1.2127	2.80978	0.0065	Yes	18.9987	No	
	7.5	2.335135135	2.051243243	1488	13	1.29609	1.21764	2.81959	0.0112107	Yes	19.3793	No	
2 mM 56	7.5	1.893648649	1.783886486	20	13	0.710243	1.24151	2.73343	0.0177718	Yes	16.0999	No	
	7.5												
1.5 mM 56	7.5	1.441216216	1.421540541	71	13	0.507255	1.24095	2.72614	0.0659932	Yes	15.4073	No	
	7.5	1.441216216	1.421540541	71	77	0.632859	1.26304	2.43486	0.309672	Yes	12.3318	No	2 Fe(III) site
	7.5	1.441216216	1.421540541	71	100	1.07769	1.12823	2.43333	0.0413442	Yes	11.654	No	
	7.5	1.441216216	1.421540541	71	120							No	
	7.5	1.441216216	1.421540541	71	250							No	
	7.5												
1 mM 56	7.5	0.908513514	0.904016216	29	13	0.754992	1.24931	2.67126	0.0360153	Yes	8.98922	No	
	7.5												
0.5 mM 56	7.5	0.467027027	0.465481081	28	13	1.76644	1.24764	2.63614	0.0291494	Yes	4.43938	No	
	7.5												
1 mM 57	7.5	1.043513514	1.038875676	75	13								
	7.5	1.043513514	1.038875676	75	21								
	7.5	1.043513514	1.038875676	75	40								
	7.5	1.043513514	1.038875676	75	77								
	7.5	1.043513514	1.038875676	75	140								
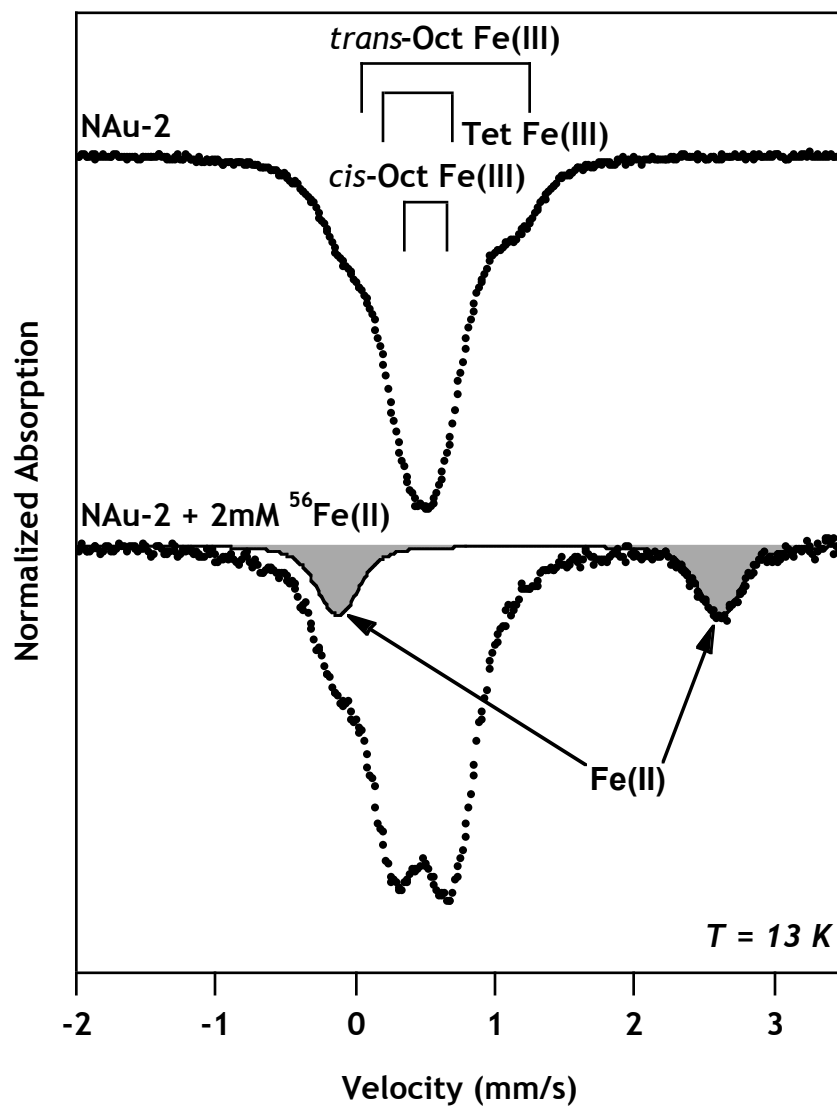
Figure 2.1. Mössbauer spectra of NAu-2 before (top) and after (bottom) reaction with
^{56}Fe(II). The grayed area in the bottom spectrum was the result of a least-
squares Voigt-based fit. Experimental conditions: 2 g/L NAu-2 reacted with
2mM ^{56}Fe(II) in pH 7.5 HEPES buffer under anoxic conditions.
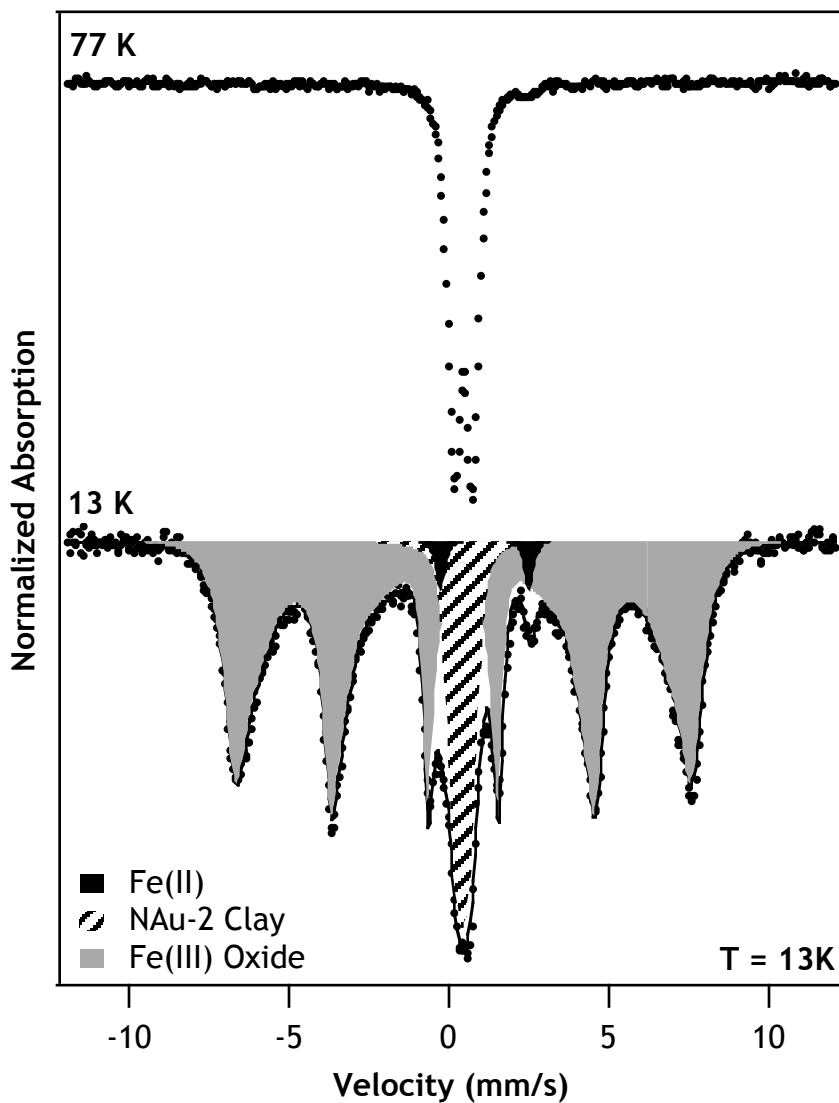
Figure 2.2. Mössbauer spectra of NAu-2 after reaction with ^{57}Fe(II) at 77 K (top) and 13 K (bottom). Experimental conditions: 2 g/L untreated NAu-2 reacted with 1 mM ^{57}Fe(II) in pH 7.5 HEPES buffer under anoxic conditions. A Voigt fit was used , the sextet represents 80% of the spectral area, clay Fe(III) 17.5%, Fe(II) 2.5%. Note that ^{57}Fe(II)$_{uptake}$ / Total ^{57}Fe(III) = 85% (^{57}Fe(II)$_{uptake}$ / ^{57}Fe(III)$_{clay}$ = 5.7), so that only 15% of the spectral area is due to Fe atoms originating from the clay.
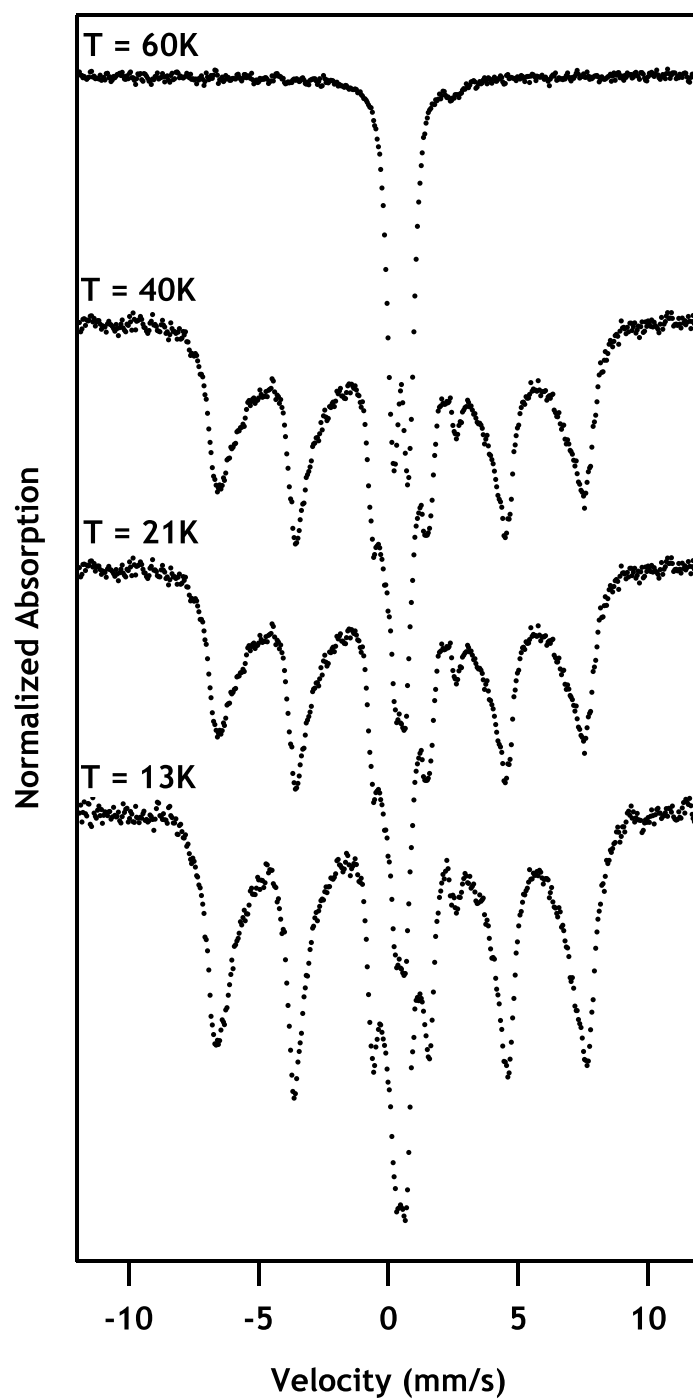
Figure 2.3. Mössbauer spectra of 1 mM 57Fe(II) reacted with NAu-2. The marked change in spectral features between 60 K and 40 K is due to magnetic ordering of the Fe(III) oxide from a ferric doublet to a sextet.
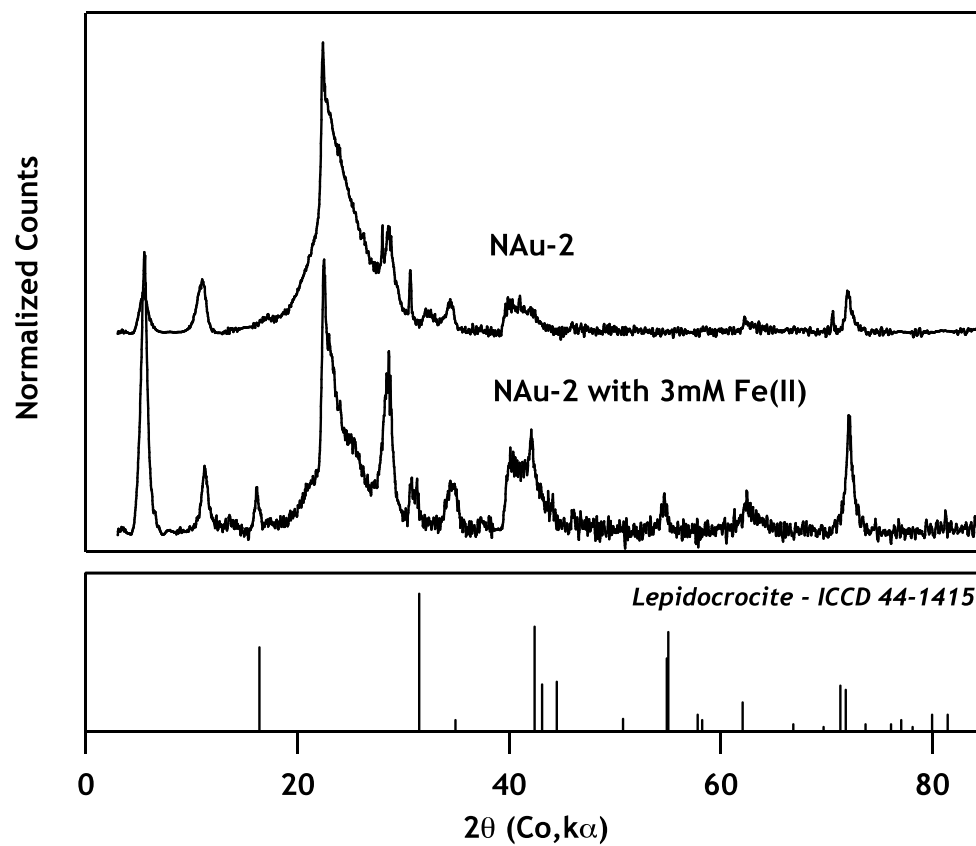
Figure 2.4. XRD patterns of NAu-2 and NAu-2 equilibrated with 3 mM Fe(II) at pH 7.5 under anoxic conditions. Both samples were mixed with glycerol before transfer to the pXRD to prevent air oxidation. ICCD pattern for lepidocrocite is provided for reference.
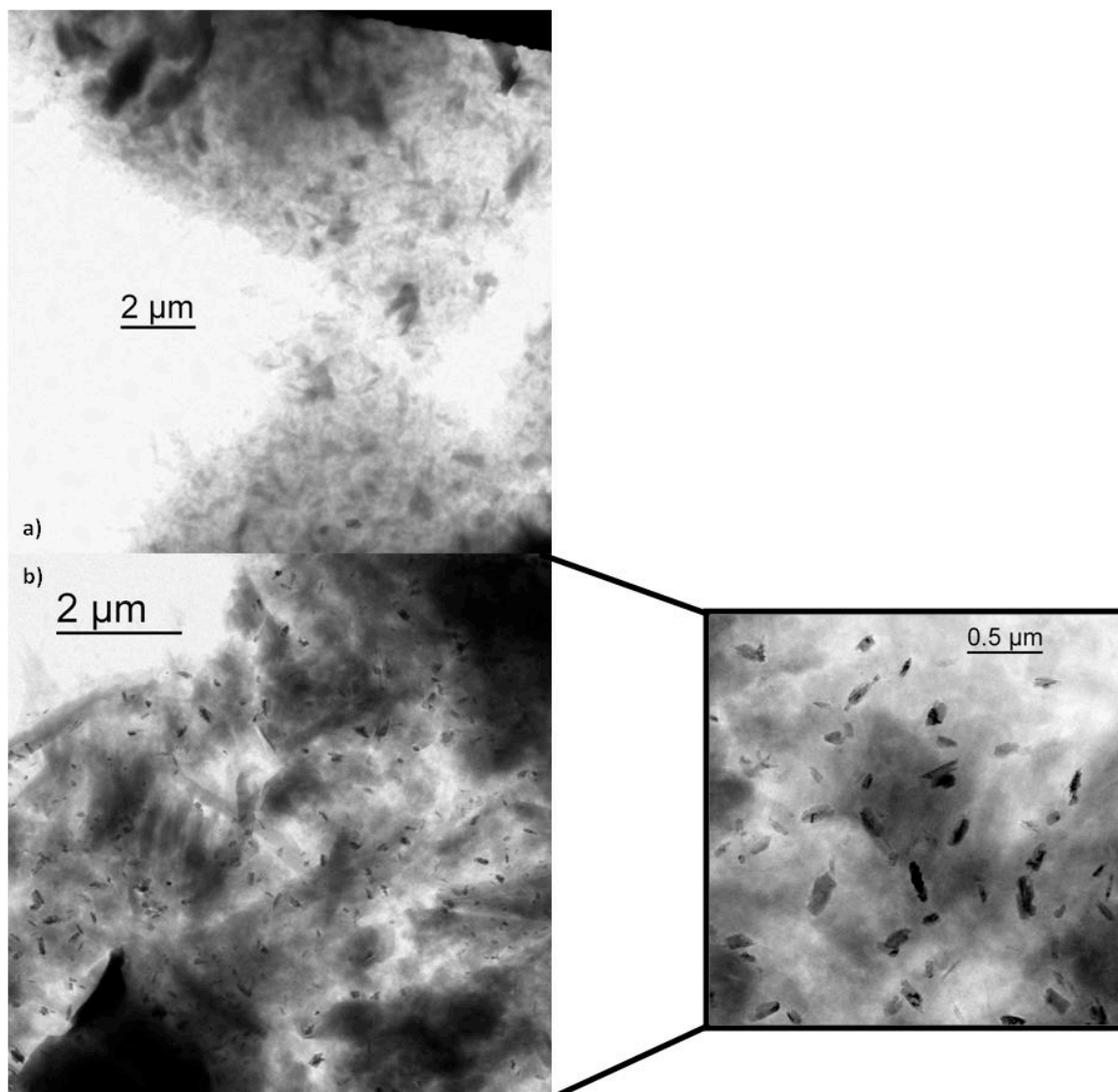
Figure 2.5. TEM micrographs of NAu-2 suspended in pH 7.5 buffer (a), and reacted with 3 mM Fe(II) at pH 7.5 (b).
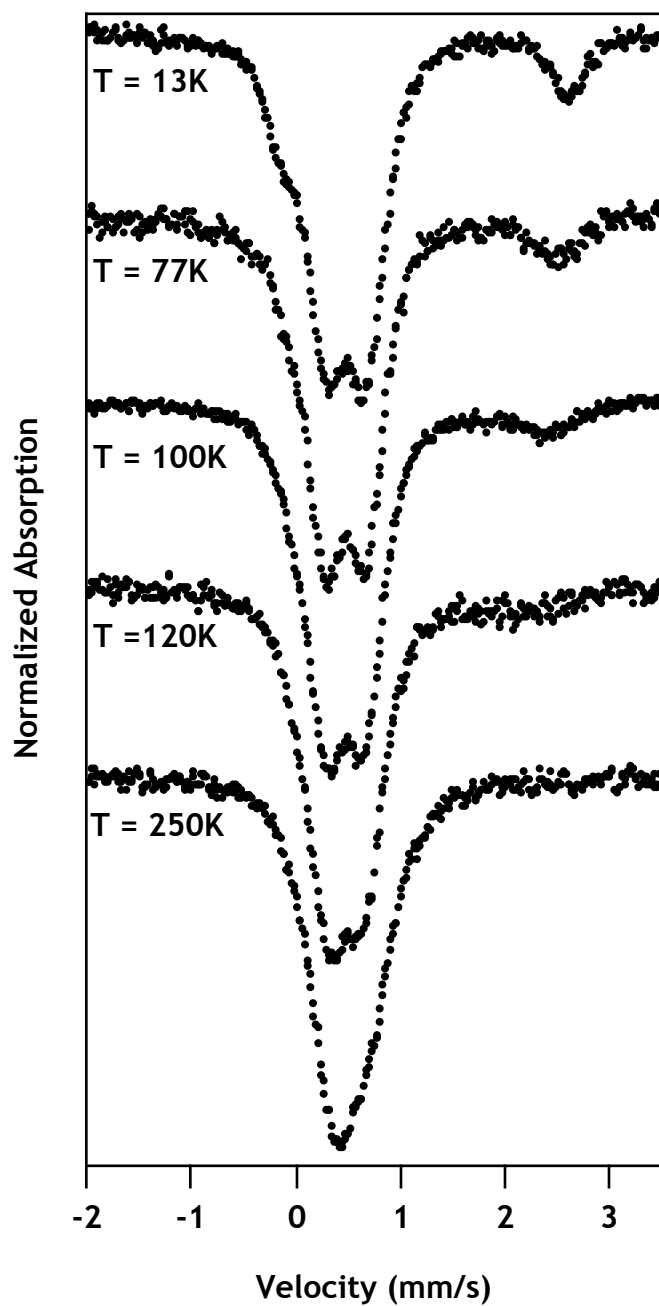
Figure 2.6. Mössbauer spectra of 1.5 mM ^{56}Fe(II) reacted with NAu-2. Spectra were collected between 250K and 13K from the same sample.
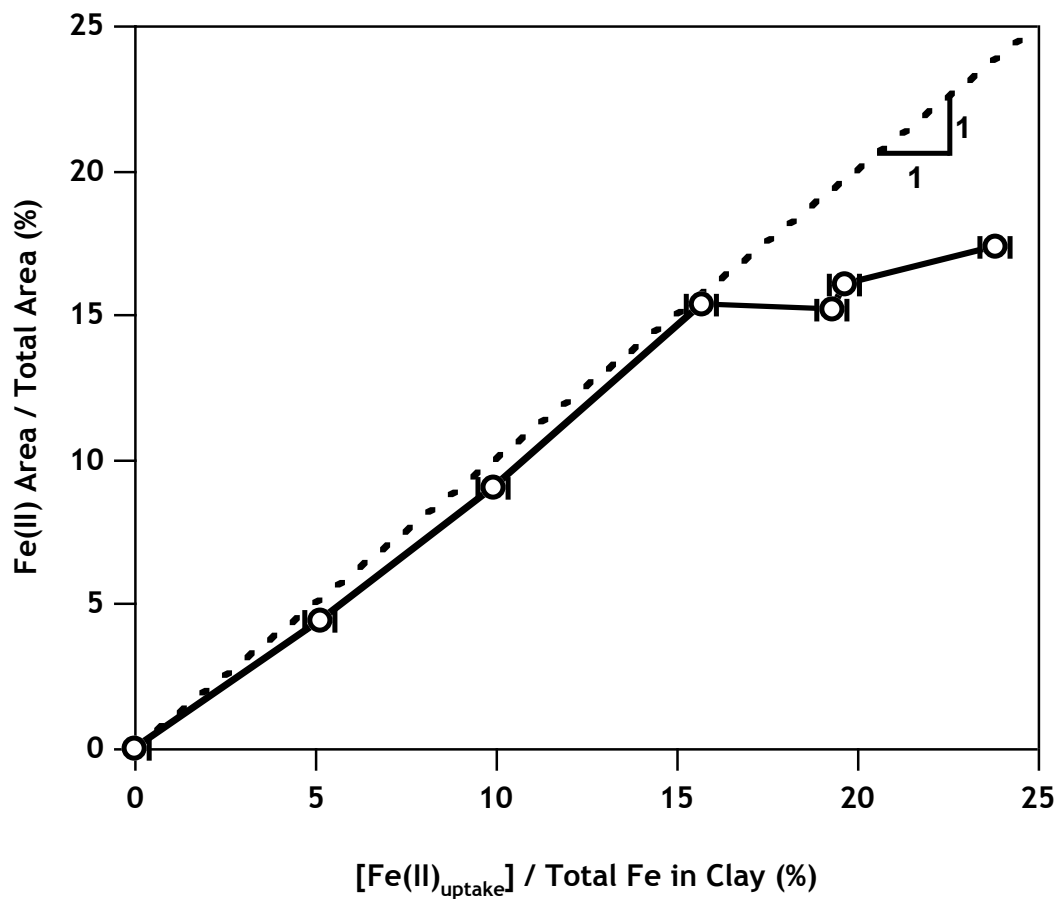
Figure 2.7. Comparison of relative amount of Fe reduced in clay to amount of Fe(II) sorbed. Amount of Fe reduced was calculated from the relative area of the Fe(II) doublet to the total area in Mössbauer spectra shown in Figure S4. The amount of Fe(II) sorbed was determined from the difference between initial aqueous Fe and final aqueous Fe.
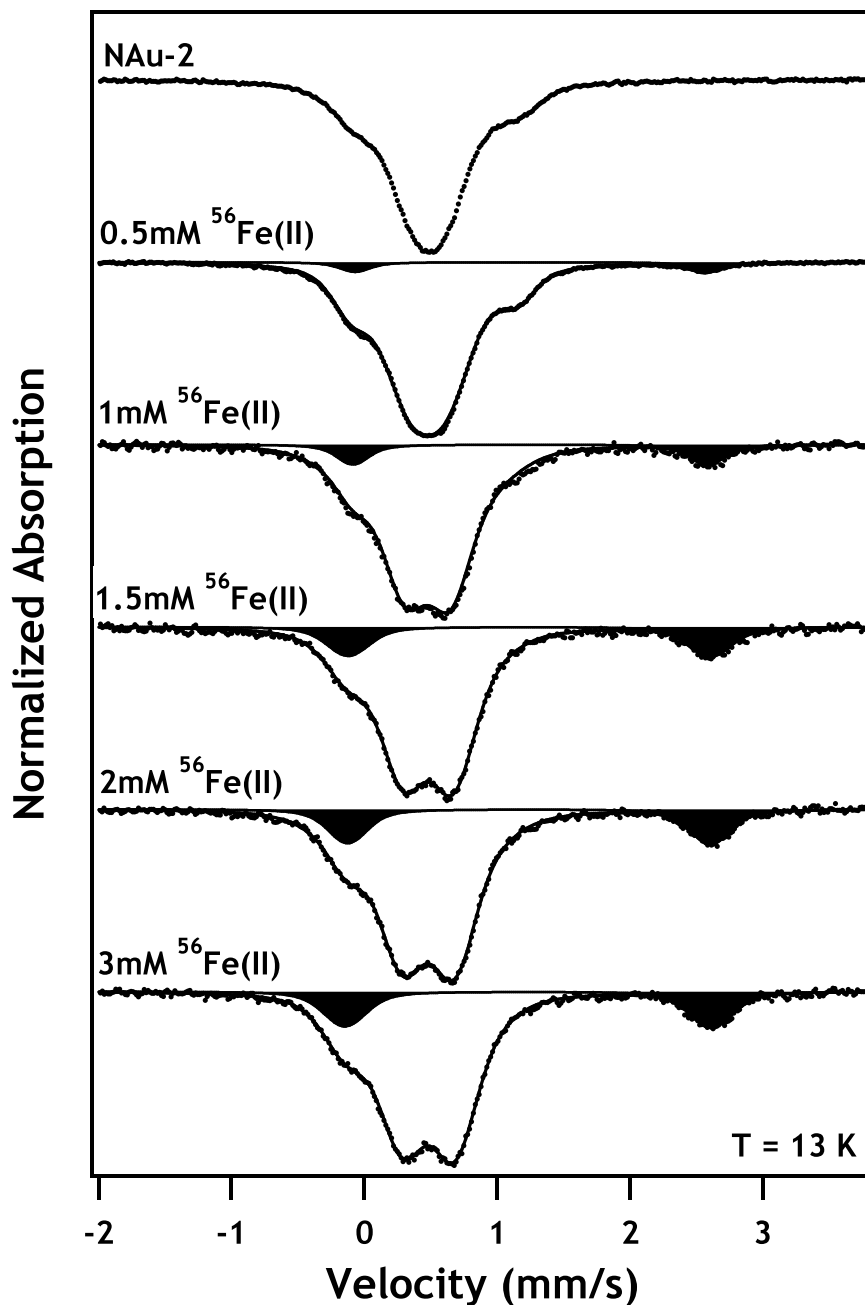
Figure 2.8. Mössbauer spectra of NAu-2 reacted with 0.5-3 mM ^{56}Fe(II) (spectra for data in Figure 3). Spectra were collected at 13K. Equilibration times ranged from 20-71 hours. Fe(II) uptake determined by aqueous Fe(II) measurements was >90% except for Fe(II)$_0$ = 3mM, which had 80% uptake. Fe(II) spectral area contribution as determined by Voigt-based fits is highlighted. The solid line is the overall fit overlaid on measured data points.
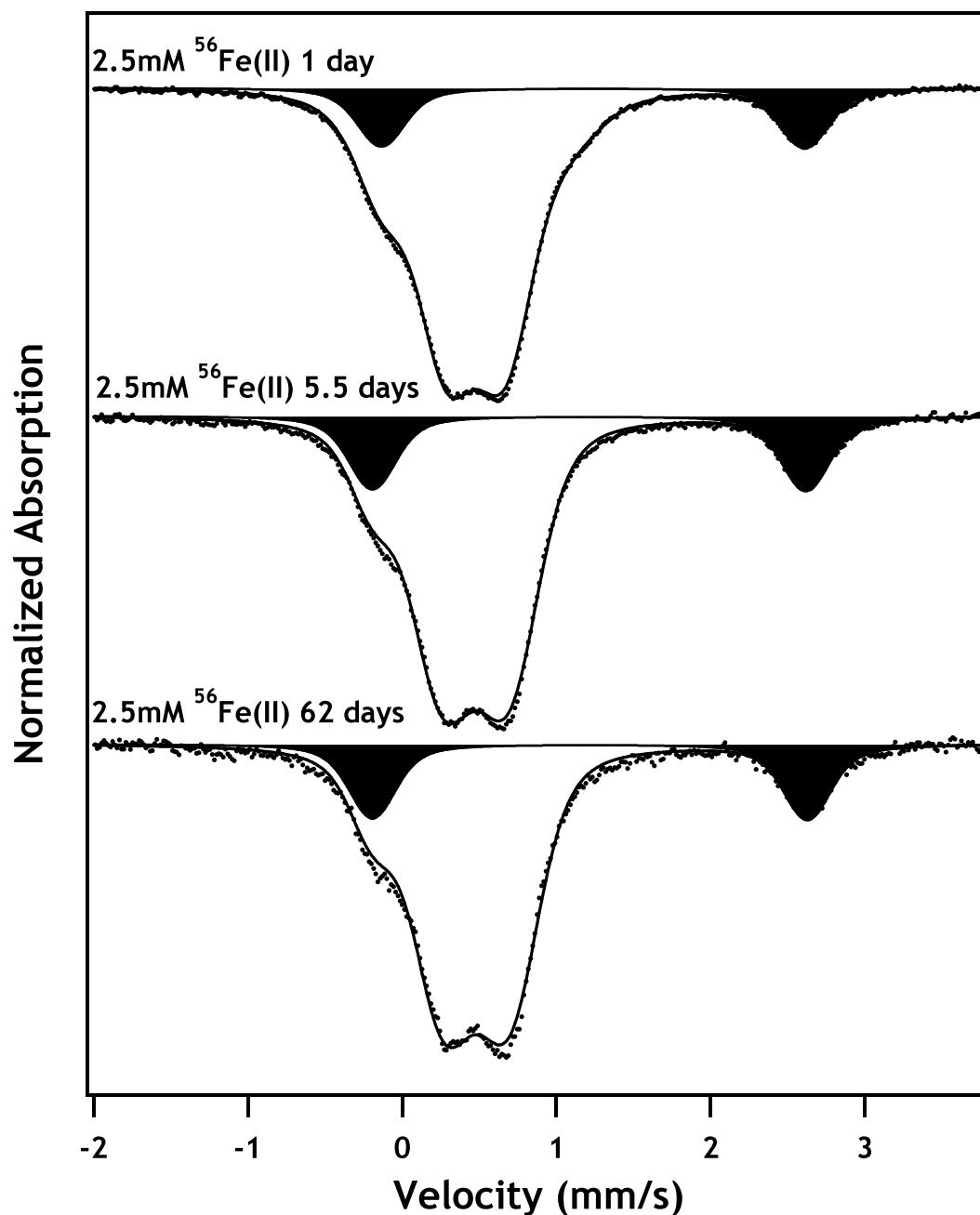
Figure 2.9. 13 K Mössbauer spectra of 2.5 mM ^{56}Fe(II) equilibrated with NAu-2 for 1, 5.5, and 62 days. The Fe(II) spectral contribution determined by Voigt-based fitting is highlighted, and the solid line is the overall fit overlaid on measured data points.
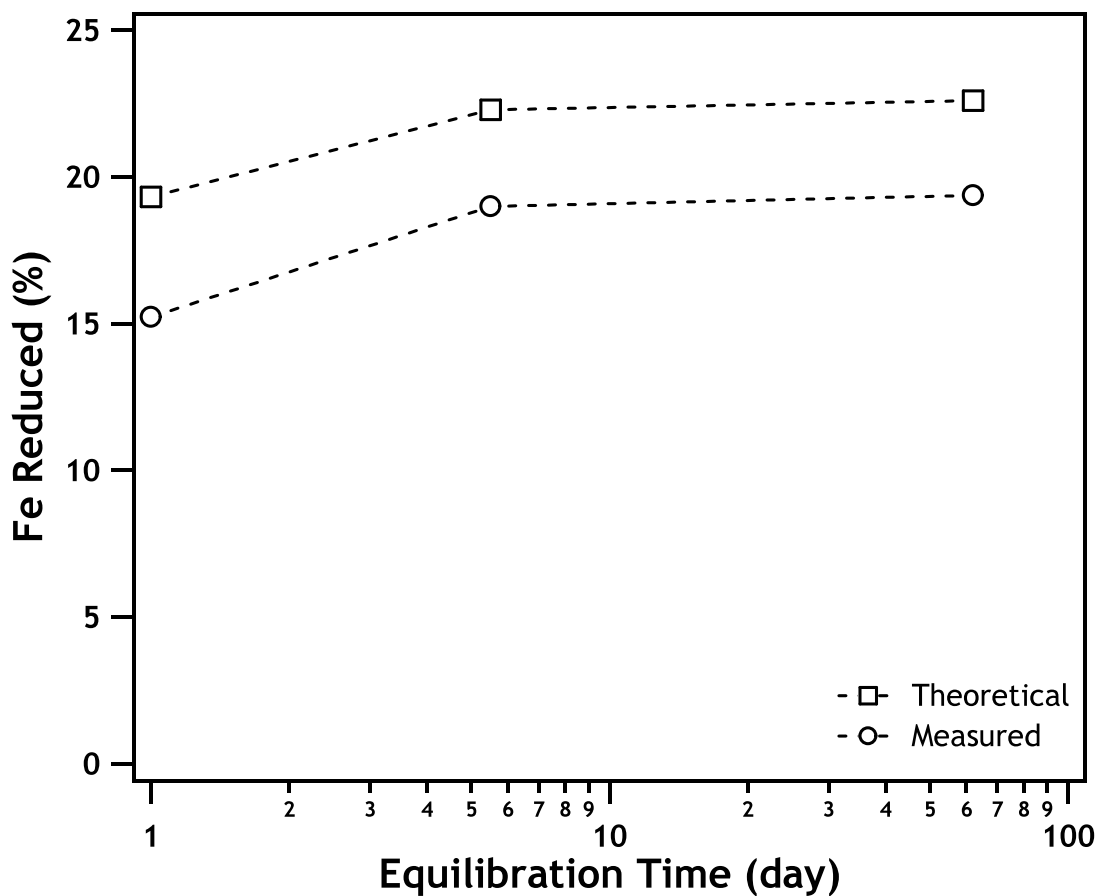
Figure 2.10. Fe(III) reduction (%) measured by Mössbauer relative area (circles) as a function of equilibration time (log scale) of NAu-2 and 2.5 mM ^{56}Fe(II) at pH 7.5. Theoretical reduction extents (squares, assuming all Fe(II) taken up from solution reduces clay Fe(III)) are provided, showing that the increased reduction extent tracks with increased amount of Fe(II) taken up from solution.

CHAPTER III: ENGINEERING AND SCIENTIFIC SIGNIFICANCE

Summary

This work has applied Mössbauer spectroscopy to the study of the interfacial reaction between Fe(II) and Fe(III) that occurs after sorption of Fe(II) onto an Fe-rich clay, NAu-2. The results in this thesis show that Fe(II) that sorbs onto NAu-2 reduces Fe(III) present in the clay structure, and the Fe(II) is oxidized to lepidocrocite, a ferric oxide. By collecting Mössbauer spectra at various temperatures, we were able to also observe the nature of the reduced clay regarding electron mobility within the crystal structure. Data shows that in reduced samples, Fe(II)-Fe(III) electron hopping occurs. This conclusion is significant because electron availability, especially at particle surfaces, has implications for contaminant transformation. Further, we showed that room temperature and even liquid nitrogen Mössbauer spectra, two temperatures most commonly used for collection of Mössbauer spectra of natural samples, may provide misleading results when trying to quantify the Fe(II)/Fe(III) ratio. This is because the electron hopping rate at higher temperatures may be greater than the Mössbauer characteristic time of about 10^{-8} seconds.

Outlook and Recommendations for Future Work

The work presented here provides a new interpretation of how Fe(II) reacts with Fe-rich clay minerals. Previous studies consistently modeled Fe(II) as simply a sorbed species on clay surfaces and did not account for electron transfer to structural Fe(III). To extend this work's significance, additional experiments should replicate the experiments performed here on clays that contain various amounts of structural Fe. In this work, we used an Fe-rich nontronite and observed reduction and electron delocalization in the clay. Previous studies would suggest that with less Fe in the clay, electron delocalization would not occur because the Fe(II)-Fe(III) pairs would be disconnected or "insulated" by Al or Si; it is generally thought that continuously juxtaposed Fe atoms are required to "connect the circuit" of electron hopping. This raises the question as to whether the ability for the electron to delocalize is also a prerequisite for structural Fe(III) reduction

in clays, which is testable with the proper clay minerals and the sensitivity of Mössbauer spectroscopy.

To extend this work, it would be worthwhile to explore the Fe(II)-clay-contaminant system more in-depth. Nontronites reduced by dithionite have been shown to reduce a number of contaminants as noted in the thesis. Is Fe(II)-reduced nontronite equivalent to dithionite-reduced nontronite in terms of its ability to reduce contaminants such as NACs, radionuclides (U, Tc), or agricultural chemicals? Upon reduction with Fe(II), are clays that originally contain less structural Fe(III) still reactive toward contaminants even if electron delocalization is blocked?

Nontronite can also be reduced by dissimilatory iron reducing bacteria (DIRB). In studies of NAu-2 reduced by *S. putrefaciens* CN32 some reductive dissolution was also observed [49]. In light of the findings in this study, it would be interesting to be able to determine the contribution of biogenic Fe(II) to the overall "biological" reduction process, *i.e.* how much Fe(III) is reduced directly by bacteria, and does biogenic Fe(II) (the product of biological reduction) act as a secondary reductant? Are Fe(II) and organisms able to reduce the same crystallographic sites in clay, or do they preferentially reduce different Fe(III) sites? In a previous study of biological reduction of NAu-2, TEM images after reduction did not reveal the formation of any ferric oxides in contrast to this study [49]. Perhaps a cycle begins with biological reduction, but is then extended to abiotic reduction coupled with growth of ferric oxides, which are easily respired on by DIRB.

Another area to explore is the role of the reductant. What other environmental reductants are able to reduce clay? Do they also induce electron delocalization, or is this phenomenon specific to reduction by sorbed Fe(II)? Of particular interest is arsenic redox chemistry due to arsenic's toxicity and the mass human exposure in Southeast Asia, among other areas. As(III) is more toxic and more mobile than As(V), and Fe redox state plays a major role in determining the speciation, and thus toxicity and mobility, of As in natural systems. Can As(III) also reduce oxidized Fe-rich clays? If so, what is the

As(V) oxidation product? Similar experiments may be performed with other redox active metals such as, *e.g.* chromium.

There is also additional work to be done in modeling the fate of sorbed Fe(II), especially if certain Fe(III) sites within clays are preferentially reduced. It is possible to speculate from the data presented here that *trans*-octahedral Fe(III) is reduced and *cis*-octahedral Fe(III) is not (or to a lesser extent), but unambiguous model fits were not attainable up to this point in this study. More detailed analysis, perhaps combining complementary techniques, may allow further interpretation of the spectra, especially if tetrahedral Fe(III) were quantified in the samples.

APPENDIX A: INTERPRETING NANOSCALE SIZE-EFFECTS IN AGGREGATED
FE-OXIDE SUSPENSIONS: REACTION OF FE(II) WITH GOETHITE

Abstract

The Fe(II)/Fe(III) redox couple plays an important role in both the subsurface fate and transport of groundwater pollutants and the global cycling of carbon and nitrogen in iron-limited marine environments. Iron oxide particles involved in these redox processes exhibit broad size distributions, and the recent demonstrations of dramatic nanoscale size-effects with various metal oxides has compelled us, as well as many others, to consider whether the rate and extent of Fe(II)/Fe(III) cycling depends upon oxide particle size in natural systems. Here, we investigated the reaction of Fe(II) with three different goethite particle sizes in pH 7.5 suspensions. Acicular goethite rods with primary particle dimensions ranging from 7 by 80 nm to 25 by 670 nm were studied. Similar behavior with respect to Fe(II) sorption, electron transfer and nitrobenzene reduction was observed on a mass-normalized basis despite almost a three-fold difference in their specific surface areas. Scanning electron microscopy (SEM) images, dynamic light scattering and sedimentation measurements all indicated that, at pH 7.5, significant aggregation occurred with all three sizes of goethite particles. SEM images further revealed that nanoscale particles formed dense aggregates on the order of several microns in diameter. The clear formation of particle aggregates in solution raises questions regarding the use of primary particle surface area as a basis for assessing nanoscale size-effects in iron oxide suspensions at circum-neutral pH values. In our case, normalizing the Fe(II) sorption densities and rate constants for nitrobenzene reduction by BET surface area implies that goethite nanoparticles are less reactive than larger

particles. We suspect, however, that aggregation is responsible for this observed size-dependence, and argue that BET values should not be used to assess differences in surface site density or instrinsic surface reactivity in aggregated particle suspensions. In order to realistically assess nanoscale size-effects in environmental systems that are likely to aggregate, new methods are needed to quantify the amount of surface area accessible for sorption and reaction in wet nanoparticle suspensions, rather than assuming that this value is equivalent to the surface area determined from the characterization of dry nanoparticles.

Introduction

Ferrous and ferric iron are one of the most familiar environmental redox couples, playing critical roles in air, water and soil systems. In subsurface environments, the Fe(II)-Fe(III) redox cycle is driven by microbial processes, in which bacteria gain energy by using naturally occurring ferric iron solids as terminal electron acceptors [65, 66]. In addition to contributing to subsurface elemental cycling, such Fe(II)-Fe(III) redox reactions are intricately linked to contaminant fate via the formation of sorbed Fe(II) species on Fe(III) mineral surfaces and biogenic, ferrous iron-containing phases, both of which have been shown to reduce a broad spectrum of common groundwater pollutants [67-74].

In natural environments, iron oxides and (oxyhydr)oxides (hereafter collectively referred to as iron oxides) are ubiquitous and often display a broad distribution of particle sizes. Their occurrence in the nanometer size regime has been previously demonstrated, with examples ranging from ultra-fine aerosols [75] to precipitates in soils and sediments [76-78]. Recent field-scale evidence has even suggested a predominance of nanoscale goethite in some natural aquatic systems, where its occurrence was attributed to iron redox cycling at the boundary between anoxic and oxic zones in sediments [79]. Although the persistence of iron oxides as nanoparticles could result from coprecipitation or surface complexation that inhibits further growth into larger crystallites [79], it is also possible that the surface energies of some oxides are low enough to allow nanoparticles to represent metastable phases [80]. Because of

their large specific surface area, iron oxide nanoparticles could represent, therefore, a key reactive constituent in many environmental systems even though they may only comprise a small fraction of total iron in the system on the basis of mass or volume [81].

Because of their prominence in natural environments, as well as their widespread application in industry and catalysis [82], the size-dependent properties and reactivity of iron oxides have long been the focus of laboratory investigations [e.g., 83]. Nanoparticles are generally assumed to be more reactive than larger particles, and indeed, many unique size-dependent properties of nanoparticles have been reported [84, 85]. Although their reactivity is sometimes attributed to very high specific surface areas, recent experimental evidence indicates that iron oxide nanoparticles may display reactive properties that cannot be extrapolated to the behavior of larger materials simply on the basis of surface area differences. These investigations have focused on common iron oxides such as goethite, ferrihydrite and hematite, and have reported enhanced nanoparticle reactivity with respect to interfacial processes such as cation adsorption, electron transfer and oxide dissolution [86-88]. Such behavior could result from a greater density of reactive sites per unit surface area on nanoparticle surfaces, or greater inherent reactivity of nanoparticle surface sites relative to sites on larger particles [89]. In the latter case, factors potentially responsible for the unique reactivity of iron oxide nanoparticles were recently detailed in a review by Waychunas et al. [81], and these include surface restructuring, surface curvature, and quantum confinement effects, all of which could emerge as a function of decreasing particle size.

However, the tendency of iron oxides to aggregate under many environmentally relevant conditions can make it difficult to determine whether the observed reactivity of nanoparticle suspensions reflects inherent particle size effects or the behavior of larger particle aggregates. Aggregation influences the transport [90], thermal conductivity [91, 92] and toxicity [93] of nanoparticles. Others [94] have also commented on the likelihood that aggregation impacts nanoparticle redox reactivity by altering the amount of reactive surface area available in suspensions, a scenario that is supported by the relatively few studies that have directly explored the influence of

nanoparticle aggregation on interfacial redox reactivity. For example, recent results of Vikesland et al. [95] demonstrated that the rate of carbon tetrachloride (CCl_4) reduction by nanoscale magnetite decreased with increasing ionic strength, which was varied to control the extent of aggregation in suspensions. Aggregation was also proposed to influence the extent of Fe(II) uptake and the rate of CCl_4 reduction in suspensions of larger goethite particles [96]. These findings agree with earlier work from the field of colloid chemistry, where it has long been recognized that reactivity measurements carried out in wet suspensions will be influenced by the system's dispersivity [97]. These studies suggest that the extent of particle aggregation needs to be considered when assessing whether iron oxides display unique behavioral properties at the nanoscale.

Here, we investigate whether nanoscale size-effects are observed for the reaction of aqueous Fe(II) with goethite. Fe(II) generated from microbial respiration of Fe(III) oxides has been shown to significantly impact oxide dissolution and secondary mineral precipitation, as well as heavy metal sequestration, and contaminant reduction [68, 69, 98-100]. Yet despite the importance of Fe(II)-Fe(III) cycling in these processes, the influence of oxide particle size on this redox couple remains relatively unexplored, as is the case for the many geochemically relevant redox processes [85].

Our work, as well as the work of several others, has shown that sorption of Fe(II) on Fe(III) oxides involves electron transfer between Fe(II) and structural Fe(III) resulting in reductive dissolution and/or some form of secondary mineral formation [99, 101-105]. Previous studies have even suggested that this electron exchange reaction may be impacted by particle size [106-108]. Mulvaney and coworkers (1988a, 1988b,1990) found that the electrons transferred to hematite particles by radiolytically generated viologen radicals could either produce surface-bound Fe(II) or be transferred into the bulk of the oxide particle. Based upon the stoichiometry of the reduction reaction and results of Fe(II) recovery experiments, they proposed that the extent of charge migration into the bulk particle was limited on colloidal iron oxides due to their small bulk volume, in turn producing a greater fraction of surface-bound Fe(II) on nanoparticles relative to larger oxides. Such a scenario has obvious implications for the

biogeochemical cycling of iron, as well as pollutant fate in anoxic, reducing environments; if the extent of Fe(II)-Fe(III) interfacial electron exchange decreases with particle size, then a greater fraction of surface-bound Fe(II) may exist on iron oxide nanoparticles, potentially making smaller oxide phases the dominant player in Fe(II)-Fe(III) redox cycling in natural systems.

For our experimental approach, three sizes of goethite particles were synthesized and their reactivity with Fe(II) was examined in batch systems. We investigated the rate of Fe(II) uptake on goethite, as well as the influence of common geochemical variables such as pH, aqueous Fe(II) concentration and goethite solids loading on the extent of Fe(II) uptake. In addition to traditional batch sorption measurements, we used isotope specific ^{57}Fe Mössbauer spectroscopy to investigate interfacial electron transfer between ^{57}Fe(II)(aq) and structural Fe(III) present within isotopically enriched ^{56}Fe goethite nanoparticles. To gain insights into the fate of Fe(II) on goethite as a function of particle size, complementary recovery studies were also performed in which particles reacted with Fe(II) were resuspended in dilute buffer solutions to examine whether any release of Fe(II) from the reacted particles was observed. Finally, to explore the role of goethite particle size in pollutant fate and transport, we compared the rate of reduction of nitrobenzene, a model groundwater contaminant, in suspensions with Fe(II) and different sizes of goethite.

An important consideration for this work was establishing the appropriate basis for comparing the reactivity of different particle sizes. As is most common for investigations of nanoparticle behavior, size-dependent reactivity trends were developed using properties determined from characterization of dry goethite powders, namely values of specific surface area determined from BET adsorption isotherms and transmission electron microscopy (TEM) particle size analysis. Alternatively, because particle aggregation is inevitable in the near-neutral pH solutions used to investigate Fe(II) reaction with goethite, the contribution of aggregation to our observed size-dependent reactivity trend was also considered. The size and nature of aggregates in suspensions of different goethite particle sizes were estimated using a combination of

techniques including dynamic light scattering, scanning electron microscopy (SEM) imaging of suspended particles, and sedimentation rates determined by monitoring changes in the visible light transmitted through each suspension as a function of time. Comparison of the size-dependent reactivity trend identified from batch studies to the results of dry particle and wet suspension characterization provided an opportunity to explore whether the properties of primary particles or particle aggregates dictate the macroscopic reactivity of goethite toward Fe(II) under environmentally relevant conditions.

Materials and Methods

Reagents

All reagents were used as received. The following chemicals were used during goethite synthesis: ferric nitrate nonahydrate ($Fe(NO_3)_3 \cdot 9H_2O$; Sigma Aldrich; ≥98%), sodium bicarbonate ($NaHCO_3$, Sigma Aldrich, ≥99.5%), and potassium hydroxide (KOH, Sigma Aldrich; ACS Reagent). Stock solutions of Fe(II) (~ 300 mM) were prepared by dissolving anhydrous ferrous chloride beads ($FeCl_2$, Sigma Aldrich, 99.99%) in 0.5 M HCl. Sorption experiments were conducted in buffer solutions of either 4-(2-hydroxyethyl)-1-piperazineethanesulfonic acid (HEPES; Sigma Aldrich, ≥99.5%) or piperazine-N,N'-bis(ethanesulfonic acid) (PIPES, Sigma Aldrich, ≥99%) with potassium bromide (KBr; Fisher, ACS Reagent grade). All solutions in sorption and reactivity experiments were degassed prior to use by sparging with high purity N_2 for 1 h/L and were stored in an anaerobic chamber with an atmosphere of 95% N_2 and 5% H_2. Measurements of dissolved Fe(II) and total dissolved iron were performed with 1,10-phenanthroline (Sigma-Aldrich, ≥ 99%), hydroxylamine hydrochloride (Sigma Aldrich, 98%) and a buffer from ammonium acetate (Fisher, 98.5%) and glacial acetic acid (EMD, 99.7%).

Goethite Synthesis

Three primary particles sizes of goethite were synthesized. The largest particles, referred to as microrods, were synthesized according to Schwertmann and Cornell

[109]. Briefly, 180 mL of 5 M KOH was rapidly added to 100 mL of 1 M $Fe(NO_3)_3$. The mixture was diluted with distilled water to a final volume of 2 L and was then held in a closed polyethylene flask at 70 °C for 60 h. Goethite nanoparticles, referred to as nanorods, were synthesized according to a modified version of the method provided by Burleson and Penn for goethite synthesis from ferrihydrite [110], in which 1 L of 0.48 M $NaHCO_3$ solution was added dropwise (rate of approximately 4.5 mL/min) to an equal volume of 0.4 M $Fe(NO_3)_3$ that was being vigorously stirred. During this titration, the pH of the ferric nitrate solution increased from approximately 1.0 to 2.4. The resulting suspension was then microwaved to boiling, immediately cooled to ~ 20 °C using an ice bath, and purified via dialysis for three days according to the details provided in Anschutz and Penn [86]. Conversion of the resulting ferrihydrite particles to goethite was accomplished by first raising the pH to 12 using 5 M KOH and then heating the resulting suspension at 90 °C for 24 h. In all instances, goethite particles were purified via three cycles of water washes and centrifugation. Particles were then freeze-dried, ground by mortar and pestle and passed through a 150 μm or 45 μm sieve for microrods and nanorods, respectively.

An intermediate size of goethite particle was synthesized by following a protocol adapted from that used for goethite nanoparticles. An 0.2 M ferric iron solution was prepared by dissolving iron metal (Fe(0); Aldrich, 99%) in 0.5 M HCl rather than using a ferric nitrate starting solution. After several days to allow for near complete dissolution of the iron metal, this solution was oxidized with excess 30% H_2O_2, and subsequently filtered to remove any undissolved iron metal. The pH of this ferric iron solution was first increased to 1.0 via the dropwise addition (rate of ~ 1 mL/min) of 5 M KOH, then an 0.24 M sodium bicarbonate solution was added at the same rate until a pH of 2.4 was attained. The resulting suspension was microwaved and purified via dialysis as described above. Then, 5 M KOH was used to raise the pH of the suspension to 13, followed by the baking, washing and drying steps described for nanorods and microrods.

As in our earlier work [102, 103], isotopically enriched goethite nanoparticles were synthesized from a starting material of isotopically enriched [56]Fe(0)

to explore Fe(II)-Fe(III) electron transfer. Briefly, a solution of 50 mM Fe(III) was prepared by dissolving [56]Fe(0) in 0.5 M HCl as described previously for the synthesis of intermediate rods. As a result of the greater acidity and higher ionic strength of the resulting [56]Fe(III) solution relative to the ferric nitrate solution used during synthesis of istotopically normal nanorods, a modified procedure was required. First, a 5 M KOH solution was added in a dropwise manner to increase the pH of this solution to 1.9 (which was the pH of an equivalent ferric nitrate solution), followed by the dropwise addition of a 60 mM bicarbonate solution to achieve a final pH of 2.4. Following the method of Penn et al. [111], the ferric iron solution was immersed in an ice bath during the addition of these bases. The lower temperature controls the size of ferrihydrite particles generated during this hydrolysis step [111]. Finally, rather than baking the final suspension in an oven at 90 °C for 24 h , we aged the suspension at room temperature for 1 week, during which time the suspension changed color from light brown to the brownish-orange color typical of goethite. To ensure full conversion to goethite, the aged suspension was placed in an oven at 40 °C for 24 h prior to washing and freeze-drying as described above.

Characterization of Goethite Powders

Freeze-dried goethite particles were characterized via powder X-ray diffraction (XRD) using a Bruker D-5000 diffractometer with a Cu Ka source. Additional oxide characterization was performed using 57Fe Mössbauer spectroscopy using the system described by Larese-Casanova and Scherer [103]. The specific surface area of all powders was determined from seven-point N2-BET adsorption isotherms performed on a Quantachrome Nova 1200 surface area analyzer. The size and morphology of primary goethite particles were determined using TEM. For TEM primary particle size analysis, suspensions (~ 0.2 g/L) of each particles size were prepared in methanol and sonicated for at least 1 h. A drop of this suspension was then applied to a carbon-coated Cu TEM grid (400 mesh; EMS). Images of goethite particles were collected on a JEOL JEM-1230 transmission electron microscope operated at a 100 keV accelerating voltage. Digital

images were acquired using a Gatan UltraScan CCD camera with Gatan imaging software. The size of goethite particles was then determined by analyzing TEM images in the software package Image J.

Characterization of Aqueous Goethite Suspensions

Dynamic light scattering (DLS) was used to obtain information regarding the relative size of particles in nanorod and microrod suspensions. All DLS measurements were made with a Zeta Sizer S series from Malvern instruments operated at a laser wavelength of 532 nm. Suspensions for DLS analysis consisted of goethite concentrations ranging from 0.05 – 0.2 g/L, a pH of either 2 (0.01 N HCl) or 7.5 (25 mM HEPES buffer), and the ionic strength of all suspensions was adjusted to 25 mM with KBr. For pH 7.5 suspensions, independent experiments revealed that ionic strength had little influence on goethite aggregation for solutions with KBr concentrations as high as 1 M (data not shown). All solutions were passed through a 0.2 mm nylon syringe filter prior to addition of solid to minimize contamination from dust. All suspensions were prepared 24 h prior to DLS analysis and were not sonicated prior to light scattering measurements. For a typical analysis, 1 mL of a well-mixed suspension was delivered to a 1 cm pathlength cuvette, and the suspension was allowed to sit for approximately 30 seconds prior to analysis to allow any extremely large aggregates to settle out of solution.

Because DLS could only be performed on relatively dilute suspensions (< 0.2 g/L), qualitative insights regarding the size of particles in concentrated suspensions more representative of our sorption studies were obtained using UV/visible spectrophotometry to measure rates of particle sedimentation. This approach has previously been used to monitor to the stability and rates of aggregation in suspensions of zero-valent iron nanoparticles [112, 113]. Goethite suspensions were added to a 1 cm pathlength cuvette and the change in transmitted light (l = 510 nm) was monitored as a function of time. Suspensions were prepared as described for DLS analysis, with goethite concentrations ranging anywhere between 0.02 and 1 g/L. For this range of

goethite concentrations, we observed a linear relationship between the absorbance values reported by the UV/visible spectrophotometer and the mass loading of goethite.

To complement DLS and sedimentation results, additional suspension characterization was accomplished using a Hitachi S-4800 SEM. Nanorod and microrod suspensions were prepared at pH 2 and pH 7.5 with loadings of 0.2 g/L, conditions identical to those used in DLS and sedimentation studies. A drop of suspension was applied to the SEM sample stub, and rather than allowing the solution to air dry, which likely would alter the aggregation state of the particles, the sample stub was immediately transferred to a -20°C freezer for 30 minutes. The sample stub was then placed in a freeze dry vessel to sublimate off the frozen solution. Because dried electrolyte and buffer would limit our ability to clearly image the particles in suspension, the freeze-dried sample was washed with a few drops of deionized water, which was then removed from the sample by repeating the freezing and freeze-drying steps.

Fe(II) Sorption Experiments

All experiments investigating Fe(II) sorption on goethite were performed within an anoxic glove box. Unless otherwise noted, all experiments were conducted in the dark with well-mixed reactors containing 25 mM HEPES with 25 mM KBr at pH 7.5. Prior to the addition of goethite to the reactors, the buffer solution was allowed to equilibrate for at least 1 h after the addition of aqueous $FeCl_2$ solution. This solution was then passed through a 0.2 mm filter to remove any precipitates that may have accumulated from the initial spike of Fe(II), and the aqueous Fe(II) concentration was measured.

Experiments investigating the rate of Fe(II) sorption were conducted with a goethite loading of 4 g/L, an initial dissolved Fe(II) concentration of ~1 mM, and reactors were mixed end-over-end at a rate of ~10 rpm. Sorption isotherms for Fe(II) used a goethite loading of either 1 or 2 g/L and initial Fe(II) concentrations ranging from 0.1-5 mM. The extent of Fe(II) sorption as a function of pH was investigated in reactors with pH values ranging from 6.1-7.5. These experiments used a 25 mM PIPES buffer with 25

mM KBr, a goethite concentration of 1 g/L, and an initial Fe(II) concentration of ~1 mM. For isotherm and pH-edge experiments, reactors were mixed end-over-end at approximately 45 rpm and were allowed to equilibrate for at least 1 h, at which time the aqueous Fe(II) concentration was determined by filtering a portion of the oxide slurry. The loss of aqueous Fe(II) was determined by the difference between the concentration of Fe(II) prior to the addition of the oxide phase compared to the concentration after equilibration.

Additional studies examined the extent of Fe(II) sorption over the range of goethite loadings from 0.2-20 g/L at pH 7.5 in solutions of 25 mM HEPES with 25 mM KBr. In these reactor systems, the ratio of goethite mass loading to initial dissolved Fe(II) concentration was held constant at a value of 0.25 mmole of Fe(II) per g of goethite. Accordingly, for goethite concentrations of 0.2, 2 and 20 g/L, initial dissolved Fe(II) concentrations of 0.05, 0.5 and 5 mM were used, respectively.

Reaction of ^{57}Fe(II) with ^{56}Fe Goethite

Experiments investigating Fe(II)-Fe(III) electron exchange followed the procedures listed above, but instead used isotopically enriched ^{56}Fe goethite particles and a ^{57}FeCl$_2$ solution. Mössbauer spectroscopy was used to examine the products of the reaction between ^{57}Fe(II)(aq) and ^{56}Fe goethite. Reacted goethite particles were collected on 13 mm filter discs and mounted as a wet paste between two layers of Kapton tape for analysis. All measurements were made on the Mössbauer spectroscopy system described in Larese-Casanova and Scherer [103].

Fe(II) Recovery Experiments

We also examined whether the Fe(II)(aq) that had been reacted with goethite could be recovered. According to the procedures already described, goethite particles were reacted with a range of aqueous Fe(II) concentrations in suspensions containing 2 g/L goethite at pH 7.5 (25 mM HEPES with 25 mM KBr). After equilibration, the concentration of aqueous Fe(II) was measured, and the suspension was centrifuged. The supernatant was discarded, and the reacted particles were resuspended in a more

dilute solution of Fe(II)(aq) and transferred to a new glass vial. These new reactors were allowed to equilibrate for approximately 1 h, at which time the solution phase concentration of Fe(II) was measured.

Nitrobenzene Reduction Experiments

The reduction of nitrobenzene was examined in goethite suspensions containing Fe(II). Reactions were conducted at pH 7.5 (25 mM HEPES with 25 mM KBr) and contained an initial nitrobenzene concentration of approximately 100 mM, an initial aqueous Fe(II) concentration of 1 mM and 0.25 g/L goethite. Nitrobenzene was added as a methanolic spike to a suspension of goethite that had been equilibrated with Fe(II) according to the methods used in sorption experiments. Samples of the goethite slurry were periodically removed from the reactor, passed through a 0.2 mm PTFE syringe filter to quench the reaction and transferred to a crimp-sealed autosampler vial for HPLC analysis.

Chemical Analyses

Dissolved Fe(II) concentrations were measured colorimetrically with the 1,10-phenanthroline method at 510 nm on a UV/visible spectrophotometer according to the procedure detailed by Larese-Casanova and Scherer [103]. Analysis of nitrobenzene and its reduction products were performed via HPLC. Details regarding the system and conditions used for nitrobenzene analysis can be found elsewhere [102].

Results

Primary Particle Characterization

We have adopted a nomenclature for goethite particles similar to that introduced by Anschutz and Penn [86], and refer to the different particle sizes as nanorods, intermediate rods and microrods. Properties determined from the characterization of freeze-dried powders of each synthetic goethite are summarized in Table A.1, whereas TEM images showing the acicular, or rod-like, morphology of each

primary particle size are shown in Figure A1. For TEM analysis, particles indicative of other iron oxide phases were not observed, suggesting near-complete transformation of ferrihydrite to goethite during the aging step of all synthetic procedures.

XRD patterns were consistent with goethite, and the pattern for nanorods revealed considerable line broadening, which was anticipated due to the lower degree of crystallinity resulting from their nanoscale dimensions. For all samples, ^{57}Fe Mössbauer spectra and the corresponding model fits were also consistent with those anticipated for goethite (see electronic annex Figure A.12). Our Mössbauer detection limit determined from mixtures of ferrihydrite and goethite was approximately 3% ferrihydrite by mass, which provides an upper limit as to how much ferrihyrite might be present. Notably, Mössbauer spectra collected at 298 (room temperature), 250 and 140 K revealed less magnetic ordering in nanorods relative to microrods, behavior that is often attributable to smaller particles [114, 115]. Differences in magnetic ordering observed from the Mössbauer characterization of these particles were subtle, however, and by 77 K, both the nanorods and microrods had achieved full magnetic ordering.

The distribution of nanorod dimensions was determined from TEM analysis of 530 unagreggated particles (Figure A2). On average, nanorods were 80 nm long and 7 nm wide, slightly larger than the nanorods prepared by Anshutz and Penn [86] using the same synthesis procedure. Size distributions for the intermediate rods and microrods were determined from smaller sample sizes (n = 240 and 285, respectively). This was due in part to the greater tendency of these particles to exist as dense aggregates when dispersed and dried on TEM grids, and sonication of these suspensions prior to imaging failed to improve their dispersion. Microrods were roughly 670 nm in length and 25 nm in width, but exhibited a much broader size distribution, as indicated by the rather large standard deviations associated with their dimensions. The size distribution for the intermediate rods, which were approximately 330 nm long and 14 nm wide, was also relatively broad. In fact, there is a relatively large overlap for the particle size distributions of intermediate rods and microrods.

Nanorods exhibited the highest specific surface area of 110 (± 7) m^2/g, as determined from seven-point N$_2$-BET adsorption measurements performed in triplicate (uncertainty represents one standard deviation). Specific surface areas for the intermediate rods (55 m^2/g) and microrods (40 ± 3 m^2/g) were smaller by roughly a factor of 2 and 3, respectively. Goethite specific surface areas were also approximated from the average rod dimensions in Table A.1 using the approach of Anschutz and Penn [86], who modeled goethite rods as rhomboidal prisms bounded by [116]. These values, assuming a goethite density of 4.26 g/cm^3 [82], are also included in Table A.1, and the relationship between particle dimensions (length and width) and specific surface area calculated assuming this geometry is displayed in electronic annex Figure A.13. Although some variation exists between specific surface areas determined from BET measurements and those estimated from particle geometry, the trend of increasing specific surface area with decreasing particle size holds true for both sets of values.

Isotopically enriched ^{56}Fe nanorods were nearly identical to nanorods prepared from isotopically normal iron starting materials. A TEM image of these particles is shown in electronic annex Figure A.14, which reveals that these primary particles had a greater tendency to adhere to one another relative to isotopically normal nanorods. The X-ray diffraction pattern for ^{56}Fe nanorods was consistent with goethite and revealed the expected line broadening. Furthermore, their specific surface area and size distribution were similar to those obtained for the nanorods synthesized from isotopically normal materials (Table A.1).

<div align="center">Characterization of Goethite Suspensions</div>

Visual inspection suggested that all sizes of goethite extensively aggregated in pH 7.5 suspensions, as large aggregates settled out of solution if the suspensions were not mixed. Figure A3 illustrates the role of solids concentration on aggregate settling rates at pH 7.5. Rather than plotting transmitted light as a function of time, we report normalized absorbance measurements (A/A$_0$), assuming that absorbances measured by the UV/visible spectrophotometer account primarily for scattered light. We reiterate

that suspensions were prepared 24 h prior to conducting sedimentation measurements and were not sonicated prior to the experiment. Thus, rates of sedimentation shown in Figure A3 reflect the aggregates in our suspensions at what we assume to be steady state.

The initial change (for t ≤ 10 min) in normalized absorbance over time adhered to exponential decay, allowing initial rate coefficients for settling to be determined from semilog plots of normalized absorbance versus time. Initial rate constants were comparable in nanorod and microrod suspensions, ranging from approximately 0.03 – 0.05 min^{-1} for nanorods and from 0.02-0.04 min^{-1} for microrods over the solid loadings investigated. Over time, the rate of aggregate settling slowed in all suspensions, and normalized absorbance values approached a stable value after roughly two hours. This behavior is most clearly observed for the 0.02 g/L suspensions of microrods and nanorods, which indicates that some fraction of the suspended particles either do not settle out of solution or do so at a very slow rate. At these longer timescales, higher goethite concentrations resulted in lower values of A/A_0, consistent with a greater extent of particle settling with increasing solids loading. Also note that over the entire experimental duration, values of A/A_0 were greater in microrod suspensions than the values observed in the corresponding nanorod suspensions.

Intensity-weighted size distributions determined from DLS analysis of pH 2.0 and pH 7.5 goethite suspensions are shown in Figure A4. For pH 2.0 suspensions, nanorod and microrod size distributions are presented for solids concentrations of 0.01 g/L and a 0.2 g/L because these distributions are representative of all solid loadings analyzed over this range. Generally, no systematic trend in size distribution with increasing solid loading was observed for either particle size. In all, thirteen different analyses were conducted with nanorod suspensions at pH 2, and the mean hydrodynamic diameter from these distributions was determined to be 130 (± 20) nm. Similarly, eight different analysis were conducted with microrod suspensions at pH 2, yielding an average hydrodynamic diameter of 550 (± 160) nm.

We also present in Figure A4 intensity weighted sized distributions for suspensions at pH 7.5. Shown are replicate measurements performed on a 0.2 g/L suspension of each particle size. Nanorod suspensions were analyzed in quadruplicate and produced an average hydrodynamic diameter 1600 (± 600) nm, which is nearly an order of magnitude greater than the hydrodynamic diameter determined at pH 2.0. A comparable hydrodynamic diameter of 1500 (± 200) nm was determined from triplicate analysis of a microrod suspension at pH 7.5. In fact, as is observed in Figure A4, the size distributions measured at pH 7.5 for the microrod suspension essentially overlapped with the distributions measured for nanorods.

Representative SEM images of the particles in 0.2 g/L nanorod and microrod suspensions at pH 2 and 7.5 are shown in Figure A5. For nanorods, SEM images revealed that pH 2 suspensions consisted primarily of well-dispersed or loosely packed individual nanorods, although aggregates typically less than 1 μm in diameter were occasionally observed. At pH 7.5, on the other hand, images revealed a predominance of relatively large and dense aggregates that were typically on the order of a few microns, but sometimes as large as 30 μm. The dense nature of these nanorod aggregates is shown in the inset in Figure A5, which is a high magnification image of the surface of a nanorod aggregate.

Similar observations were made for microrod suspensions at pH 2 and 7.5. At pH 2, a number of well-dispersed or loosely associated microrods were clearly observed, whereas aggregates were rarely found. In contrast, larger aggregates were frequently encountered at pH 7.5, typically ranging between 5-10 μm, although aggregates with diameters up to 30 μm were sometimes observed. Notably, SEM images of pH 7.5 suspensions suggest that there are a greater number of individually dispersed microrods relative to freely dispersed nanorods.

Recall that sedimentation studies indicated that a fraction of the particles in suspensions at pH 7.5 either did not settle or did so at a very slow rate. SEM images of suspensions taken after 30 min of settling reveal that the relatively stable particles consist primarily of small aggregates ranging from 0.5 -1 μm in nanorod systems,

whereas in microrods systems, a mixture of individually dispersed microrods and small aggregates typically on the order of a couple of microns was observed (see electronic annex Figure A.15).

Fe(II) Sorption on Goethite

Fe(II) sorption isotherms collected for pH 7.5 suspensions of each goethite particle size are shown in Figure A6. Independent experiments (Figure A7) revealed that the density of sorbed Fe(II) in both nanorod and microrod suspensions was comparable over a much broader range of mass loadings than those used to construct the sorption isotherms presented in Figure A6.

Sorption isotherms for Fe(II) revealed relatively small differences in the concentrations of sorbed Fe(II) per gram of goethite determined for each particle size. Whereas sorption data for intermediate rods and microrods were essentially identical, sorbed concentrations of Fe(II) on the nanorods were slightly greater than the values measured with larger particles. This result is most easily observed from the Fe(II) sorption densities reported in Figure A7, in which densities measured for nanorods were on average 1.3 (± 0.1) times greater than the values measured in the corresponding microrod system. Figures A6 and A7 also reveal, however, that the increase in Fe(II) uptake on nanorods was often within the uncertainty associated with measurements of sorbed Fe(II) concentration, which was determined from replicate experiments.

Additional experiments examined whether the rate of Fe(II) sorption (electronic annex Figure A.16a) or the extent of Fe(II) sorption as a function of pH (electronic annex Figure A.16b) exhibited more pronounced variations between nanorod and microrod systems containing equivalent goethite mass. Consistent with the results of our Fe(II) isotherms, only a modest increase in the rate and extent of Fe(II) sorption was observed for nanorods relative to the behavior observed in otherwise identical microrod suspensions.

Fe(II)-Fe(III) Interfacial Electron Transfer on Goethite

Temperature profiles of Mössbauer spectra collected after the reaction of 0.25 mM aqueous ^{57}Fe(II) with suspensions containing 2 g/L of either ^{56}Fe goethite nanorods or microrods are shown in Figure A8. For both nanorods and microrods, these conditions produced an equivalent concentration of 0.11 mmoles of sorbed ^{57}Fe per gram of ^{56}Fe goethite. The resulting temperature profiles for ^{56}Fe nanorods and ^{56}Fe microrods reacted with ^{57}Fe(II)(aq) revealed nearly identical ferric iron sextets, suggesting that electron transfer had occurred between sorbed ^{57}Fe(II) and structural ^{56}Fe(III) present within the goethite. As in our earlier study with ^{56}Fe microrods (Williams and Scherer, 2004), model fit parameters for the 13 K spectra suggested that these sextets correspond to goethite with a low degree of magnetic ordering.

As confirmation that the aqueous ^{57}Fe(II) was oxidized by structural ^{56}Fe(III) in the nanorods and not by trace oxidants in our system, we dissolved the reacted goethite nanoparticles in ~ 3 M HCl and subsequently measured the dissolved Fe(II) concentration. To account for the background signal of Fe(III) generated from goethite dissolution, we subtracted the absorbance measured in samples of dissolved goethite without Fe(II). This procedure typically resulted in near complete (95-100%) recovery of the sorbed Fe(II), providing further evidence that the Mössbauer spectra in Figure A8 reflect oxidation of the sorbed Fe(II) by goethite.

Recovery of Fe(II) after Reaction with Goethite Nanorods and Microrods

The results of recovery experiments used to explore the fate of the Fe(II) species generated from interfacial electron exchange are shown in Figure A9. Open symbols correspond to the sorbed and aqueous Fe(II) concentrations measured after fresh goethite particles were equilibrated with aqueous solutions containing variable concentrations of Fe(II). Solid symbols indicate the concentrations of sorbed and aqueous Fe(II) determined after these reacted particles were recovered via centrifugation, resuspended and equilibrated with a new, more dilute Fe(II) solution. We observed relatively good agreement between Fe(II) concentration data collected from sorption and recovery experiments, suggesting that most of the Fe(II) species

generated via interfacial electron transfer was released back into solution upon dilution. Our ability to recover Fe(II) was independent of the size of goethite particles used in sorption and recovery experiments.

Nitrobenzene Reduction by Fe(II) in the Presence of Goethite

Under our experimental conditions (0.25 g/L goethite, pH 7.5, 1 mM initial dissolved Fe(II) concentration), roughly 15-20% of the initial aqueous Fe(II) concentration was sorbed in the nanorod and microrod suspensions. In both systems, nitrobenzene was rapidly reduced, and the end product of the reaction was aniline. Near complete transformation of nitrobenzene was observed over the course of 1 h.

For both sizes of goethite particles, the concentration profile for nitrobenzene as a function of time generally followed exponential decay, although a moderately steep (and reproducible) decrease in the concentration of nitrobenzene was observed by the first sampling point (t ~ 1 min) in nanorod systems. Pseudo-first-order rate constants for the reduction of nitrobenzene (k_{obs} values) were determined from plots of the natural log of nitrobenzene concentration versus time (Figure A10) and equaled $(2.6 \pm 0.4) \times 10^3$ s^{-1} and $(1.8 \pm 0.1) \times 10^3$ s^{-1} for nanorods and microrods, respectively. Values of k_{obs} indicate only a modest increase in the rate of nitrobenzene reduction in nanorod systems on the basis of goethite mass loading. Moreover, as the experimental conditions chosen for these experiments resulted in a comparable amount of sorbed Fe(II) in both nanorod and microrod suspensions, little change in their relative reactivity was observed when k_{obs} values were normalized by the concentration of sorbed Fe(II).

Discussion

Aggregation of Suspended Goethite Particles

Goethite nanorods and microrods aggregate in pH 7.5 suspensions. Aggregate formation is clearly shown in SEM images (Figure A5), with additional evidence from sedimentation studies and DLS analysis. The mean hydrodynamic diameter estimated

for particles in nanorod suspensions at pH 7.5 was roughly one order of magnitude greater than the corresponding value measured at pH 2. Although the magnitude of increase was not as great in microrod suspensions, the average hydrodynamic diameter at pH 7.5 was still greater than that observed at pH 2. Such results illustrate the control that solution pH exerts on the stability of goethite suspensions.

A dominant role for pH in suspension stability is anticipated from DLVO theory [117], which is widely applied to explain aggregation in colloidal suspensions. At low pH values (e.g., pH 2.0), protonation of surface hydroxyl groups produces a net positive surface charge that, due to unfavorable electrostatic interactions, minimizes aggregation. As a result, the mean hydrodynamic diameter measured at pH 2.0 for nanorods (~ 130 nm) agrees reasonably well with the nanorod dimensions determined from characterization of dry goethite powders (80 × 7 nm), especially since we did not use any algorithms to correct for the acicular nature of our particles In contrast, pH 7.5 is nearer to the pH at which the net surface charge on goethite is zero (reported range of pH_{zpc} 7.5-9.5; [82]), a condition that increases particle-particle interactions and results in aggregate formation.

Results from DLS analysis and sedimentation studies also appear to suggest that the aggregates in nanorod and microrod suspensions at pH 7.5 are of comparable size. Specifically, mean hydrodynamic diameters in both systems were on the order of 1 micron at pH 7.5. Furthermore, the comparable rates of nanorod and microrod settling could also be interpreted as evidence that similarly sized aggregates were present in both systems. Unfortunately, both approaches have limitations; sedimentation velocities are influenced by a variety of factors including the permeability and density of the aggregates [118], which were not rigorously quantified for our experimental systems, whereas DLS analysis requires suspensions with non-settling particles moving entirely as a result of Brownian motion [119]. Although our application of DLS to pH 2 goethite suspensions meets this requirement (sedimentation plots show that both suspensions are essentially stable at pH 2, see electronic annex Figure A.17), our unstable pH 7.5 suspensions likely pushed this approach to its analytical limits.

The most definitive evidence as to the relative size and nature of the particles in suspension at pH 7.5 is provided by the images from SEM (see Figure A5). These images support a scenario in which aggregates of nanorods are of comparable size to the aggregates encountered in microrod suspensions, as aggregates generally on the order of 5-10 μm are found in both systems. There are also a fewer number of primary particles dispersed in nanorod suspensions, and the nanorod aggregates appear to be much denser. It seems, therefore, that nanorods aggregate more extensively than microrods at pH 7.5, resulting in denser aggregates and fewer primary particles suspended in solution.

<div align="center">Influence of Goethite Particle Size on Fe(II) Sorption and
Contaminant Reduction</div>

Little difference with regards to Fe(II) sorption and contaminant reduction was observed over the range of primary particle sizes used in our study. On the basis of mass, Fe(II) sorption isotherms and rates of nitrobenzene reduction appear nearly independent of goethite particle size. Thus, the significant enhancements in rates or extent of reaction that we had originally hypothesized were not observed. The lack of significant increases in reactivity contrasts several previous reports in which nanoparticles generally outperform larger particles on a mass basis (e.g., see review by Savage and Diallo [120] and references therein).

For investigations of nanoparticle reactivity, the influence of particle size is traditionally determined by normalizing measures of reactivity (e.g., sorbate concentrations or reaction rate constants) to a primary particle characteristic determined from the characterization of dry nanoparticles. The most widely used property is specific surface area, which is often assumed to be representative, or at least a good indicator, of reactive surface area. Nanoscale size-effects are then identified by determining whether nanoparticles display enhanced reactivity beyond that expected from their greater surface area.

In Figure A11, we plot our Fe(II) sorption isotherms normalized to BET surface area. A clear trend emerges that implies that the amount of Fe(II) sorbed per m^2 of

goethite decreases with decreasing particle size. A similar trend is observed if we normalize our rate constants for nitrobenzene reduction by BET surface area, which yields surface-area-normalized rate constants (or k_{SA} values) of 2.3 ($\pm$ 0.4) $\times$ 10^6 and 4.4 ($\pm$ 0.3) $\times$ 10^6 L·m^2·s^{-1} for nanorods and microrods, respectively. The lower observed reactivity of the nanorods is not limited to specific surface areas derived from BET measurements, as the use of specific surface areas estimated from particle geometries obtained with TEM (Table A.1) produced the same trend.

That smaller k_{SA} values and less Fe(II) sorbed per m^2 are observed for nanorods again runs counter to the typical trends commonly associated with nanoparticles. Both reactivity and sorption capacity per unit surface area are often expected to increase as particle sizes approach the nanoscale. Indeed, there are many examples of where significant increases in reactivity of nanoparticles have been observed. Sorption studies by Zhang et al. [121] reported as much as a 70-fold increase in the sorption coefficients of simple organic acids on 6 nm TiO$_2$ particles relative to 16 nm TiO$_2$ material, and a more recent study by Mayo et al. [122] reported enhanced uptake of arsenic on 12 nm magnetite nanoparticles relative to larger particles that could not be attributed to differences in surface area. With respect to reaction rates, larger k_{SA} values have been observed for the reduction of carbon tetrachloride by 9 nm magnetite particles compared to values measured with 80 nm particles [95], and surface-area normalized rates of hematite [87] and goethite [86] reductive dissolution have also been shown to increase with decreasing particle size.

There are, however, a few others that have also observed less reactivity with smaller particles on the basis of surface area. Most notable for comparison to this work are two studies which investigated the size-dependent sorption of Hg(II), protons, and carbonate on goethite. For Hg(II) sorption, Waychunas et al. [81] observed a similar size dependence on the basis of goethite surface area for particles ranging from 5 to 75 nm that were prepared via nearly the same synthetic methods used here. Likewise, Villalobos et al. [123] also measured less proton and carbonate sorption per m^2 on

goethite rods with specific surface areas (45 and 94 m^2/g) that were quite close to our microrods and nanorods.

The lesser reactivity of the goethite nanoparticles in these prior studies was attributed to different phenomena. In the proton and carbonate sorption study, the lesser reactivity was interpreted as evidence that the density of reactive goethite sites (i.e., sites per m^2) decreases as particle size becomes smaller. In the Hg(II) study, on the other hand, the size-dependent reactivity trend was attributed to increased curvature of nanoparticle surfaces resulting in distorted Fe(III)(O,OH)$_6$ octahedra and thus a poorer coordination environment for metal surface complexation. Their hypothesis of distorted octahedra was supported by EXAFS measurements that revealed a ~0.2 Å increase in the Hg-Fe interatomic distance for the smallest (highest specific surface area) goethite particles relative to the largest (smallest specific surface area) goethite particles studied. Additional explanations for the lesser reactivity of the smaller particles may also be related to differences in the manner charge accumulates on nanoparticle surfaces [124] or to the relative amounts of specific crystal faces available on nanorods in comparison to microrods [125].

Influence of Aggregation on Fe(II) Sorption and Reactivity

An alternative explanation for the lesser reactivity of the nanorods we observed here is loss of reactive surface area due to aggregation. Based upon SEM images, DLS analysis, and sedimentation studies, we can reasonably conclude that goethite nanorods and microrods both aggregate at pH 7.5, which introduces uncertainty as to whether macroscopic observations of material reactivity reflect the behavior of the aggregate or the nanoparticles comprising the aggregate [94]. The size-dependent behavior suggested from the surface-area normalized isotherms in Figure A11 could, therefore, simply be an artifact resulting from the inappropriate use of primary particle surface area for normalization.

Aggregation may also influence the results of studies exploring interfacial Fe(II)-Fe(III) electron exchange in nanorod and microrod suspensions. From Mössbauer

spectroscopy and the results of our Fe(II) recovery experiments, we found that the products of electron exchange are of a nearly identical nature for each particle size and that the Fe(II) species generated via this process displays comparable behavior upon resuspension of each particle size after reaction. Both observations were unexpected; we initially anticipated the surface coating on less ordered nanorods to be more poorly ordered than the microrod coating, and previously, we found that the Fe(II) created after Fe(II)-Fe(III) electron transfer on hematite could not be recovered [103]. Furthermore, Mulvaney et al. [106] provided experimental evidence that the fate of Fe(II) generated by the reduction of iron oxides depends upon particle size, with larger particles having a greater tendency for charge migration into the bulk of the oxide where the Fe(II) could not be recovered via chemical extraction. We saw no evidence to support such a scenario, as our recovery studies illustrate that the Fe(II) generated from goethite reduction is equally susceptible to recovery from both particle sizes. We suspect such similarities are also a consequence of the extensive aggregation occurring in nanorod suspensions, ultimately producing particles that are typically within the range of particle sizes encountered in microrod suspensions.

Although the implications of aggregation on the environmental transport of nanoparticles are well-recognized [89], its impact on reactivity in environmentally relevant systems has not been widely considered in previous investigations. Often times, a response in particle reactivity to variations in ionic strength, which will affect suspension stability, is used to infer a role for aggregation in altering the reactivity of colloidal or nanoparticle suspensions [95, 97]. Another approach was employed by Amonette et al. [96], who interpreted a systematic decrease in the amount of sorbed Fe(II) per gram of goethite with increasing goethite loading as a result of aggregation in their microrod suspensions. Recall, however, that this behavior was not observed in the current study, as the amount of Fe(II) sorbed per gram of goethite was relatively constant in both microrod and nanorod systems for goethite concentrations ranging from 0.02 to 20 g/L (Figure A7), which may indicate that the size of aggregates does not

change appreciably over the range of goethite concentrations employed in Fe(II) batch sorption studies.

Conclusions

Results from both batch and spectroscopic investigations revealed little difference in the reactivity of goethite nanorods and microrods with regard to Fe(II) sorption, Fe(II)-Fe(III) interfacial electron transfer, and nitrobenzene reduction on a mass-normalized basis. SEM images, DLS analysis, and sedimentation studies all indicate that aggregation occurs in near-neutral pH suspensions of goethite nanorods and microrods. Taken together, these findings illustrate the challenges frequently encountered when evaluating whether nanoparticles display size-dependent reactivity in environmentally relevant systems. Specifically, it is difficult to quantify reactive surface area in aggregating systems, particularly when different primary particle sizes display different aggregation behavior.

Based upon SEM images, DLS analysis, and sedimentation studies, we contend that the amount of reactive surface area in our goethite suspensions is unknown. Clearly, the extensive aggregation we observed indicates that the reactive surface area is less than what would be predicted from our BET measurements, but exactly how much less is difficult to assess. Consequently, presenting our experimental results as evidence that nanorods are inherently less reactive toward Fe(II) uptake and nitrobenzene reduction than larger particles on the basis of primary particle specific surface area is suspect. In fact, the nearly equivalent reactivity observed for nanorod and microrod systems on the basis of particle mass could be interpreted as evidence that the reactive surface area is roughly equivalent in the pH 7.5 suspensions that consist primarily of aggregates of each particle size.

Many previous studies have fit macroscopic sorption data similar to the data we collected here and concluded that differences in amount of sorption were due to either differences in surface site density or intrinsic reactivities. For example, the distorted surface octahedra on nanoscale goethite particles observed by Waychunas et al. [81]

could be interpreted to produce a lower intrinsic reactivity of the nanorod surface, whereas the observation of less proton and carbonate uptake on goethite nanoparticles was modeled by invoking a decrease in surface site density with decreasing particle size [123]. Both represent viable explanations for the depressed reactivity of goethite nanorods with respect to Fe(II) sorption that we have observed here on the basis of primary particle surface area. In fact, our Fe(II) sorption results are remarkably consistent with the findings of Villalobos et al. [123], as their site densities of 8.6 μmoles/m^2 on goethite particles similar to our microrods (SA_{BET} = 45 m^2/g) and 3.0 μmoles/m^2 for particles comparable to our nanorods (SA_{BET} = 94 m^2/g) correspond reasonably well our isotherm data (as illustrated by the dashed lines in Figure A11).

Such conclusions regarding surface site density and intrinsic reactivity, however, are based on the assumption that the dry particle surface area is the same as the reactive surface area in a wet suspension. We argue, and demonstrate, that when that assumption is no longer valid (i.e., in an aggregated suspension), it is no longer possible to isolate whether the differences in sorption are due to differences in *i*) intrinsic reactivity of a site, *ii*) site densities, or *iii*) changes in available surface area. With this data set, we show that the exercise of fitting sorption isotherms to determine site densities or intrinsic reactivities when particles aggregate is not appropriate. The "reactive" surface area has changed due to aggregation, and with this number unknown, the fitted isotherm parameters are no longer meaningful. We emphasize, as have others before us (e.g., Nurmi et al. (2005)), that the role of aggregation must be considered when attempting to evaluate nanoscale effects based upon the behavior and reactivity of particle suspensions.

Acknowledgements

(NSE) Program through a Nanoscale Interdisciplinary Research Team (NIRT) award (EAR-0506679).

Table A.1. Properties determined from the characterization of freeze-dried powders of the goethite particles synthesized in the current study.

	n^a	Length (nm)	Width (nm)^b	SA$_{BET}$ (m^2/g)^c	SA$_{TEM}$ (m^2/g)^d
Nanorods	530	80 ± 30^e	7 ± 2	110 ± 7^f	205
Nanorods (^{56}Fe)	100	85 ± 30	5.0 ± 1.3	90	264
Intermediate	240	330 ± 160	14 ± 4	55	92
Microrods	285	670 ± 370	25 ± 9	40 ± 3	52

a Number of unaggregated particles examined by TEM

b Corresponds to the width of the 110 facet according to the convention of Anshutz and Penn (2005)

c Specific surface area determined from seven-point N2-BET measurements

d Specific surface area calculated assuming a rod geometry of a rhomboidal prism as in Anshutz and Penn (2005)

e Uncertainties on particle dimensions represent one standard deviation

f When present, uncertainties on BET surface areas represent one standard deviation of triplicate measurements
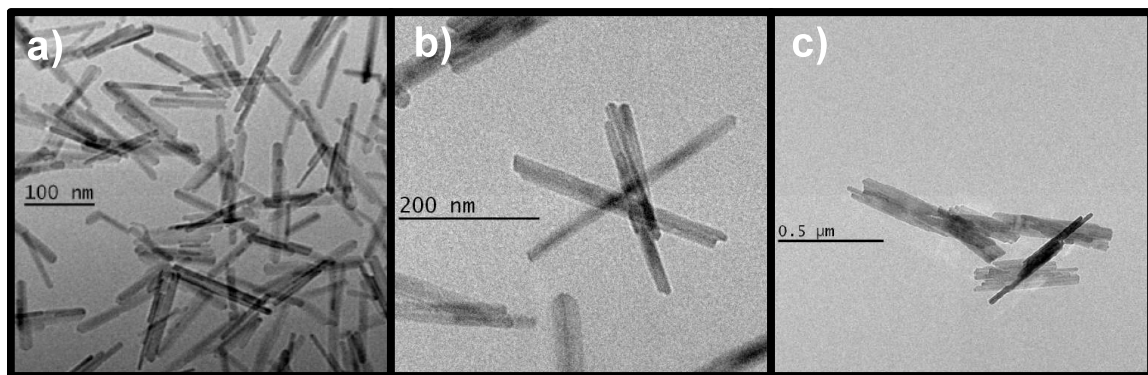
Figure A.1. TEM images of the three goethite primary particle sizes synthesized in the current study. Shown are goethite (a) nanorods, (b) intermediate rods and (c) microrods. The dimensions and surface area of these materials are summarized in Table 1.
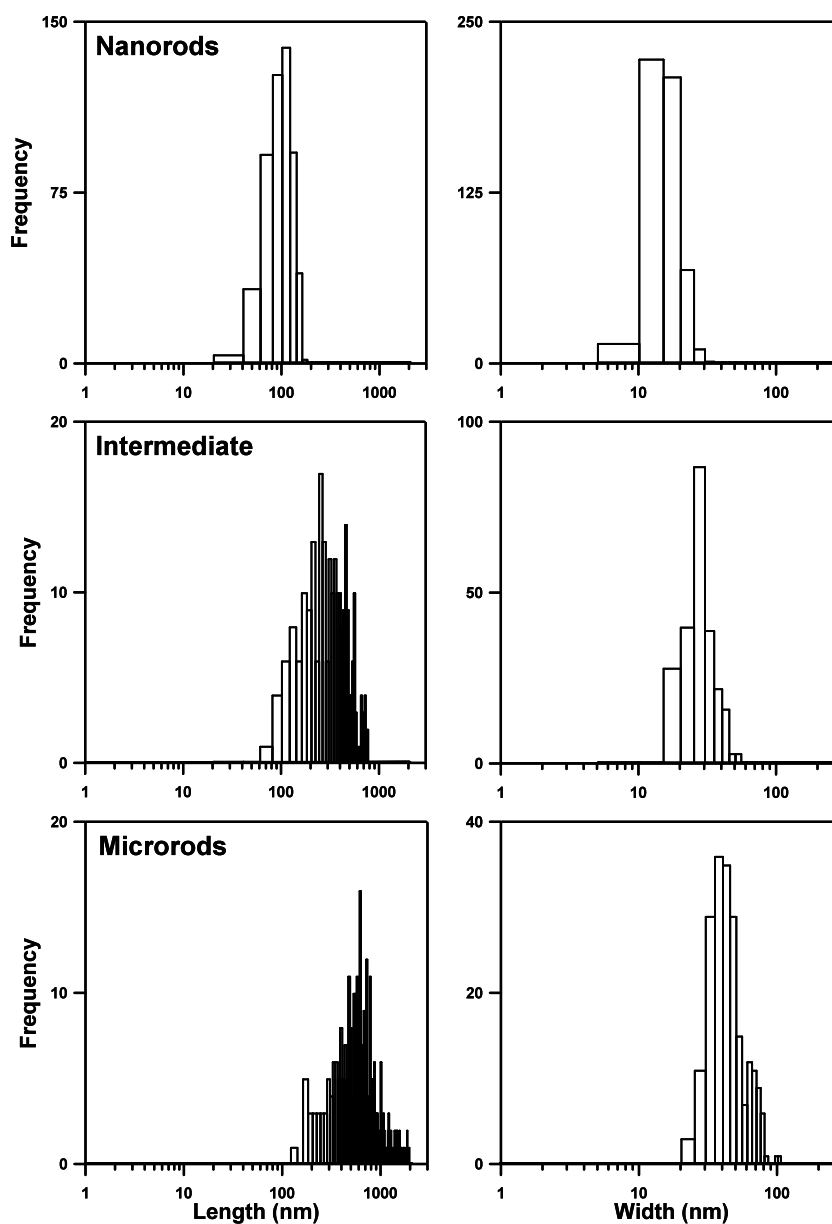
Figure A.2. Size distributions for nanorods, intermediate rods and microrods determined from TEM analysis of unaggregated goethite primary particles. Values are shown on a logarithmic scale with equivalent bin sizes so that the distributions of each primary particle size can be directly compared.
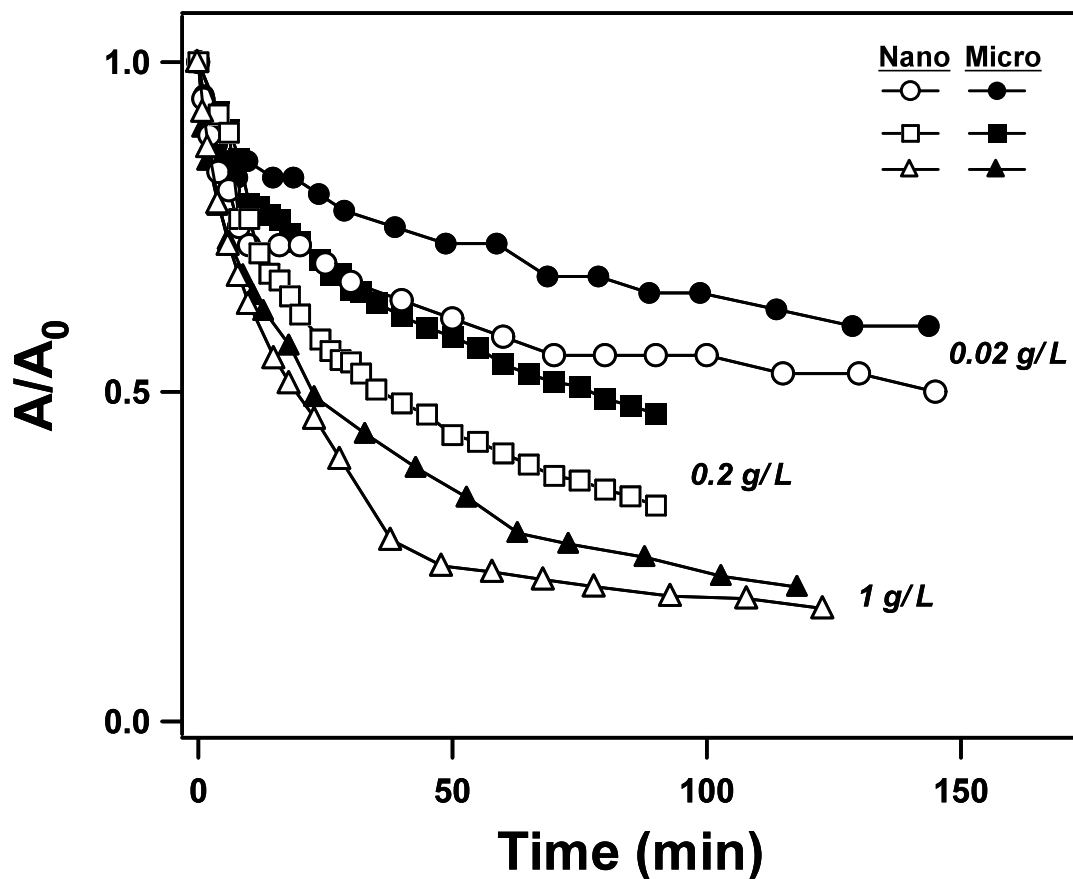
Figure A.3. Sedimentation plots for nanorods and microrods shown as a function of mass loading at pH 7.5. Particles were suspended in 25 mM HEPES buffer with 25 mM KBr, conditions to equivalent to those used in Fe(II) sorption studies. Normalized absorbance values correspond to the amount of light (λ = 510 nm) transmitted through a 1 cm path length cell containing goethite suspensions.
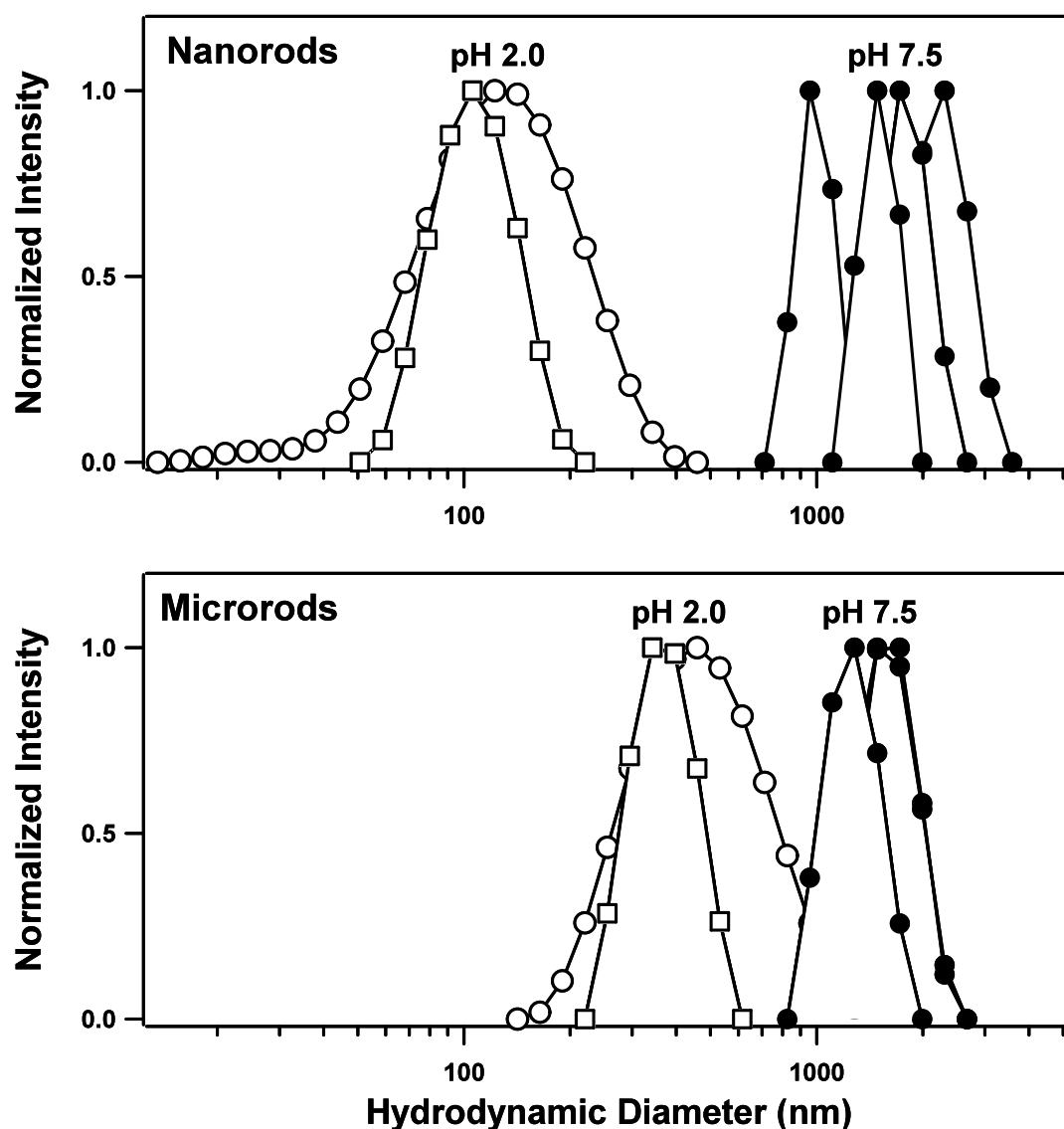
Figure A.4. Intensity-weighted size distributions for nanorod and microrod suspensions determined from dynamic light scattering. Data at pH 2.0 (0.01 N HCl) represent size distributions for 0.01 (open squares) and 0.2 g/L (open circles) suspensions, whereas data at pH 7.5 (25 mM HEPES) are replicate measurements performed on a single 0.2 g/L suspension of each material. The ionic strength of all systems was adjusted to 25 mM with KBr.
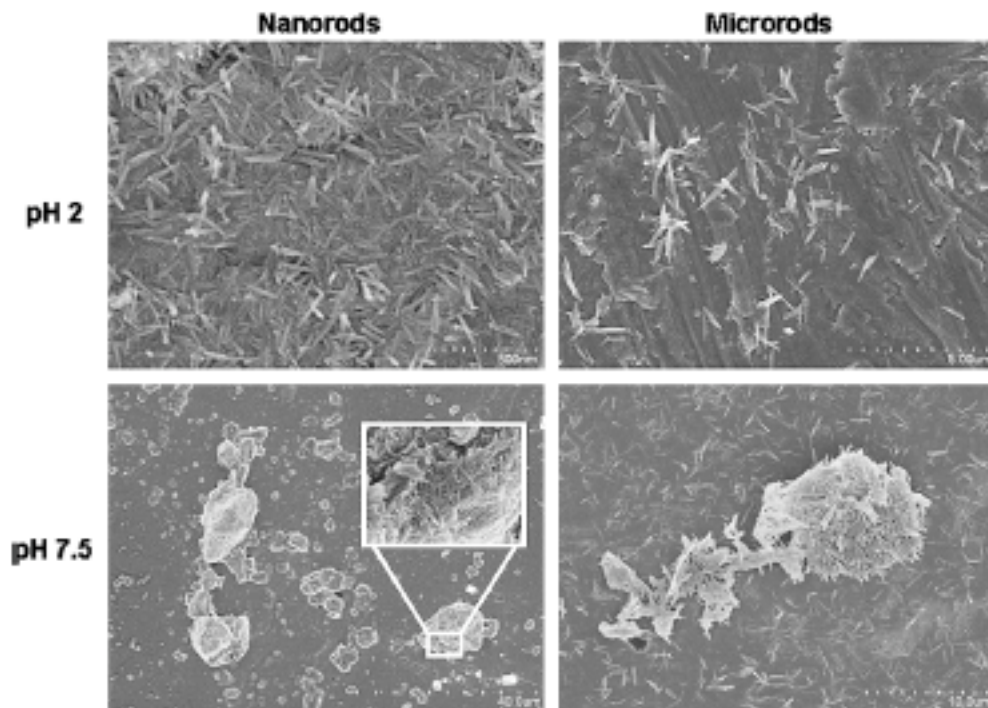
Figure A.5. SEM images of nanorod and microrod suspensions at pH 2 and pH 7.5. Inset for nanorods at pH 7.5 reveals the dense nature of aggregates in these suspensions.
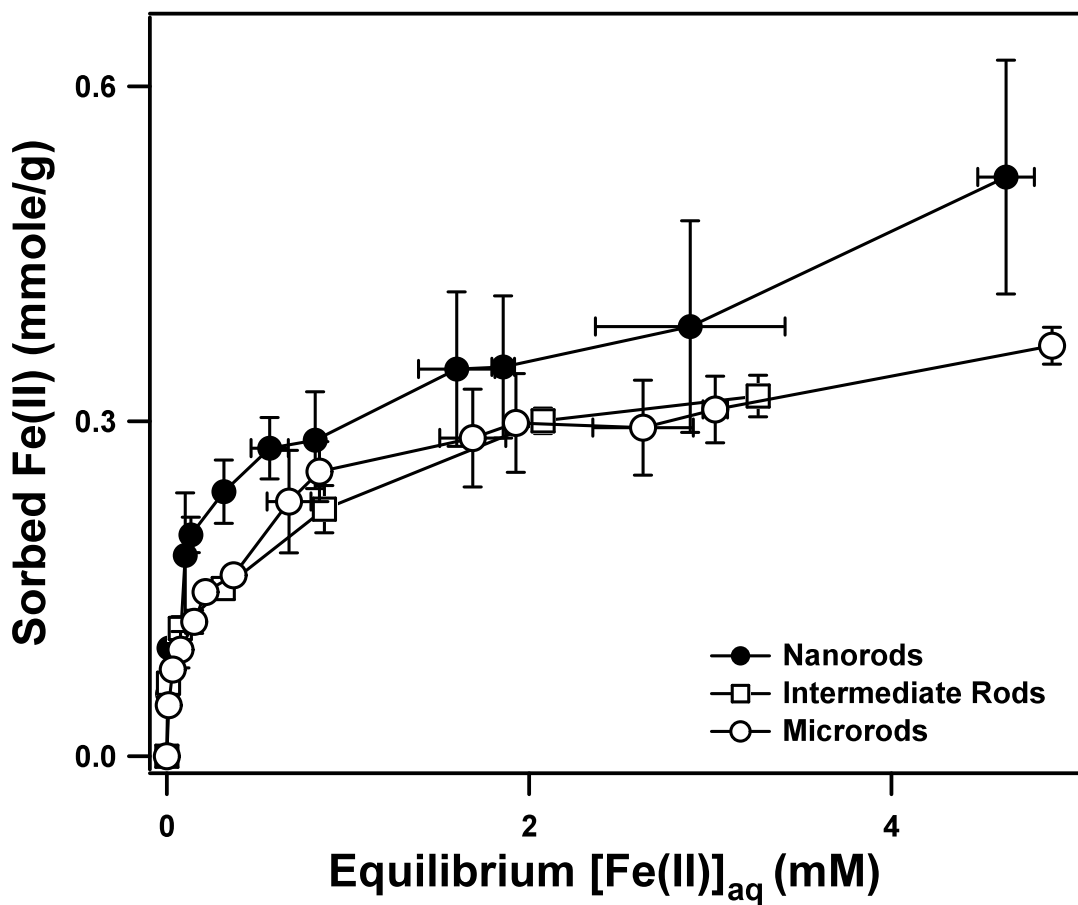
Figure A.6. Fe(II) sorption isotherms for goethite suspensions of different particle sizes. Isotherms were conducted at pH 7.5 in 25 mM HEPES buffer with 25 mM KBr, using either 1 or 2 g/L goethite (15 or 30 mg into 15 mL). Uncertainties represent one standard deviation determined from replicate experiments, where n ranged between 3 and 21.
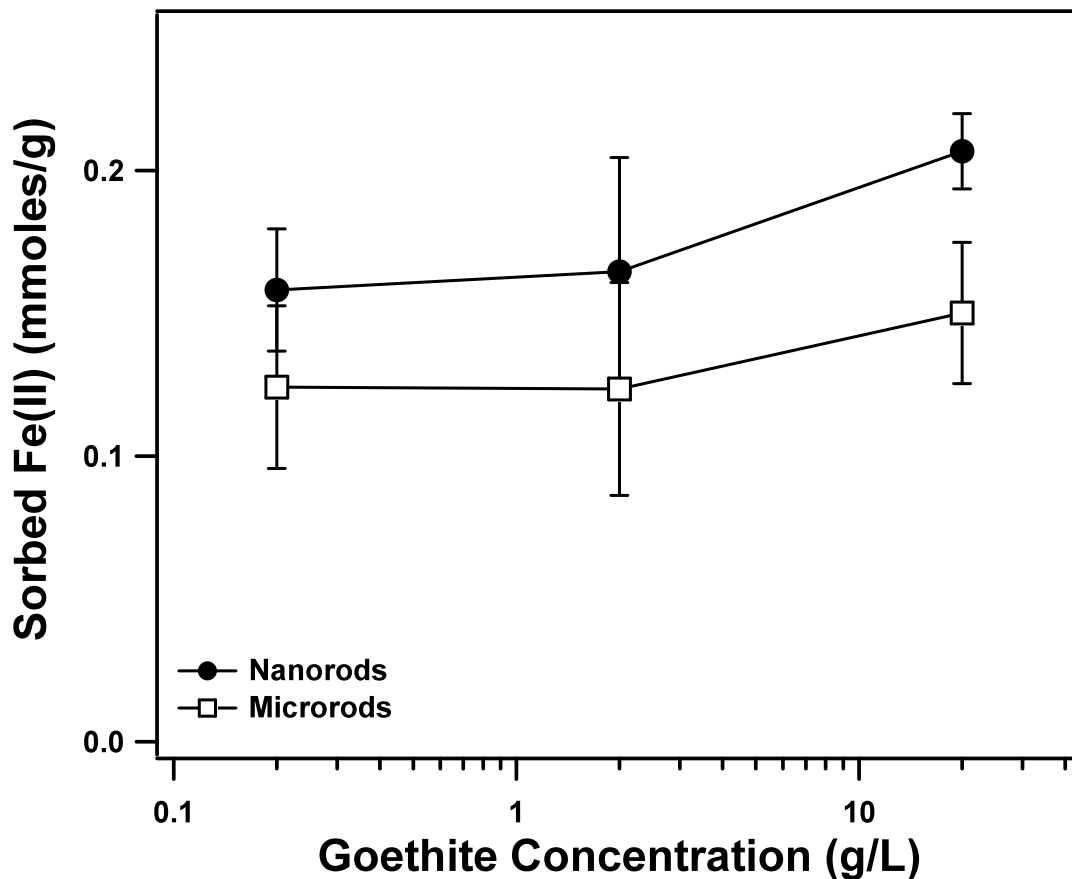
Figure A.7. Concentration of sorbed Fe(II) as a function of goethite solids loading for nanorod and microrod suspensions at pH 7.5 (25 mM HEPES with 25 mM KBr). For each goethite concentration, experimental systems contained an initial ratio of 0.25 mmoles of Fe(II)(aq) per gram of goethite. Uncertainties represent one standard deviation determined from replicate experiments ($n = 6$).
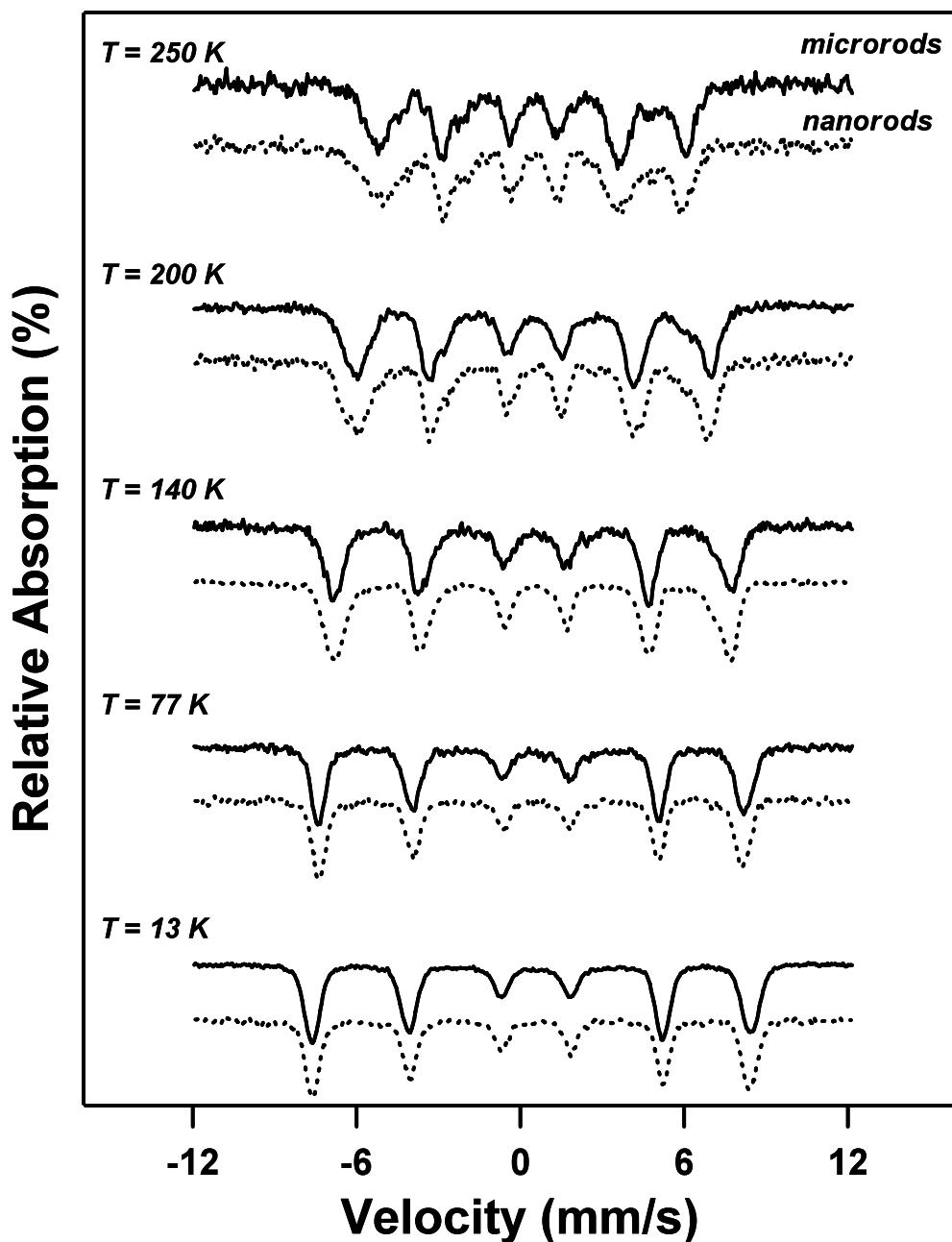
Figure A.8. Temperature profiles of Mössbauer spectra for the reaction of aqueous phase [57]Fe(II) with isotopically enriched [56]Fe goethite nanorods (dashed lines) and microrods (solid lines). Reactions used an initial concentration of 25 mM [57]Fe(II) and 2 g/L goethite (30 mg into 15 mL) and were conducted at pH 7.5 (25 mM HEPES with 25 mM KBr). These conditions resulted in an equivalent concentration of sorbed [57]Fe (0.11 mmoles/g) in both nanorod and microrod suspensions.
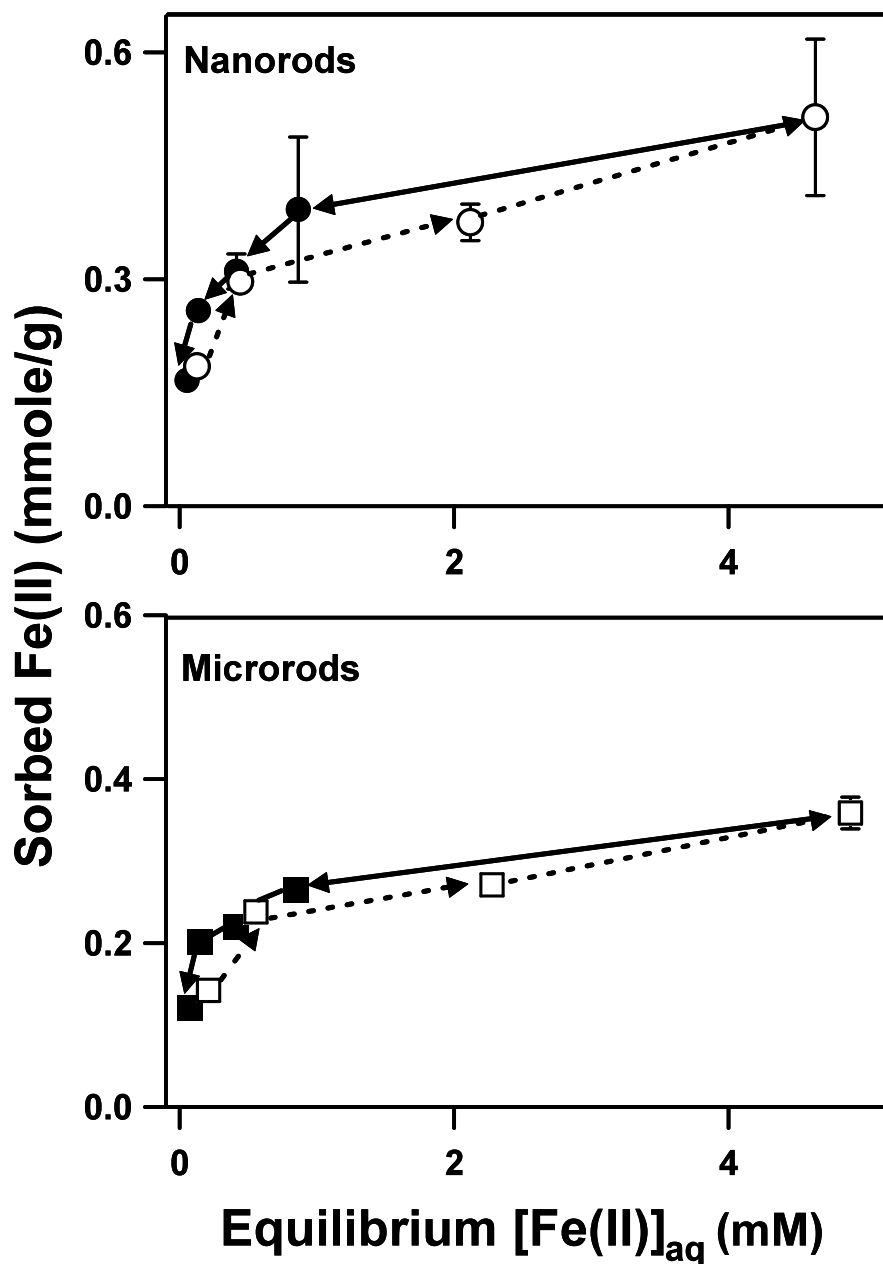
Figure A.9. Results of Fe(II) recovery experiments. Open symbols correspond to the initial sorbed and aqueous Fe(II) concentrations in our experimental systems, whereas solid symbols represent the sorbed and aqueous Fe(II) concentrations after resuspension of the reacted goethite particles in more dilute Fe(II) solutions. Reactors contained 25 mM HEPES with 25 mM KBr at pH 7.5 and 2 g/L goethite (30 mg into 15 mL). Uncertainties represent one standard deviation determined from replicate experiments (n = 3).
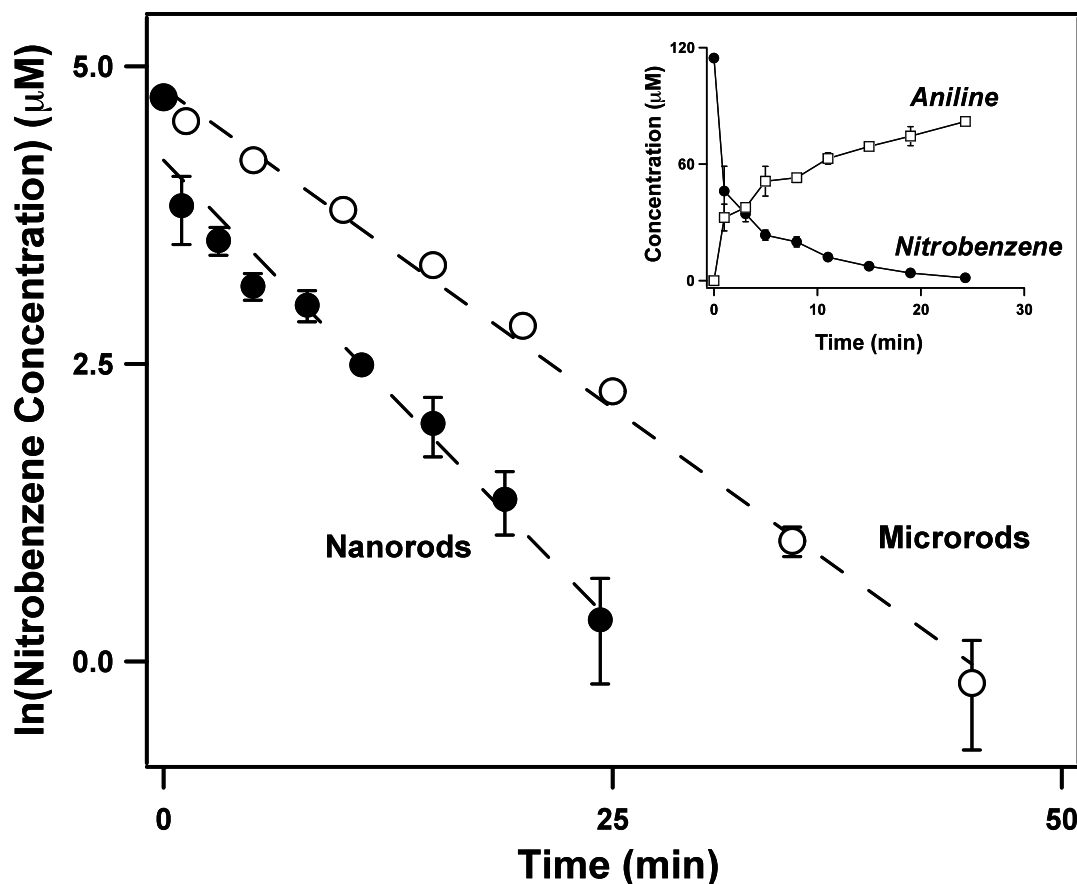
Figure A.10. First-order plot of nitrobenzene concentration as a function of time in nanorod and microrod suspensions. Reactions were conducted at pH 7.5 (25 mM HEPES with 25 mM KBr) and contained an initial nitrobenzene concentration of approximately 100 μM, an initial aqueous Fe(II) concentration of 1 mM and 0.25 g/L goethite. Uncertainties represent one standard deviation determined from triplicate experiments. Dashed lines represent linear regression fits to the experimental data, from which k_{obs} values for nitrobenzene reduction were determined. The inset shows the concentration data as a function of time for nitrobenzene and aniline, the final product, in nanorod suspensions.
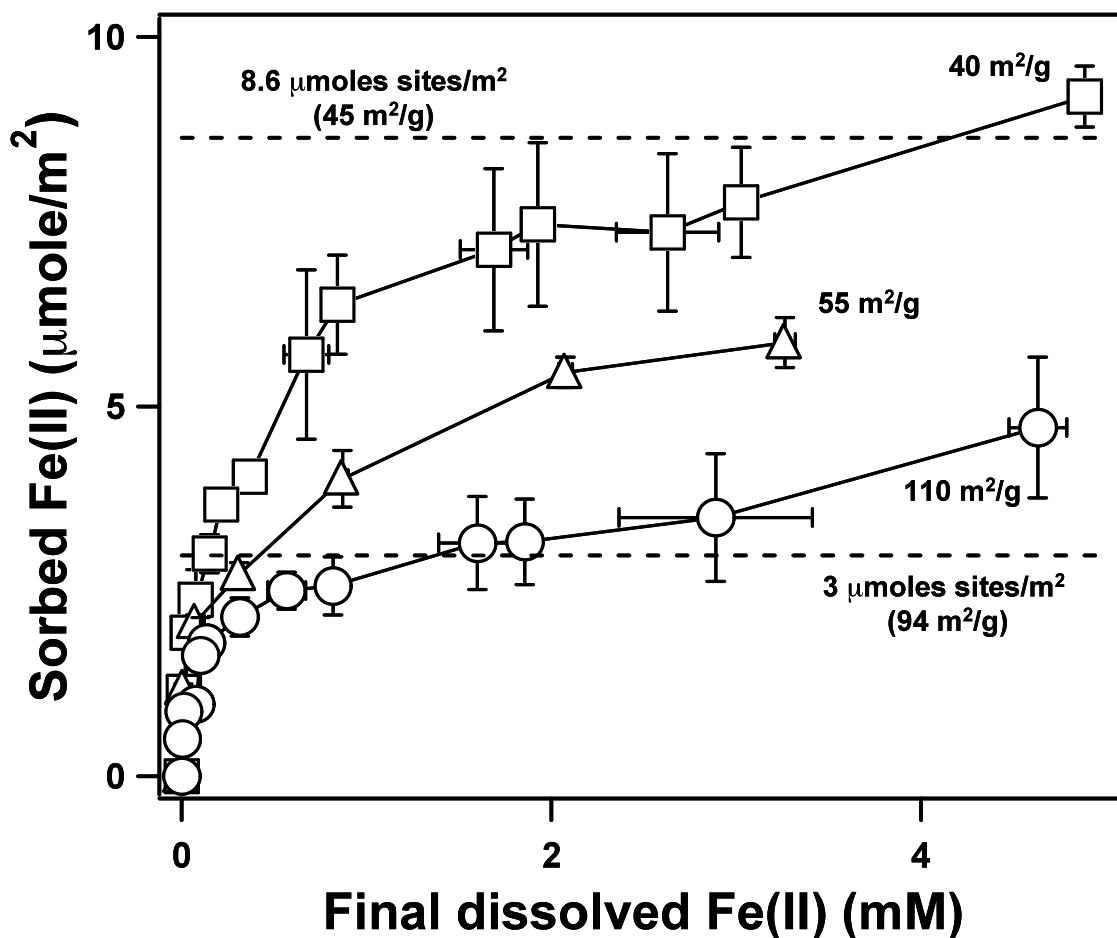
Figure A.11. Isotherms in which sorbed Fe(II) concentrations are reported with units of μmole per square meter of goethite. Values were calculated using the sorption data in Figure 5 and measurements of N_2-BET specific surface area for each material. Dashed lines represent one monolayer of Fe(II) coverage estimated from surface site densities reported by Villalobos et al. [123], which were determined from proton and carbonate sorption studies performed with comparable sizes of synthetic goethite particles. The specific surface areas of the goethite particles investigated by Villalobos et al. (2003) are provided for comparison.
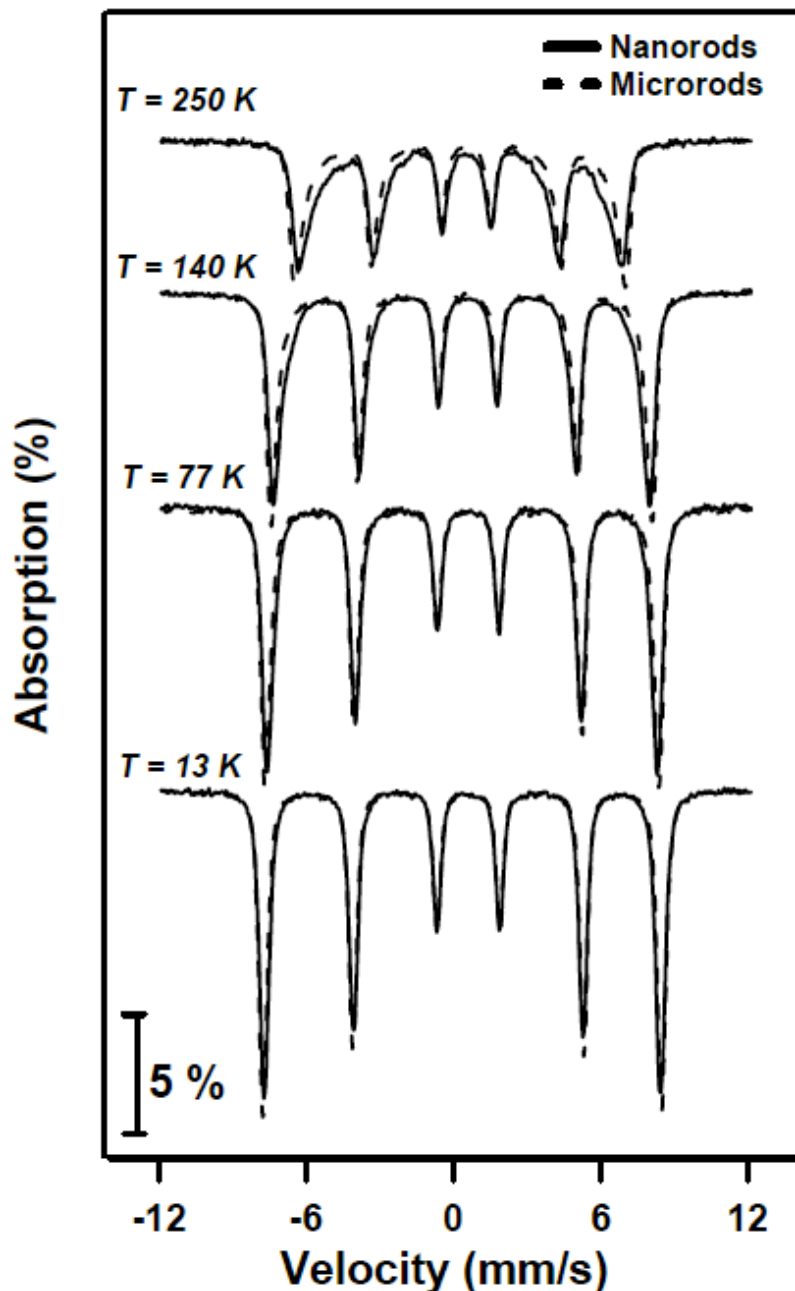
Figure A.12. Mössbauer spectroscopy temperature profiles for goethite nanorods and microrods synthesized from naturally abundant iron starting materials. Mössbauer spectra collected at 298, 250, and 140 K reveal less magnetic ordering in nanorods relative to microrods. Differences in magnetic ordering observed from Mössbauer characterization of these particles were subtle, however, and by 77 K, both the nanorods and microrods had achieved full magnetic ordering.
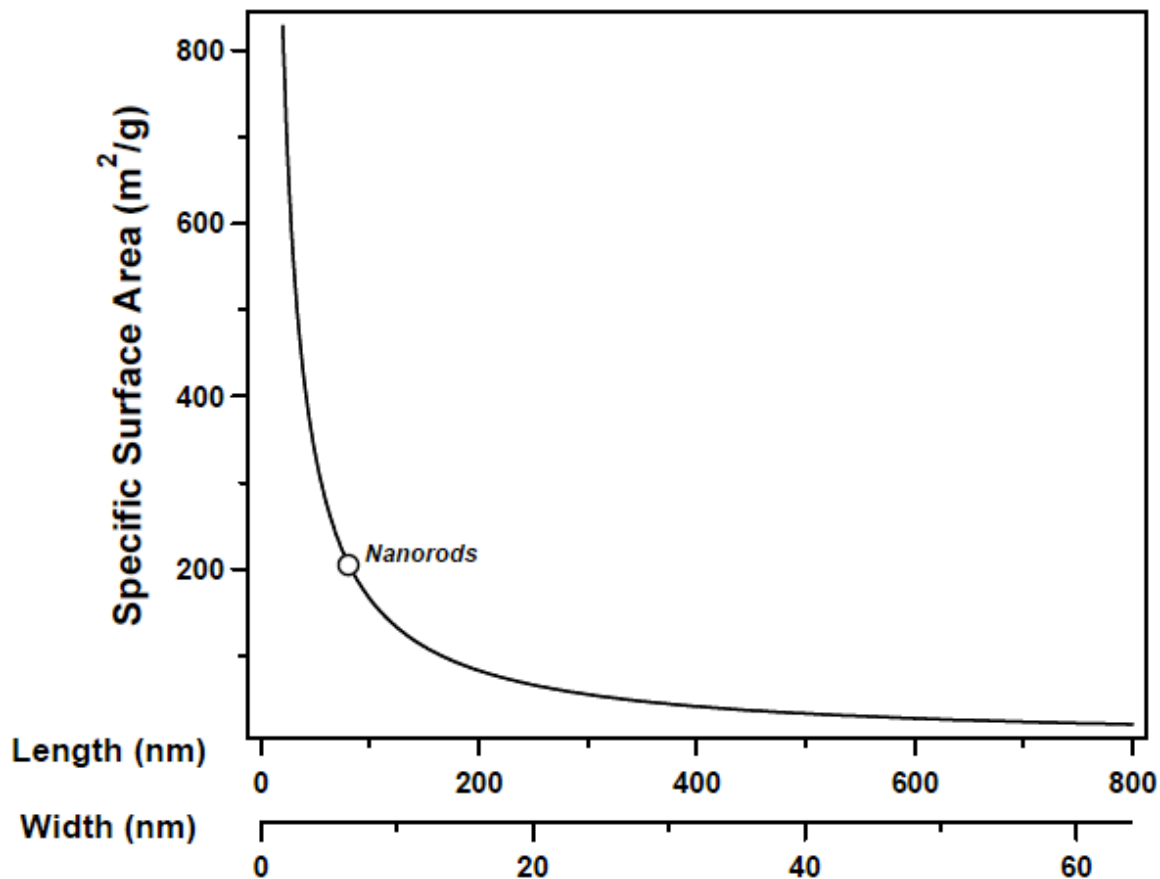
Figure A.13. Relationship between goethite dimensions and specific surface area calculated by modeling the geometry of a goethite particle as a rhomboidal prism. Calculations assumed a goethite density of 4.26 g/cm^3 and a particle aspect ratio (length:width) of 12.3, which is equal to that determined for nanorods via TEM particle size analysis. The dimensions and specific surface area of the nanorods investigated in the current study are noted. The dimensions and surface area of intermediate rods and microrods are not shown, as they exhibited a different aspect ratio (~25) relative to nanorods.
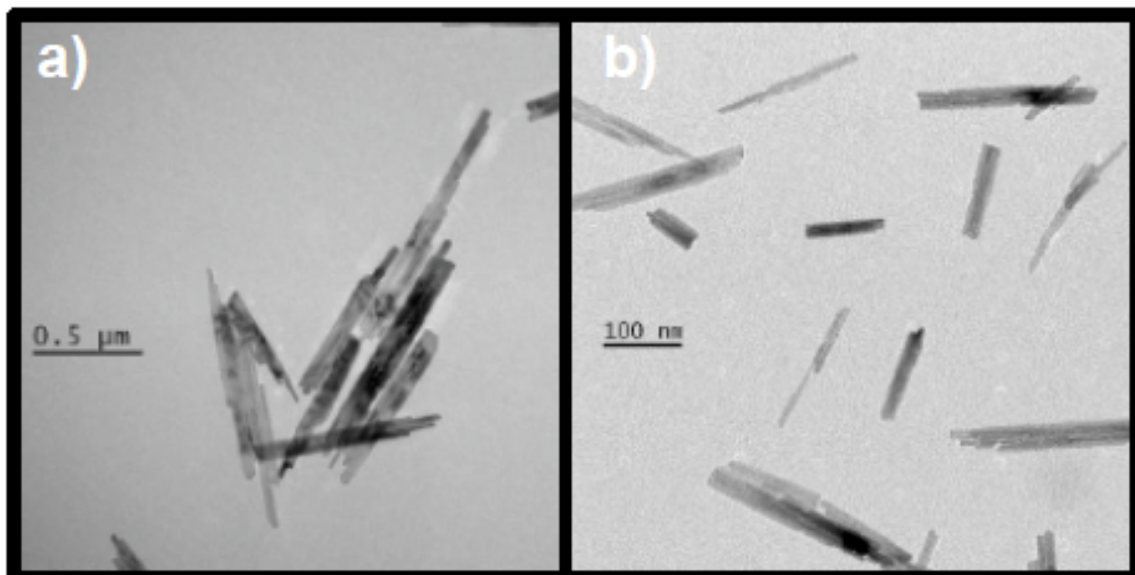
Figure A.14. Representative TEM images of (a) ^{56}Fe microrods and (b) ^{56}Fe nanorods. Nanorods exhibited a tendency to adhere to one another.
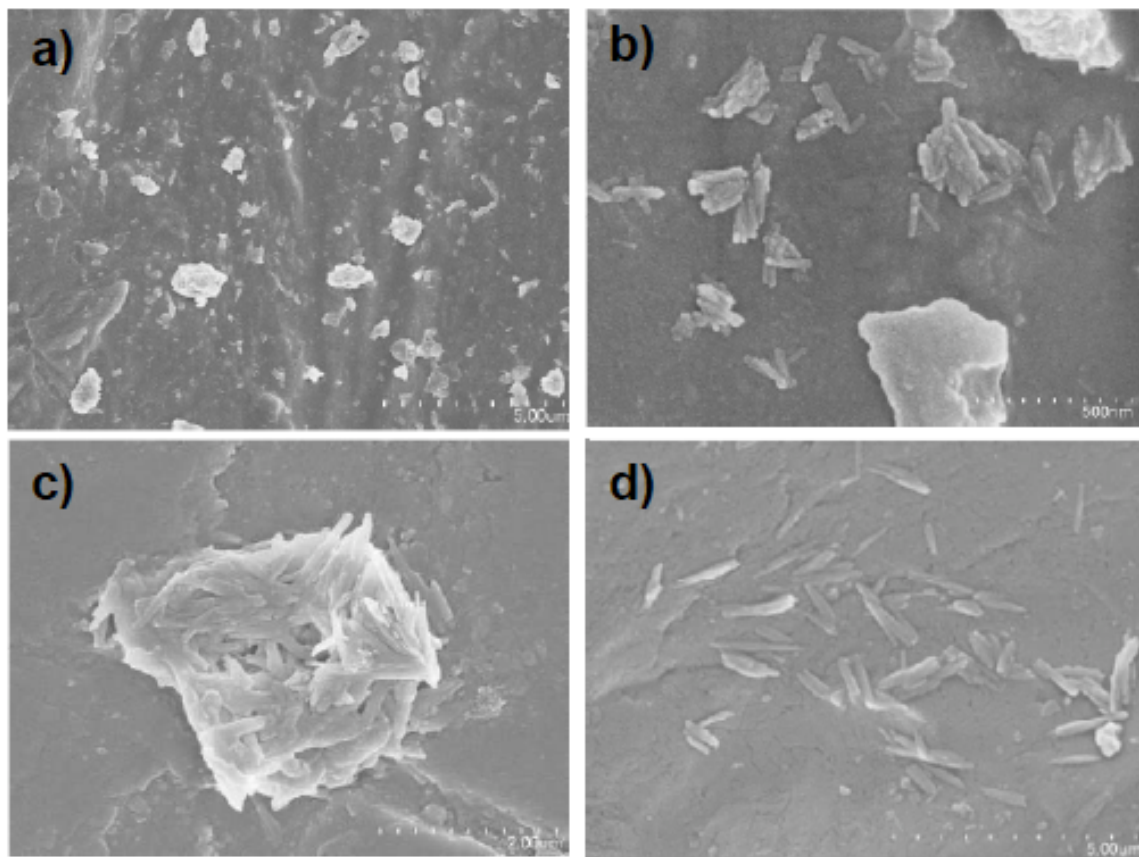
Figure A.15. SEM images collected of nanorod (a and b) and microrod (c and d) suspensions at pH 7.5 after 30 minutes of settling time.
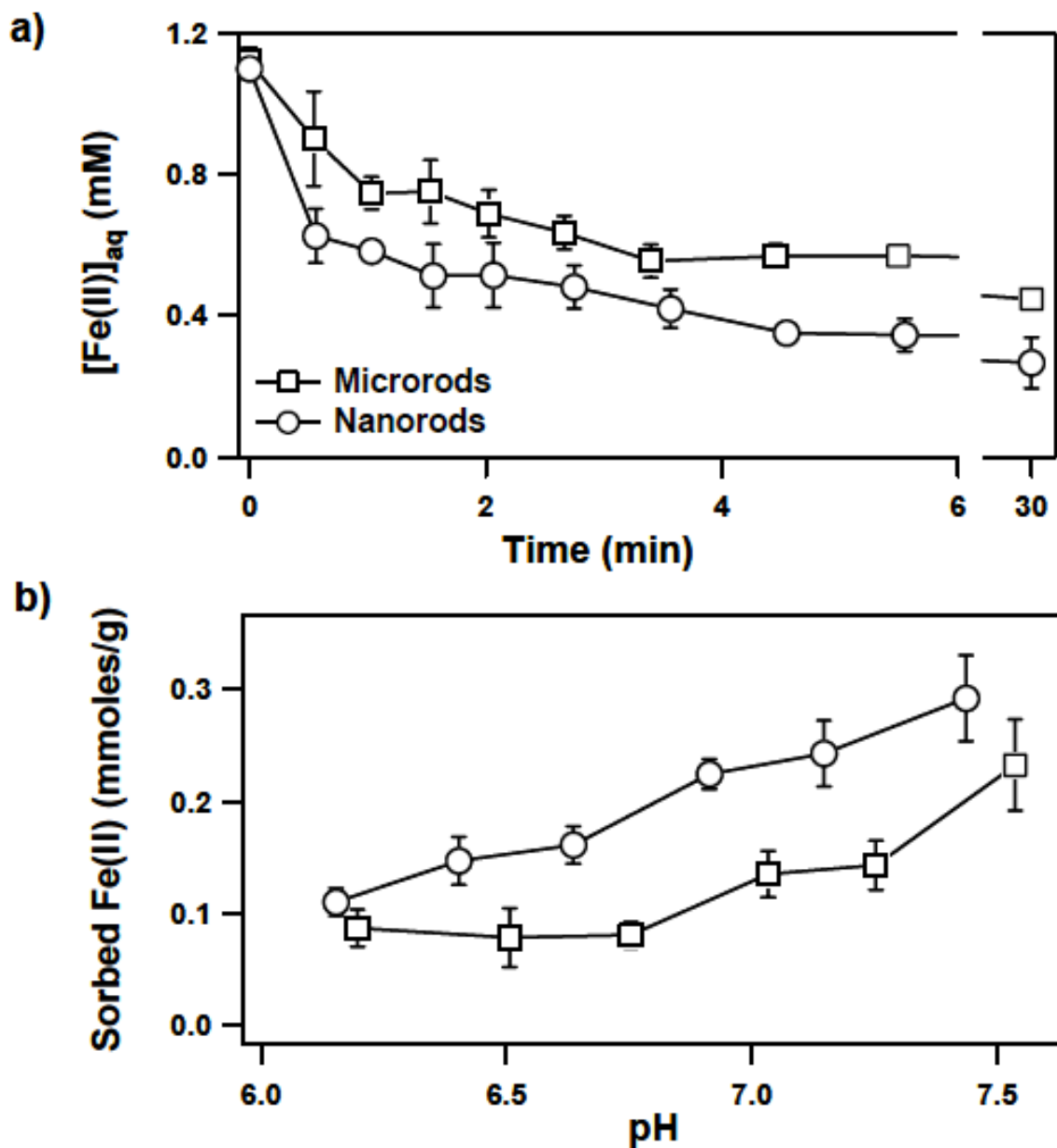
Figure A.16. Results of batch studies examining (a) the rate and (b) the pH-edge behavior for Fe(II) sorption on goethite. Rate experiments were conducted at pH 7.5 in 25 mM HEPES buffer with 25 mM KBr, using 4 g/L goethite (60 mg into 15 mL) and an initial aqueous Fe(II) concentration of 1 mM. Reactors were slowly mixed end-over-end at 9 rpm. pH-edge experiments were conducted in 25 mM PIPES buffer with 25 mM KBr and an initial aqueous Fe(II) concentration of ~1 mM. Uncertainties represent one standard deviation determined from triplicate experiments.
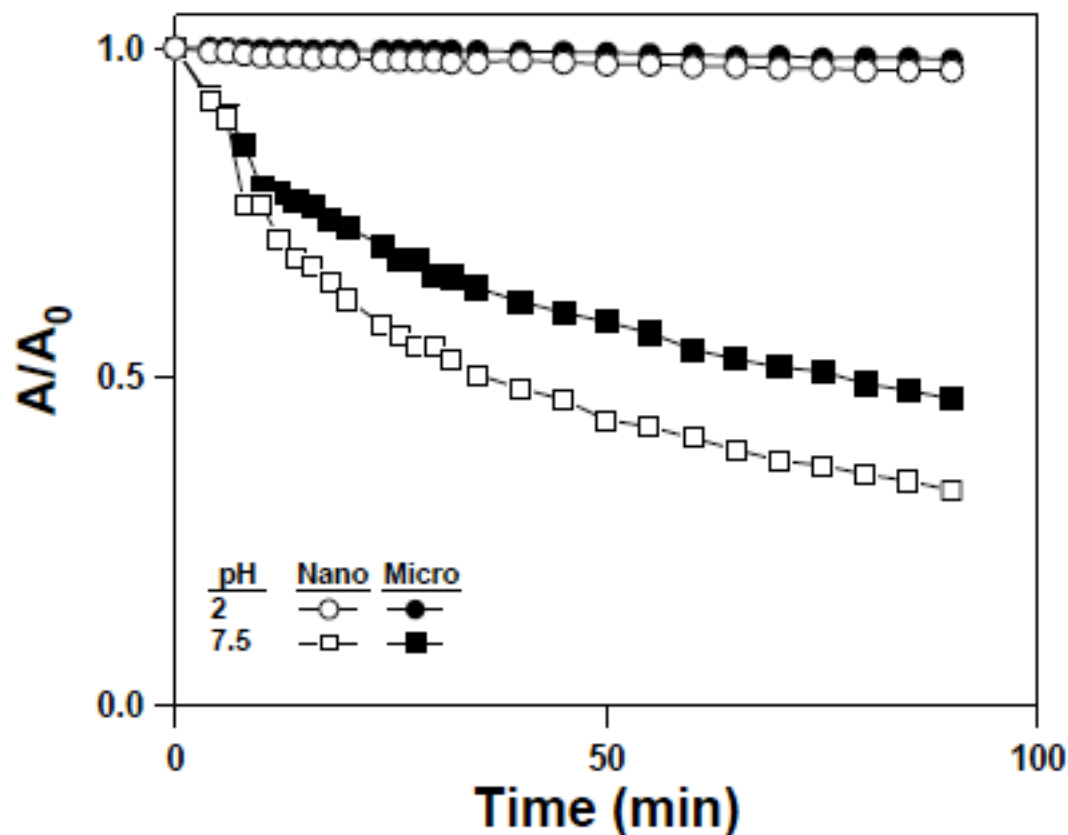
Figure A.17. Sedimentation plots for nanorods and microrods shown as a function of pH for a fixed mass loading of 0.2 g/L. Suspensions were prepared in either 0.1 N HCl (pH 2.0) or 25 mM HEPES (pH 7.5). The ionic strength of all systems was adjusted to 25 mM with KBr. Normalized absorbance values correspond to the amount of light at wavelength 510 nm transmitted through a 1 cm path length cell containing goethite suspensions.

APPENDIX B: EVOLUTION OF MN OXIDE REDOX ACTIVITY AFTER
REACTION WITH AQUEOUS FE(II)

Abstract

Fe and Mn are both common redox-active metals in environmental systems, and Fe-Mn redox chemistry is an important consideration when predicting fate and transport of contaminants. Reactions of aqueous Fe(II) with pyrolusite (β-MnO_2) were assessed using electron microscopy, X-ray diffraction, aqueous Fe and Mn analyses, and ^{57}Fe Mössbauer spectroscopy. Pyrolusite solids were exposed to successive reactions with 3 mM Fe(II) at pH 7.5 in order to assess evolving reactivity of Mn/Fe solids. In addition, we have extended our selective use of Fe isotopes in conjunction with Mössbauer spectroscopy by using enriched ^{56}Fe(II) or ^{57}Fe(II), which were varied in their order of exposure to Mn solids, allowing us to probe marginal Fe(II) reactivity after preliminary Fe(II) oxidation or continuing redox reactions with initial Fe(III) precipitates. Using these complementary techniques, we determined that lepidocrocite was initially the predominant Fe oxidation product of Fe(II), and additional Fe(II) exposures resulting in an increasing proportion of magnetite on the pyrolusite surface. Over a series of nine 3 mM Fe(II) additions, Fe(II) was still always oxidized by Mn/Fe particles, implying that Mn phases can still be important redox active phases after extensive surface coverage with Fe(III) oxides. Initial Fe(III) oxide precipitates were also further reduced by additional Fe(II), and additional Mn was released into solution as additional Fe(II) was oxidized, indicating that Fe and Mn chemistry is influenced by subsequent reactions of Mn/Fe oxides.

Introduction

Iron (Fe) and manganese (Mn) are the two most common redox-active elements in the Earth's crust [126]. Reactions between Fe and Mn species, as well as with other

common groundwater constituents have significant impacts on mineral formation and dissolution [127], trace metal sequestration [128], and contaminant transformations [129, 130]. The present study focuses on redox reactions of ferrous iron (Fe(II)) with oxidized Mn(IV) solids. Thermodynamic considerations would predict that in the presence of Fe(II), all manganese species would exist as reduced manganese Mn(II) as opposed to oxidized Mn (IV). Complex environmental systems, however, do not always adhere to the compositions implied by thermodynamic constraints. Microorganisms have been shown to significantly impact the speciation of Fe and Mn between reduced and oxidized forms. [e.g., 131, 132]. Bacterial action can result in large local concentrations of dissolved Fe(II) or Mn(IV) solids that form and persist in transient but important time scales.

Certain geochemical conditions (low pH, anaerobic zones, presence of organic matter) can stabilize aqueous Fe(II), allowing reduced Fe to travel significant distances and interact with a variety of mineral species. Examples of scenarios where geochemical and kinetic effects dictate the redox interactions observed in field settings are widespread. Studies of both freshwater and marine porewater constituents have observed dissolved Fe(II) in the presence of Mn oxides [133] and implicated Mn oxides as the relevant oxidants of Fe(II) in porewaters [134]. Interactions between Fe(II) and Mn oxides has been studied previously under several model geochemical settings, including acid mine drainage [135-137] and marine systems [134]. Reaction of Fe(II) with Mn(IV) oxides has previously been described by the reaction:

$$2Fe^{2+} + MnO_2 + 2H_2O \rightarrow 2FeOOH + Mn^{2+} + 2H^+ \qquad (1)$$
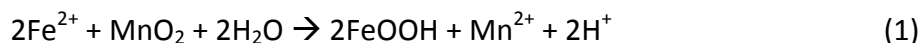
in order to explain locally high concentrations of manganese oxides in sediments [138]. Redox reactions of Fe(II) with Mn(IV) oxides would also result in an oxidized Fe species, which often occurs as a surface coating on the underlying Mn oxide substrate.

Composition of resulting Fe oxides has previously been difficult to ascertain with traditional methods of solid-phase analysis such as x-ray diffraction (XRD) or electron microscopy. Postma (1985) was unable to clearly define the Fe oxide coating that occurred on birnessite (δ-MnO$_2$) particles reacted with Fe(II), and in later studies chose to model the resulting Fe(III) oxide phase as an amorphous Fe(OH)$_3$ species [139]. Krishnamurti and co-workers used a combination of infrared spectroscopy, XRD, and transmission electron microscopy (TEM) to determine that Fe(II) in contact with different Mn oxide substrates (e.g., cryptomelane, hausmannite, and pyrolusite) will react to form different Fe oxide layers, depending on experimental solution conditions [140].

Formation of an Fe(III) surface coating on Mn oxide solids may impact the rate or overall ability of Mn oxides to remain redox-active phases in environmental systems. In simulated acid-mine drainage systems, Mn(II) production from Mn oxides reacted with Fe(II) decreases with time, suggesting that evolution of a new Fe oxide surface interferes with the ability of underlying Mn oxides to accept electrons from aqueous Fe(II) [136]. Further studies in this experimental system attributed changing rates of Fe(II) loss and Mn(II) production from batch reactors to Langmuir-type blocking of Mn(IV) surface sites by Fe(III) oxide precipitates using a model simulations [137]. In these studies, it was also difficult to concretely ascertain the composition of resulting Fe(III) reaction products. Fe(II)/Mn(IV) redox activity may also negatively impact future oxidation capacity of Mn oxides, which have been demonstrated to be important oxidants for a variety of important environmental remediation processes [141, 142]. Formation of an amorphous Fe(III) precipitate was shown to inhibit Cr(III) oxidation by birnessite at pH 5.5 [143].

In this study we wished to evaluate the effect of aqueous Fe(II) on electron transfer reactions at Mn oxide surfaces. Mn oxide particles were reacted with successive exposures of Fe(II) at pH 7.5. Most investigations involving Fe(II) and Mn oxides have occurred at lower solution pH values between 3-6 in order to simulate acid mine drainage. Evaluation of Fe/Mn redox chemistry at circum-neutral pH values is also

important, as anoxic Fe(II) plumes may persist in neutral pH environments in the presence of Mn oxides [144].

Alongside traditional methods of analysis (XRD, microscopy, chemical Fe and Mn analyses), we utilized ^{57}Fe Mössbauer spectroscopy in conjunction with isotopically enriched ^{57}Fe(II) in order to increase the Fe signal (natural Fe contains roughly 2% ^{57}Fe). To further examine Fe(III) surface precipitate morphology and what effect this phase has on further redox reactions with Fe(II), we exposed Mn oxide particles to a series of solutions buffered at pH 7.5 which contained either ^{57}Fe(II) (Mössbauer-active) or ^{56}Fe(II) (Mössbauer-inactive). In this manner, we could submit Mn oxide solids to a series of Fe(II) exposures, but only a particular "pulse" of Fe(II) would be visible with Mössbauer spectroscopy throughout the experiment. This procedure allowed us to track the chemical changes that occurred to a specific set of Fe atoms, even as more Fe(II) is introduced to the particle surface. Evolving redox capacity of Mn oxides was assessed through measurements of aqueous Mn and X-ray photoelectron spectroscopy.

Materials and Methods

Mn oxide solids characterization

Commercially available MnO_2 (Sigma-Aldrich) was used for the entirety of the present study. Mn oxides were ground with a mortar and pestle before sieving (150-micron mesh) to achieve a uniform particle size. XRD was performed on solids using a Rigaku Miniflex II equipped with a Co X-ray source. Initial characterization with XRD indicated pyrolusite (β-MnO_2) was the sole Mn oxide phase, and no diffraction peaks indicative of impurities could be detected (Figure B.2). Surface area measurements on sieved Mn oxide powders were made with a Quantachrome BET Nova surface area analyzer using a multipoint measurement and consistently resulted in low specific surface areas, ~ 1-2 m^2/g.

Sequential batch experiments with isotopically-enriched aqueous Fe(II)

All reagents were used as received. Experiments were performed in an anaerobic chamber with multiple palladium catalysts to scavenge trace O_2, and all solutions were made with deionized water that had been deoxygenated through N_2 sparging. Aqueous Fe(II) stock solutions were prepared by dissolving enriched [56]Fe or [57]Fe metal (Chemgas, 99% and 96%, respectively) in 0.5 M HCl. To initiate Fe(II) redox experiments, 18 mL of a pH 7.5 buffer solution (25 mM 4-(2-hydroxyethyl)-1-piperazineethanesulfonic acid (HEPES) + 25 mM KBr) was spiked with either a [57]Fe or [56]Fe stock solution to yield an initial aqueous Fe concentration of roughly 3 mM. Prior to Fe addition, reactors were counter-spiked with 0.5 M NaOH to maintain initial pH. Reactors were equilibrated for 1 hr before filtering through a 0.2-micron syringe filter to remove any potential Fe precipitates. Initial Fe(II) concentration was measured, and 18 mg of Mn oxide powder was added to initiate the timecourse (solids loading 1 g/L, Fe/Mn molar ratio 0.26). Reactors were placed on an end-over-end rotator and mixed in the dark. Periodically, small aliquots (~150 uL) of solution were withdrawn, filtered with 0.2-micron nylon syringe filters, and used for chemical Fe and Mn analyses. Fe(II) redox experiments were typically allowed to run for ~ 90 min. If solids for a particular experiment were scheduled to receive more than 1 treatment in an aqueous solution, experimental reactors were allowed to stand for a short amount of time to allow dense Mn solids to settle, where they could be easily removed with a pipette. Solids were placed in a microcentrifuge tube and centrifuged to pellet solids and facilitate easy removal of the residual aqueous supernatant. Mn solids were then resuspended in a new buffer solution containing 3 mM [57]Fe(II), [56]Fe(II), or no Fe, depending on the particular experiment, and a new timecourse was performed to investigate the movement of aqueous Fe and Mn into or out of solution. Solids resuspension in new buffer solutions with or without additional aqueous Fe(II) was repeated anywhere from 1-9 times.

Acid Extractions

In an attempt to reconcile the amount of Fe(II) lost from solution with the production of Mn(II) into solution, acid extractions were performed on recovered solids to remove surface precipitates of Fe and any adsorbed Fe or Mn species. Control reactors with an identical buffer system, Mn solids loading, and Fe/Mn ratio were mixed for 90 min before solids were collected and resuspended in deionized water. Varying amounts of 5 M HCl were added to different reactors to obtain a distribution of pH values between ~ 1- 2. Extraction reactors were allowed to mix for ~ 150-300 hours, periodically removing samples for Fe and Mn analyses.

Chemical Analyses

Aqueous Fe(II) was measured colorimetrically using 1,10-phenanthroline at 510 nm [145]. Fluoride was used to remove interferences from aqueous Fe(III) when present in samples [146]. The amount of Fe(III) in solution was determined by the difference of measured Fe(II) content and the Fe concentration of a sample that had been completely reduced from the addition of hydroxylamine HCl. Aqueous Mn was determined by modifying the formaldoxime method outlined in Morgan and Stumm [147] and Abel [148], using phenanthroline to complex interfering aqueous Fe.

Post-reaction solids characterization

After the final timecourse in the presence or absence of aqueous Fe(II), solids were captured by filtration through a syringe filter with a removable 0.45-micron filter disc. A small portion of recovered solids (~ 1 mg) were removed from the filter disc and rinsed with deionized water to remove residual aqueous Fe, Mn, and buffer salts. Rinsed solids were placed on an aluminum microscopy stub and fixed with carbon tape. Imaging of resulting particles and surface precipitates was performed with a Hitachi S-4800 scanning electron microscope. Remaining Mn/Fe solids recovered after sequential reaction experiments were wrapped in Kapton oxygen-impermeable tape prior to analysis with ^{57}Fe Mössbauer spectroscopy. Mössbauer spectra were collected in transmission mode using a ^{57}Co source and a Janis cryostat with temperature control to

13 K. Mössbauer spectra collected at room temp, 140 K, 77 K, and 13 K, and data was calibrated against α-Fe foil spectra collected at room temperature, Spectral fitting was performed with the Recoil Software package (http://www.isapps.ca/recoil/)

Oxidation states of Mn and Fe atoms near the surface of reacted Mn/Fe particles were characterized with x-ray photoelectron spectroscopy (XPS) using a Kratos Axis Ultra XPS system. Activated carbon was used as an internal reference standard in all samples. Mn oxidation states were assessed by comparing the difference in binding energies of the Mn $2p^{3/2}$ and O 1s peaks, a method successfully utilized to characterize oxidation of different transition metals [149, 150]. Mn $2p^{3/2}$ – O *1s* differences were determined for unreacted MnO_2 starting material and compared to samples that had been reacted with 1 and 2 suspensions of aqueous Fe(II) in the manner described above.

<u>Results and Discussion</u>

Formation of Fe(III) precipitate

Oxidation of aqueous Fe(II) by pyrolusite stimulated a rapid and pronounced change in observed particle morphology. After exposure to aqueous Fe(II), the normally featureless pyrolusite surface was completely transformed into a dense network of needlelike protrusions and fused platelets, likely due to formation of an Fe(III)-containing precipitate (Figure B.1). Individual needles ranged in length from ~ 200 – 800 nm. Many Fe(III) oxides exist as rod-like structures, including goethite, lepidocrocite, and akaganeite, and schwertmannite [151].

Powder X-ray diffraction (XRD) patterns collected after pyrolusite solids were reacted with 3 mM Fe(II) at pH 7.5 reveal the presence of lepidocrocite (γ-FeOOH) in the solid phase, which is consistent with needle-like precipitate morphology observed in SEM images (Figure B.1). No other Fe phases could be detected, indicating that lepidocrocite is the dominant phase formed during Fe(II) oxidation by pyrolusite at pH 7.5. Synthetic lepidocrocite is commonly formed through rapid Fe(II) oxidation in air at near-neutral pH values [151], conditions which are analogous to our experimental work

through heterogeneous redox reactions with Mn oxides, promoting rapid anaerobic oxidation of Fe(II) with pyrolusite.

Mössbauer spectra of the precipitate formed after the initial reaction of pyrolusite with aqueous ^{57}Fe(II) reveal several interesting characteristics. At room temperature (298 K), the Fe precipitate has doublet spectral parameters indicative of a ferric solid (center shift = 0.37 mm/s, quadrupole splitting = 0.53 mm/s). Absence of ferrous doublet character (with a larger center shifts and quadrupole splitting) in Mössbauer spectra indicates that all solid-associated Fe was oxidized to Fe(III) (Figure B.3). Room-temperature Mössbauer parameters can not conclusively indicate the presence of lepidocrocite, as similar ferric doublets occur for multiple Fe oxides. At lower collection temperatures, spectral doublet features are replaced by a sextet as magnetic ordering occurs in the sample. Between 77 K and 13 K, the Fe phase is ordered into a sextet, characteristic of lepidocrocite or ferrihydrite [114]. Mössbauer spectra collected at 13 K indicate that the initially observed doublet has not resolved into a fully ordered sextet, an uncommon observation for a majority of Fe(III) oxides. Lepidocrocite has an average ordering temperature of ~ 70 K [114]. Potential explanations for decreased ordering temperature in Fe oxides include decreasing crystallite size and cation substitution into the solid structure. Although Mn incorporation has not previously been observed in lepidocrocite, estimates of ionic radii for Mn(II) or Mn(III) cations are similar to those expected for Fe(III) in oxides.

Formation of an Fe precipitate was supported by rapid loss of Fe(II) from the aqueous phase upon introduction to pyrolusite (Figure B.4). According to equation 1, loss of Fe(II) should be accompanied by formation of aqueous Mn(II), although reaction stoichiometry in equation 1 predicts production of half as much Mn(II) produced as Fe(II) consumed. Although our colorimetric method does not permit speciation of Mn, it is reasonable to assume that aqueous Mn is most likely Mn(II) based on solubility constraints [147]. Aqueous Mn is produced as Fe(II) is consumed, but yields of Mn do not reach levels predicted by equation 1. Average recoveries, calculated as:

$$\text{Recovery (\%)} = \frac{100 \times 2 \times [Mn\,produced]}{[Fe(II)\,lost]} \qquad (2)$$

are typically 40% in our experimental procedure for 3 mM Fe(II) reacted with 1 g/L pyrolusite. Non-stoichiometric production of aqueous Mn has previously been attributed to adsorption or entrainment of newly-produced Mn(II) in mineral surfaces [e.g., 138, 152].

Acid extraction of Mn/Fe particles after reaction with aqueous Fe(II) was successful at recovering additional Mn as Fe(III) solids were dissolved. Compilation of Fe(III) recoveries and aqueous Mn recoveries for acid extractions in pH 1- 2 solutions at times ranging from 12-300 hours indicate relatively congruent dissolution of Mn and Fe(III), suggesting that Mn was evenly distributed throughout the Fe precipitate phase (Figure B.5 and Table B.1). Even distribution of Mn within Fe precipitates could be evidence for cation substitution of Mn into lepidocrocite, explaining the anomalously low ordering temperature observed in [57]Fe Mössbauer spectra. Contrary to expectations, we observed Mn recovery that more closely resembled a 1:1 ratio (solid line, Figure B.5) with dissolved Fe(III) than a 1:2 ratio predicted by equation 1 (dashed line, Figure B.5.) Although we cannot be certain due to our inability to speciate aqueous Mn, identical Mn and Fe recoveries may suggest a 1:1 reaction stoichiometry, meaning that Mn(III) was formed instead of Mn(II). Additional studies are currently being performed using extended X-ray absorption fine structure (EXAFS) spectroscopy to quantify Mn oxidation states of aqueous Mn initially produced from reactions with Fe(II) and Mn extracted from the solid phase. Control studies suspending unreacted pyrolusite particles in pH 1.0 buffered solutions, our most extreme extraction condition, produced minimal Mn release after several days, suggesting Mn(IV) is not simply leaching into solution.

Sustained redox activity with aqueous Fe(II)

Sustained exposure of pyrolusite particles to aqueous Fe(II) appears to induce noticeable shifts in observed Fe reaction products. After one reaction sequence with aqueous Fe(II), exposed surfaces of all visible Mn oxides are covered in needlelike precipitates, identified as lepidocrocite in XRD patterns (L - labeling, Figure B.6, B-C). As these Mn/Fe oxide particles are resuspended in new Fe(II)-containing buffer solutions, clusters of small round precipitates begin to emerge and eventually dominate observed surface morphology (Figure B.6, C, D).

^{57}Fe Mössbauer spectroscopy on Mn/Fe solids after successive resuspensions in aqueous Fe(II) indicate the formation of magnetite and/or maghemite (hereafter referred to as magnetite for simplicity). Magnetite commonly occurs as nanoscale spherical or cubic primary particles, consistent with observed particle morphology changes in SEM images (Figure B.6). Room-temperature Mössbauer spectra clearly indicate increasing multi-sextet character indicative of magnetite as cumulative Fe(II) loading increases (Figure B.7). Moreover, enriched ^{56}Fe and ^{57}Fe isotope experiments demonstrate sustained redox activity of newly introduced Fe(II) with Mn/Fe particles. Experiments were performed in which Mössbauer-active ^{57}Fe(II) was only exposed to Mn/Fe solids at the endpoint of reaction (all prior resuspensions in aqueous Fe(II) were performed using ^{56}Fe(II)). Mössbauer spectra collected after reaction of ^{57}Fe(II) in these cases provide a glimpse of marginal net reactivity of Fe(II) added to pyrolusite/lepidocrocite solids. In every case, ^{57}Fe(II) was observed to exist as an oxidized Fe solid consisting of lepidocrocite and/or magnetite, with no trace of adsorbed Fe(II) doublets (Figure B.7). This was observed even after 9 resuspensions in 3 mM aqueous Fe(II) (8 x ^{56}Fe(II) + 1 x ^{57}Fe(II)), resulting in an addition of 27 mM of e$^-$ to the system, exceeding theoretical electron-accepting capacity of initial pyrolusite (1 g/L = 23 mM e$^-$ for conversion of Mn(IV) to Mn(II)).

Attributing spectral area due to lepidocrocite (doublet) or magnetite (sextets) in Mössbauer data provides us with a means to quantify relative abundances of Fe phases

present among the total population of ^{57}Fe atoms in the sample. Magnetite can display superparamagnetic behavior, which would cause magnetite to appear as a doublet in Mössbauer spectra and induce error in our estimations [e.g., 153]. This effect is minimized at low temperatures, and because the lepidocrocite doublet observed in our experimental protocol did not order until ~ 20 K, spectral fitting was performed at 77 K to minimize the errors caused by potential magnetite superparamagnetism. Analysis of spectra shown above in Figure B.7 show a clear transition in marginal Fe(II) reaction products from lepidocrocite to predominantly magnetite after nine resuspensions in 3 mM aqueous Fe(II) (Figure B.8). Lepidocrocite transformation to magnetite in the presence of aqueous Fe(II) is a commonly observed phenomenon [154], accomplished though solid-state transformations of lepidocrocite [155]. A more quantitative assessment of the transition from lepidocrocite to magnetite precipitate formation is shown below in Table A.2, as calculated by determining the proportion of spectral area at 77 K within the doublet and multi-sextet areas, respectively.

Impacts on underlying Fe and Mn solids

After pyrolusite solids had been exposed to ^{57}Fe in the reaction sequence, additional resuspensions in aqueous ^{56}Fe(II) allowed us to monitor changes occurring in previously-deposited Fe precipitates without interference due to formation of additional Fe precipitates.

Mössbauer spectra collected after additional rounds of Fe(II) addition show a general increase in magnetite character and a relative decrease in lepidocrocite doublet area, demonstrating that Fe atoms deposited in an initial precipitate are still able to participate in redox reactions with aqueous Fe(II) (Figure B.9, Table B.2). A summary of spectral fitting for every sequential Fe isotope reaction series is shown in Table A.2. Phase changes in Fe precipitates from oxidized lepidocrocite to mixed-valent magnetite provide evidence that Fe precipitates are able to participate in redox reactions with aqueous Fe(II), suggesting Mn/Fe particle complexes can still be important redox-active phases in reactions with constituents like Fe(II).

From aqueous Fe(II) data and Mössbauer data collected after sequential resuspensions in aqueous Fe(II), it is apparent that aqueous Fe(II) can still participate in redox transformations with pyrolusite particles, even after a surface precipitate of Fe has been formed. It is not clear, however, whether additional aqueous Fe(II) is reacting with the underlying Mn oxide, or solely with the Fe oxide precipitate. It is apparent that lepidocrocite to magnetite redox transformations are consuming some of the electron equivalents provided by additional aqueous Fe(II), as demonstrated by [57]Fe Mössbauer spectra (Figure B.9). Resuspension of Mn/Fe particles in aqueous Fe(II) initiates a release of aqueous Mn in a similar non-stoichiometric fashion illustrated in Figure B.4 (Figure B.10), but no Mn is released into solution is the particles are simply resuspended in pH 7.5 buffer without aqueous Fe(II) (data not shown). Mn release from the solid phase upon Fe(II) addition could be an indication of further redox reaction between Mn(IV) and Fe(II). It could also simply be controlled by the physical changes that are taking place on the surface, as precipitated lepidocrocite is transformed to magnetite, allowing for release of adsorbed or incorporated Mn into solution. Regardless of the cause, aqueous Mn release in the presence of Fe(II) can be achieved despite the presence of an oxidized Fe surface precipitate, commonly thought to prevent further Mn chemical activity. As Fe precipitates may be prevalent on the surface of Mn oxides, the impact of Mn/Fe particle complexes on Mn release to environmental systems should not be ignored.

We analyzed solids formed after successive resuspensions in aqueous Fe(II) with XPS to examine the changes that occur to the near-surface manganese atoms after zero, one, or two reactions with aqueous Fe(II). It appears that after reaction with Fe(II), observed energy differences between Mn *2p* $^{3/2}$ and O *1s* peaks are reduced from 112.4 eV to 111.3 eV, indicative of a reduced oxidation state for near-surface Mn (Table A.3) [149]. This trend does not appear to continue, however, in pyrolusite particles that have been reacted twice with aqueous Fe(II). Mn *2p* $^{3/2}$ – O *1s* differences for pyrolusite reacted once or twice with aqueous Fe(II) are nearly equivalent, indicating that any near-surface Mn present after two reactions with Fe(II) has the same average oxidation

state as the near-surface Mn after only one reaction with Fe(II). XPS evidence seems to suggest the average redox state of near-surface Mn is not altered once an initial surface layer of Fe is deposited, indicating further redox transformations of Mn/Fe particles could be due to interactions with Fe precipitates, such as lepidocrocite in this case.

Conclusions

We have pursued a novel method to investigate evolving Fe-Mn heterogeneous redox activity, utilizing selective introduction of Fe isotopes in combination with [57]Fe Mössbauer spectroscopy to complement observations from bulk assessments of aqueous and solid phase transformations. In this fashion, we have shown that Fe(II) in the presence of pyrolusite at pH 7.5 stimulates rapid precipitation of a lepidocrocite phase with interesting morphology and possible incorporation of Mn (II) or Mn(III). Further redox reactions of Mn/Fe particle complexes with aqueous Fe(II) are still possible, as Fe precipitates can be reduced by exposure to additional Fe(II). Continued redox reactions with aqueous Fe(II) can also release additional Mn into solution, either through continued Fe-Mn redox activity or detachment of entrained manganese as surface properties of Mn/Fe particles complexes evolve. Contrary to assumptions previous assumptions, Mn oxide particles cannot simply be dismissed as passivated, redox-inactive phases after reaction with aqueous Fe(II), as important chemical transformations may still take place at Mn/Fe particle surfaces with newly increased surface area and reactive capacity.

Acknowledgements

Figures and Tables
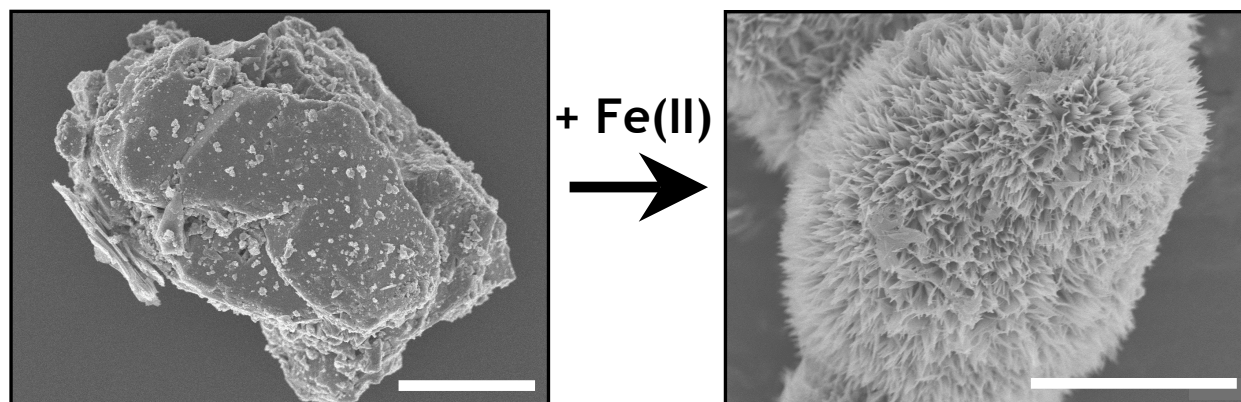
Figure B.1. Scanning electron micrographs reveal the significant changes in particle morphology that occur when unreacted pyrolusite particles (left panel) are exposed to aqueous Fe(II). Extensive needlelike surface precipitates (right panel) cover the surface of every particle that was imaged, after one reaction sequence of pyrolusite with 3 mM aqueous Fe(II). Scale bars on both images are 5 microns.
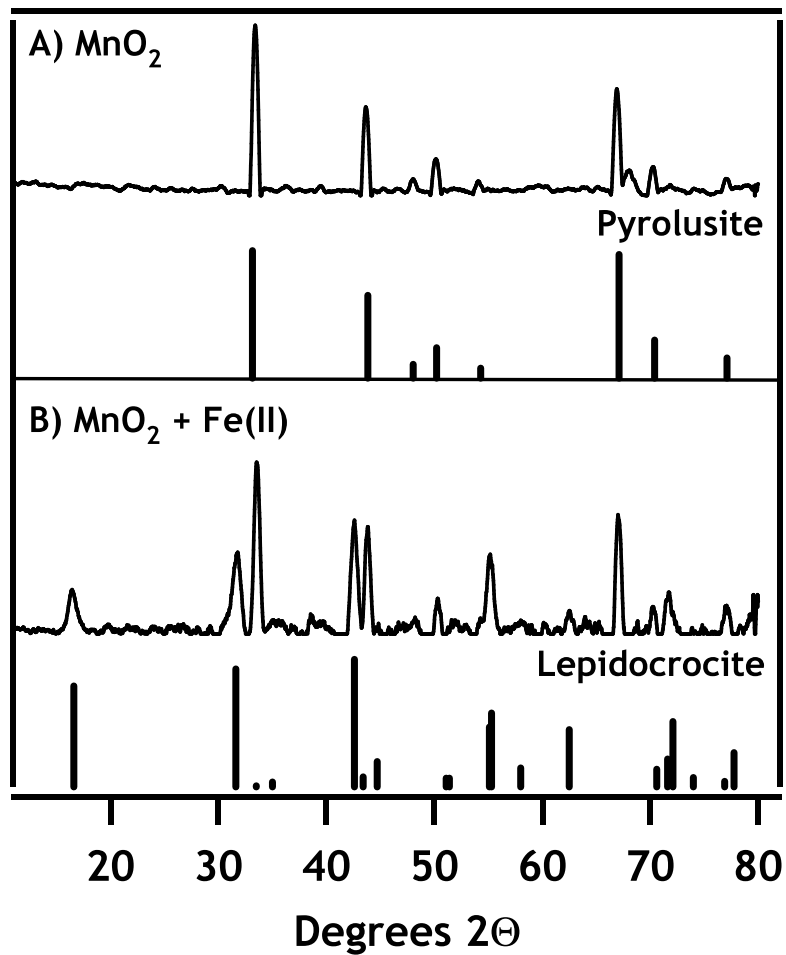
Figure B.2. X-ray diffraction patterns of MnO_2 particles before and after reaction with aqueous Fe(II). Pyrolusite and Lepidocrocite standard diffraction patterns are provided for reference.
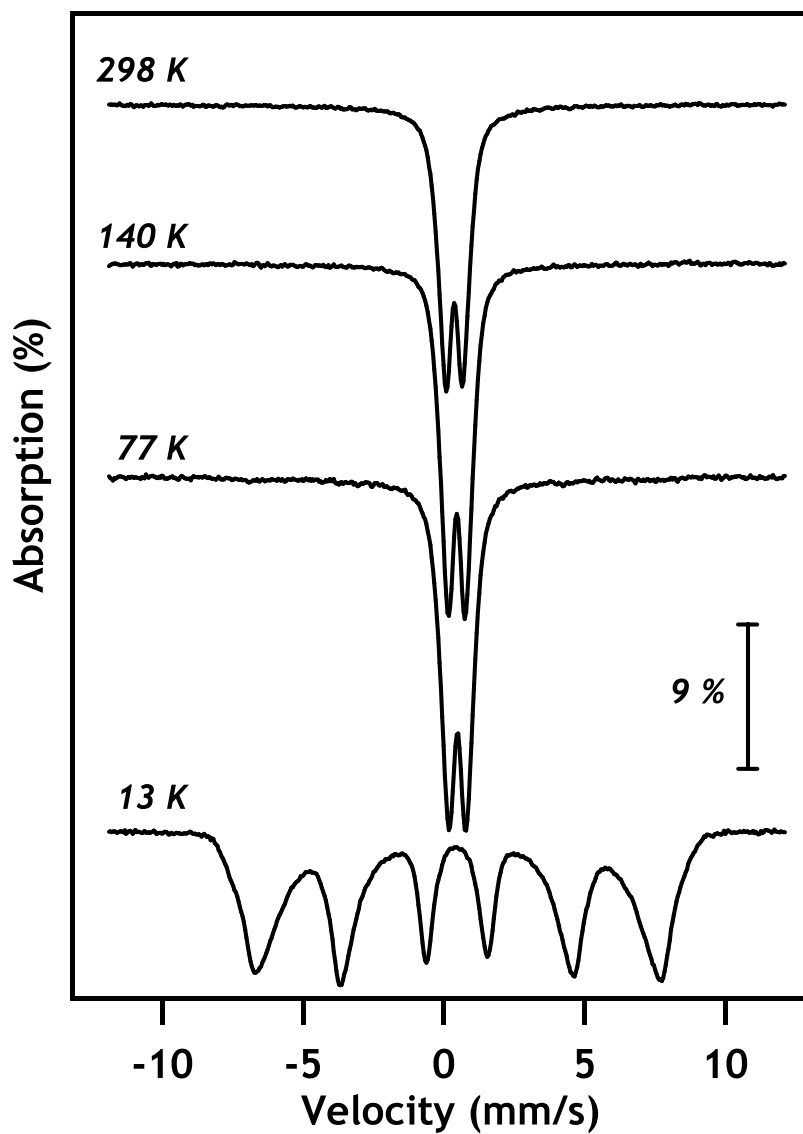
Figure B.3. Mössbauer spectra of pyrolusite reacted with 3 mM ^{57}Fe(II). Spectra were collected at temperatures ranging from room temperature (298 K) to 13 K.
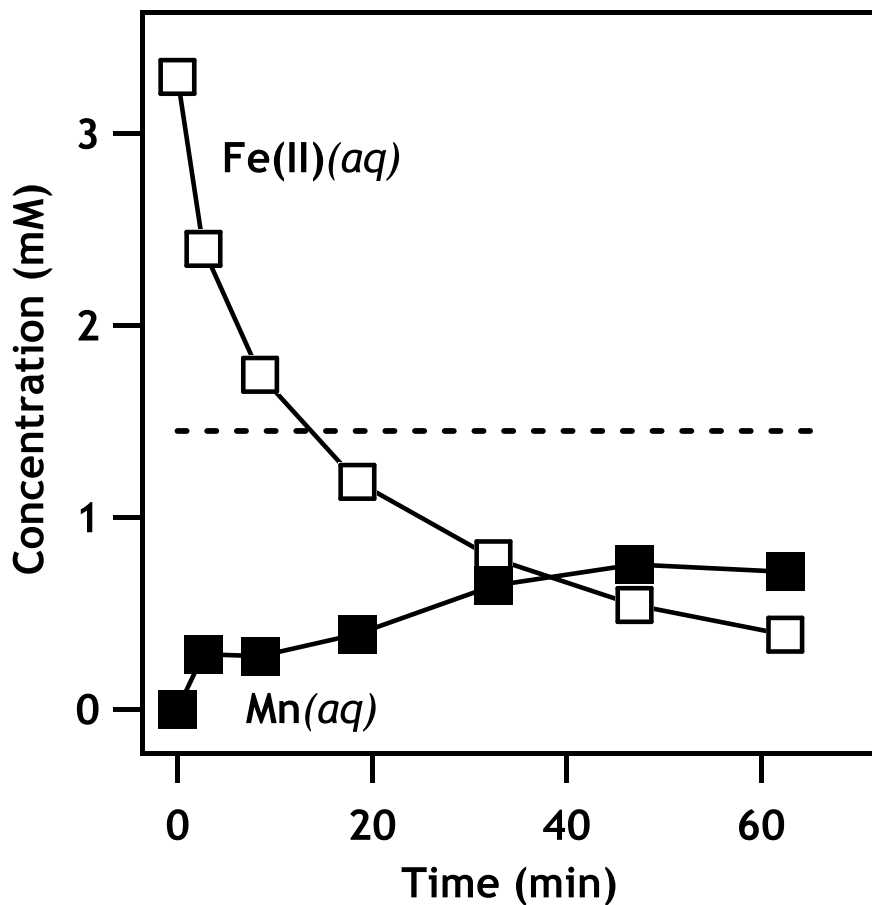
Figure B.4. Example kinetics of Fe(II) loss from, and Mn appearance into, the aqueous phase after aqueous Fe(II) exposure to pyrolusite solids batch reactors. Dashed line represents theoretical predictions of Mn(II) based on stoichiometric redox reaction between Fe(II) and Mn(IV), shown in equation 2.
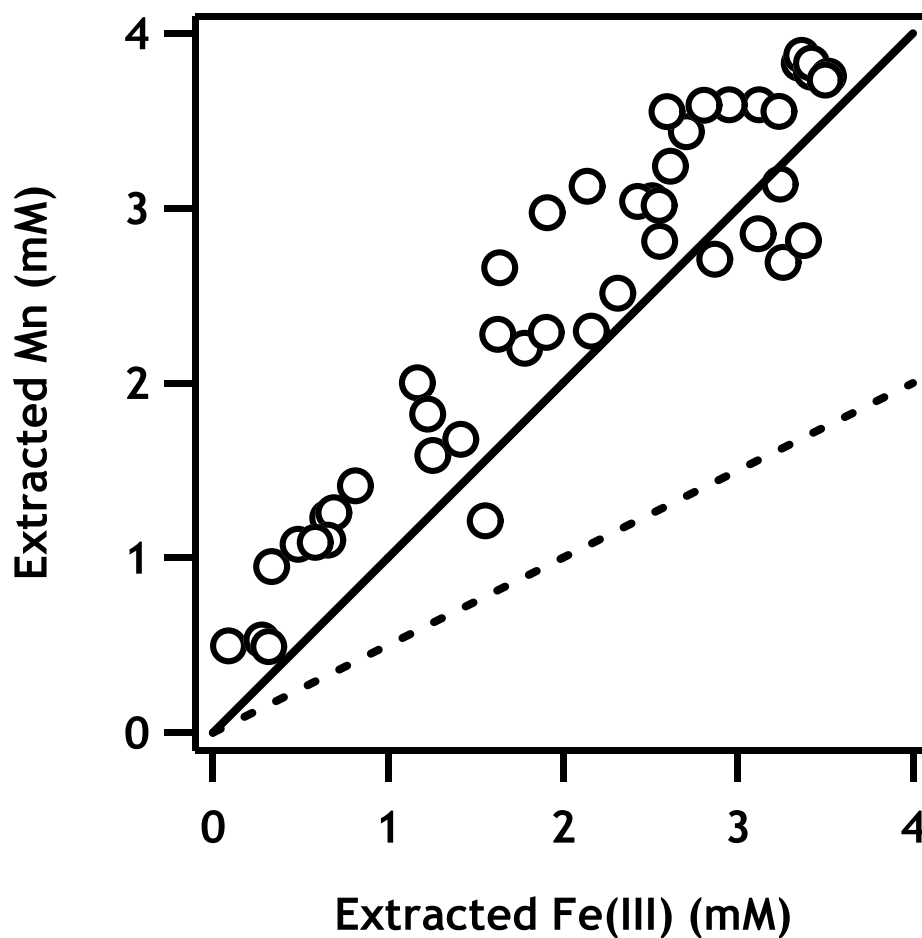
Figure B.5. Summary of recovered Fe(III) and Mn after resuspension of Mn/Fe mixed-phase solids in low pH acid extraction reactors. Theoretical extraction results based on a 1 Fe : 1 Mn (——) or 2 Fe : 1 Mn (- - - -) reaction stoichiometry are provided for reference. Data cluster more closely around the 1:1 reaction line, indicating that Fe(II) may be reacting with Mn(IV) to produce Mn(III), which remains in the solid phase. A majority of data points cluster above the 1:1 line, due to the presence of ~ 0.6 mM Mn already existing in solution at the onset of acid extraction, as a result of the initial reaction between pyrolusite and Fe(II).
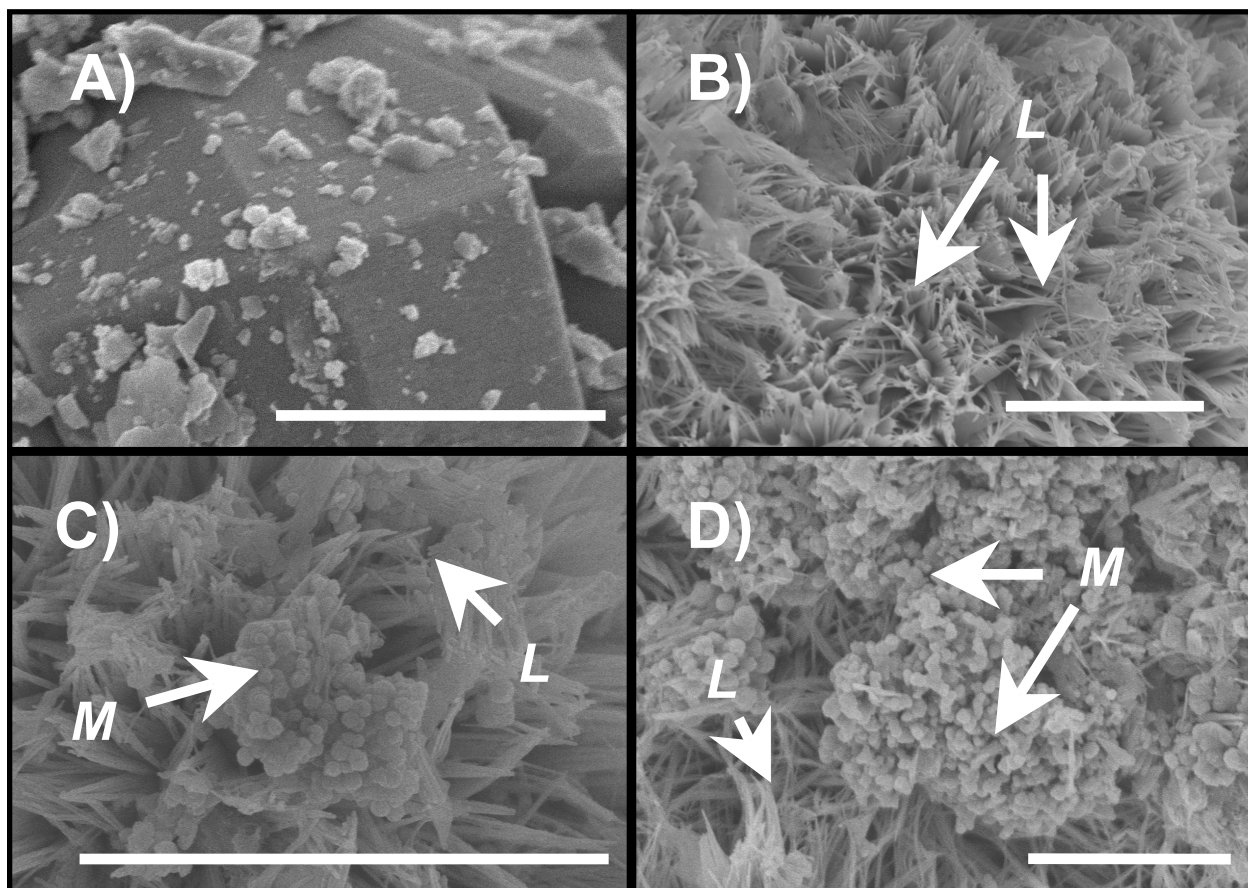
Figure B.6. Scanning electron micrographs of unreacted pyrolusite particles (A), alongside pyrolusite particles resuspended one (B), twice (C), or three times (D) in 3 mM aqueous Fe(II). Scale bars in all images are 2 microns long. During successive exposures of the Mn/Fe particles to aqueous Fe(II), the appearance of smaller, round magnetite/maghemite clusters (M) begin to overtake the initial needlelike lepidocrocite (L) precipitates formed on the Mn surface. Fe phase identification as magnetite or maghemite is on the basis of observed morphology, [57]Fe Mössbauer spectroscopy, and x-ray diffraction results.
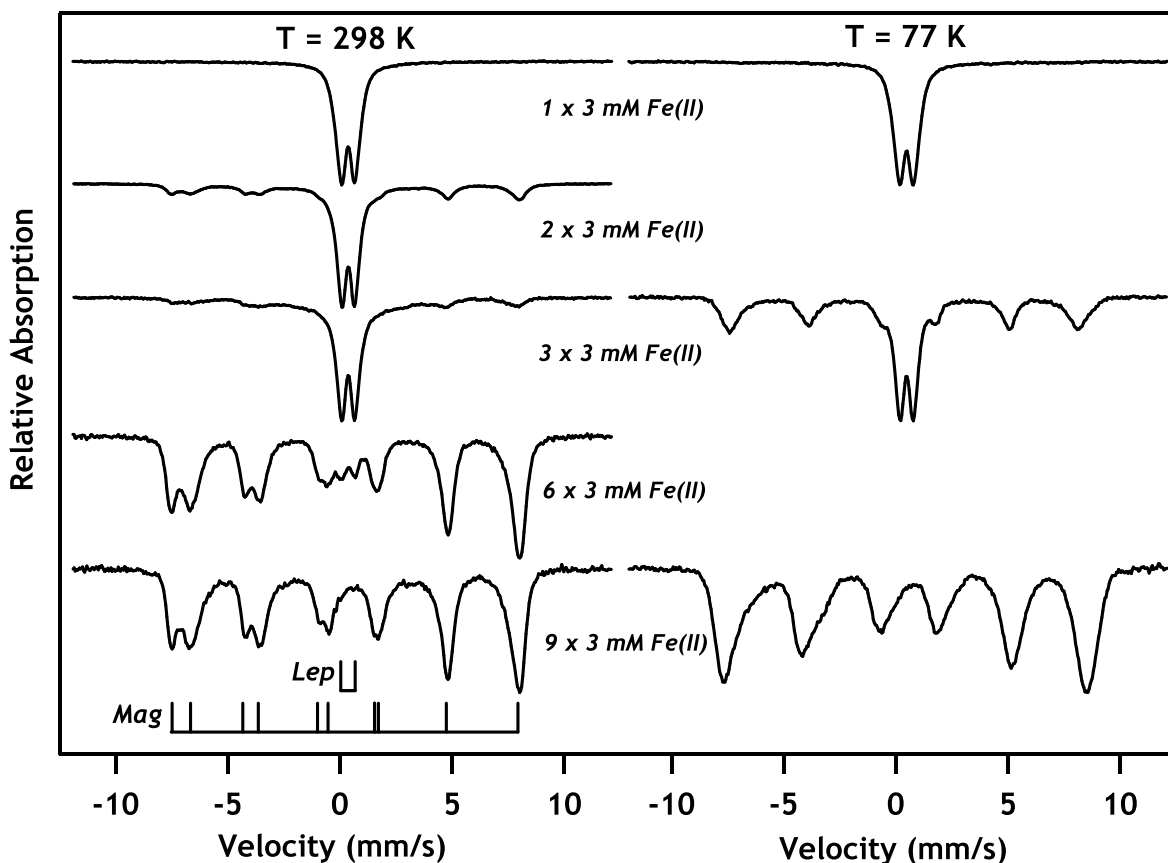
Figure B.7. [57]Fe Mössbauer spectra of all experimental data collected in which only the final resuspension of Mn particles was done using [57]Fe(II). Room temperature (RT, 298 K) spectra are provided for all experiments (left column), with selected 77 K spectra of identical experiments (right column) for comparison. After only one resuspension in 3 mM Fe(II), the resulting spectrum is devoid of multi-sextet character typical of magnetite. As the amount of Fe(II) exposure increases, we can see the final deposition of [57]Fe atoms onto the particle surface results in an increasingly large multi-sextet signal and a gradual disappearance of the doublet associated with lepidocrocite formation. Comparing RT spectra with 77 K, magnetite sextets appear to overlap more thoroughly at 77 K, which is commonly observed below the Verwey transition temperature (~ 120 K). Spectra collected at 77 K also contain a visibly higher ratio of sextet : doublet spectral area, possibly indicating the presence of unordered magnetite at room temperature, which orders into a typical sextet at lower collection temperatures.
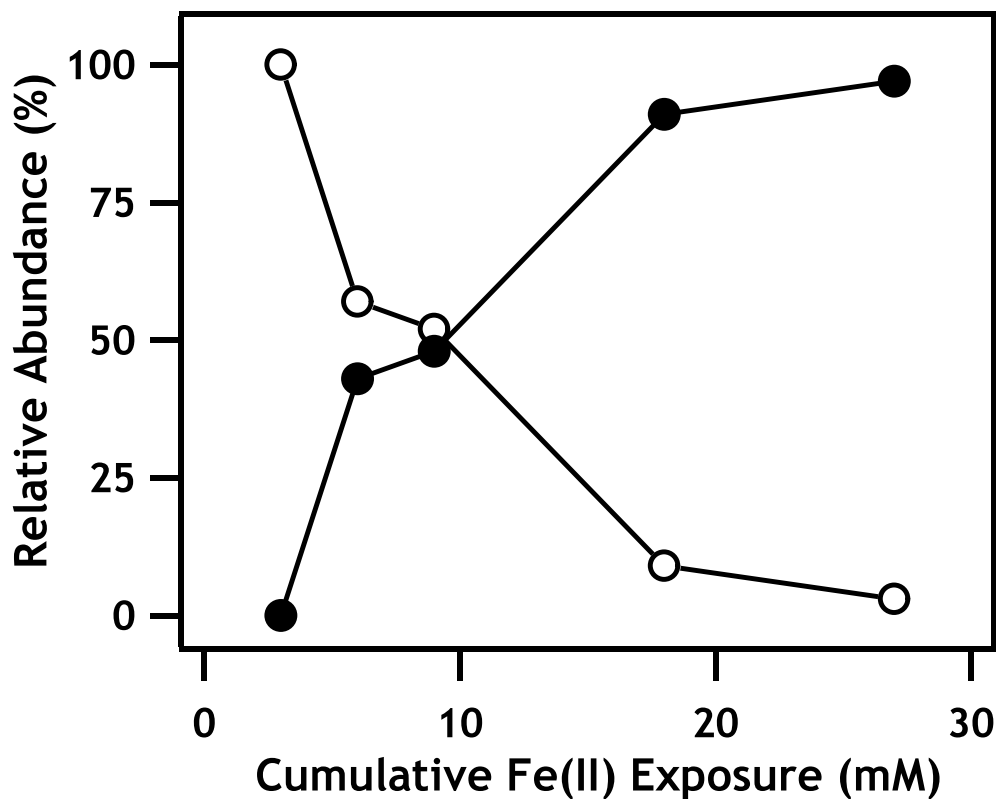
Figure B.8. Relative abundances of lepidocrocite (open markers) and magnetite (closed markers) in marginal Fe(II) additions, as determined my Mössbauer spectral fitting of Fe phases at 77 K. Experiments were only exposed to [57]Fe during the final Fe(II) resuspension, permitting us to view chemical changes occurring to the marginal Fe(II) addition. After initial reaction of pyrolusite with 3 mM Fe(II), only lepidocrocite was detectable in Mössbauer spectra. Increasing Fe(II) exposure resulted in marginal Fe precipitate formation increasingly dominated by magnetite, as identified by characteristic overlapping sextets in Mössbauer spectra.
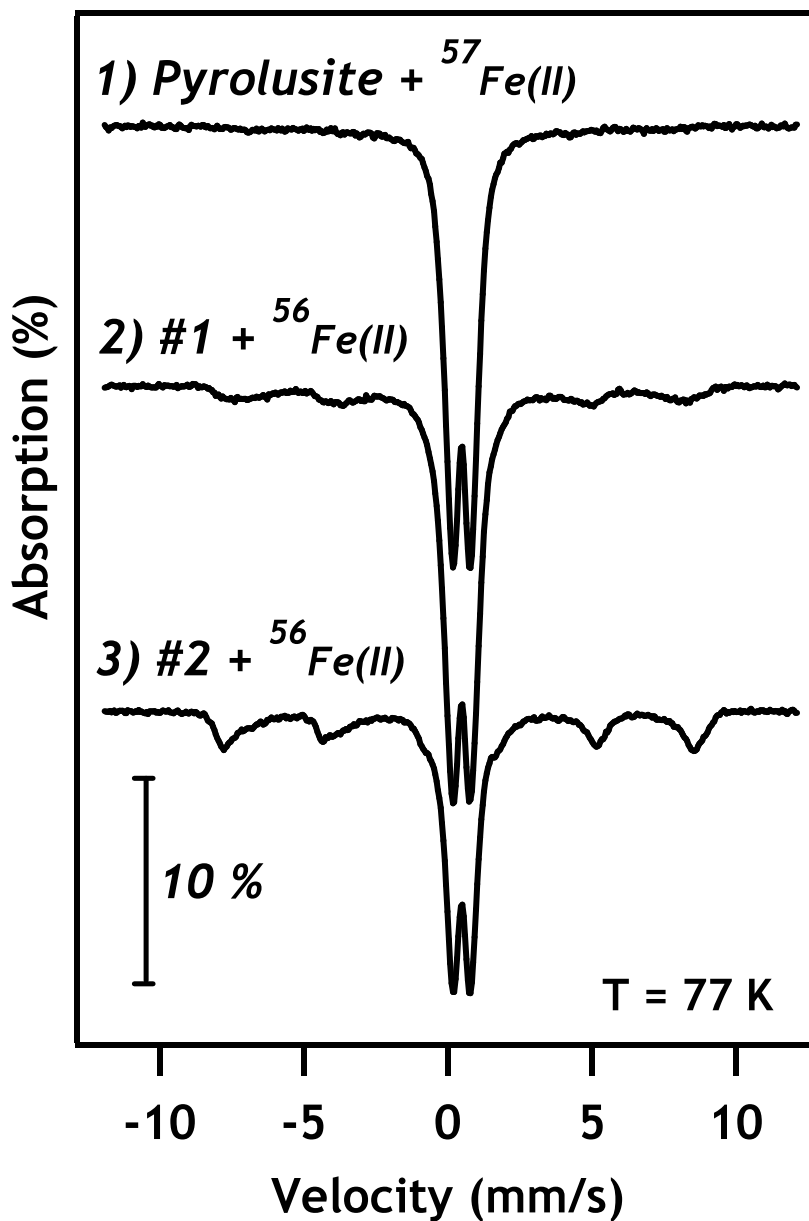
Figure B.9. [57]Fe Mössbauer spectra of pyrolusite resuspended 1, 2, and 3 times in 3 mM aqueous Fe(II), where the Fe isotope order of addition was [57]Fe-[56]Fe-[56]Fe. A marked increase in magnetite character can be observed in successive spectra, which is indicative of chemical transformations occurring only in the initial [57]Fe atoms oxidized and precipitated on the pyrolusite surface.
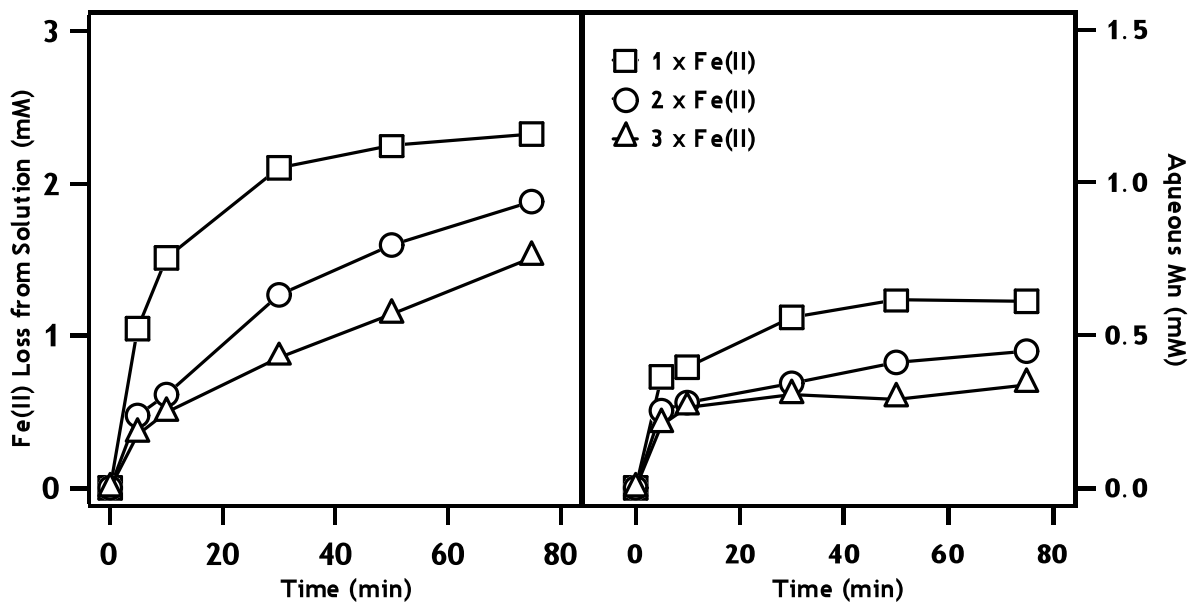
Figure B.10. Kinetics of Fe(II) loss from (left panel, open markers) and Mn appearance into (right panel, filled markers) the aqueous phase. Squares (□) indicate data for the initial suspension of pyrolusite in Fe(II), circles (○) and triangles (Δ) indicate second and third resuspensions, respectively. Initial Fe(II) concentrations for this series of experiments were 2.4 mM. Note the difference in y-axis scaling between the two panels.

Table B.1. Summary of acid extraction data after reaction of 1 g/L pyrolusite with 3 mM Fe(II).

Sample No.	Acid Added[a] (mmol HCl)	Time (hr)	Fe(III) Extracted (mM)	Mn Extracted (mM)	Fe(III)$_{ext}$: Fe(II)$_0$[b]	Fe(III)$_{ext}$: Mn$_{ext}$[c]
1	12.5	24.25	2.51	3.04	0.74	0.82
2	12.5	50.5	3.12	3.59	0.93	0.87
3	12.5	98.5	3.35	3.83	0.99	0.88
4	12.5	143.75	3.37	3.87	1	0.87
5	12.5	24.25	2.43	3.04	0.72	0.8
6	12.5	50.5	2.95	3.59	0.87	0.82
7	12.5	98.5	3.42	3.78	1.01	0.91
8	12.5	143.75	3.42	3.83	1.01	0.89
9	12.5	24.25	2.55	3.02	0.75	0.85
10	12.5	50.5	3.23	3.55	0.95	0.91
11	12.5	98.5	3.52	3.76	1.04	0.94
12	12.5	143.75	3.5	3.73	1.03	0.94
13	7.5	7.58	1.23	1.82	0.34	0.67
14	7.5	19.42	1.64	2.66	0.45	0.62
15	7.5	77.08	2.59	3.55	0.71	0.73
16	7.5	105.58	2.81	3.59	0.77	0.78
17	7.5	213.08	3.24	3.14	0.89	1.03
18	7.5	314.5	3.37	2.81	0.93	1.2
19	6.25	7.58	1.42	1.68	0.42	0.84
20	6.25	19.42	1.63	2.28	0.49	0.71
21	6.25	77.08	2.61	3.24	0.78	0.81
22	6.25	105.58	2.71	3.44	0.81	0.79
23	6.25	213.08	3.12	2.85	0.93	1.09
24	6.25	314.5	3.26	2.69	0.97	1.21
25	5	7.58	0.81	1.41	0.25	0.58
26	5	19.42	1.17	2	0.35	0.58
27	5	77.08	1.91	2.97	0.57	0.64
28	5	105.58	2.14	3.13	0.64	0.68
29	5	213.08	2.55	2.81	0.77	0.91
30	5	314.5	2.87	2.71	0.86	1.06
31	3.75	7.58	1.56	1.21	0.46	1.28
32	3.75	19.42	1.26	1.59	0.37	0.79
33	3.75	77.08	1.78	2.2	0.53	0.81
34	3.75	105.58	1.9	2.29	0.57	0.83
35	3.75	213.08	2.16	2.3	0.64	0.94
36	3.75	314.5	2.31	2.51	0.69	0.92
37	2.5	7.58	0.34	0.95	0.1	0.35
38	2.5	19.42	0.49	1.08	0.15	0.45
39	2.5	77.08	0.66	1.23	0.2	0.53
40	2.5	105.58	0.69	1.26	0.21	0.55
41	2.5	213.08	0.66	1.1	0.2	0.6

a- Acid added as a spike of 5 M HCl.

b- Refers to the ratio of recovered Fe(III) as compared to Fe(II) concentration initially present in reactors before oxidation by pyrolusite.

c- Ratio of extracted Fe(III) to extracted Mn, at each time point.

Table B.2. Relative abundances of lepidocrocite and magnetite/maghemite appearing in [57]Fe Mössbauer spectra at 77 K.

Fe(II) Addition	Appearance of [57]Fe(II) in series[a]				
	1st (Lep. / Mag.)	2nd (Lep. / Mag.)	3rd (Lep. / Mag.)	6th (Lep. / Mag.)	9th (Lep. / Mag.)
# 1	100 / 0	NA[b]	NA	NA	NA
# 2	85 / 15	57 / 43	NA	NA	NA
# 3	75 / 25	46 / 54	52 / 48	NA	NA
# 6	----[c]	----	----	9 / 91	NA
# 9	----	----	----	----	3 / 97

a – Refers to the position of single [57]Fe(II) resuspension in the resuspension sequence. All other Fe(II) resuspensions were performed using [56]Fe(II), which would not contribute to observed Mössbauer spectra.

b – NA due to addition of [56]Fe(II) in this position. No Mössbauer spectral features were observed, as [56]Fe(II) is not visible to Mössbauer spectroscopy.

c – Dashed lines indicate that the experiment has not been performed.

Table B.3. Summary of XPS data for manganese oxidation state characterization.

	Sample Description[a]		
	β-MnO$_2$	β-MnO$_2$ + Fe(II)	β-MnO$_2$ + Fe(II) + Fe(II)
Mn $2p^3/_2$ (eV)	641.5	638.9	640.2
O $1s$ (eV)	529.1	527.6	528.8
Mn $2p^3/_2$ – O $1s$ (eV)	112.4	111.3	111.4

a- Pyrolusite particles were reacted with aqueous Fe(II) using identical experimental conditions as other reported work (pH 7.5, 1 g/L pyrolusite, 3 mM Fe(II)).

REFERENCES

1. Ronov, A.B. and A.A. Yaroshevsky, *Chemical composition of the earth's crust*, in *The earth's crust and upper mantle*, P.J. Hart, Editor. 1969, American Geophysical Union: Washington, D.C.

2. Amonette, J.E., *Iron redox chemistry of clays and oxides: Environmental implications*, in *Electrochemistry of Clays*, A. Fitch, Editor. 2002, Clay Minerals Society: Aurora, CO.

3. Stucki, J.W., *Structural Iron in Smectites*, in *Iron in Soils and Clay Minerals*, J.W. Stucki, B.A. Goodman, and U. Schwertmann, Editors. 1988, D. Reidel: Dordrecht, The Netherlands. p. 625-675.

4. Montes-H, G., et al., *Influence of interlayer cations on the water sorption and swelling-shrinkage of MX80 bentonite.* Applied Clay Science, 2003. **23**(5-6): p. 309-321.

5. Stucki, J.W., et al., *EFFECTS OF OXIDATION-STATE OF OCTAHEDRAL IRON ON CLAY SWELLING.* Clays and Clay Minerals, 1984. **32**(5): p. 357-362.

6. Luca, V., *Detection of tetrahedral Fe-3+ sites in nontronite and vermiculite by Mössbauer-spectroscopy.* Clays and Clay Minerals, 1991. **39**(5): p. 467-477.

7. Manceau, A., et al., *Oxidation-reduction mechanism of iron in dioctahedral smectites: I. Crystal chemistry of oxidized reference nontronites.* American Mineralogist, 2000. **85**(1): p. 133-152.

8. Merola, R.B. and M.M. McGuire, *Crystallographic site distribution and redox activity of Fe in nontronites determined by optical spectroscopy.* Clays and Clay Minerals, 2009. **57**(6): p. 771-778.

9. Keeling, J.L., M.D. Raven, and W.P. Gates, *Geology and characterization of two hydrothermal nontronites from weathered metamorphic rocks at the Uley Graphite Mine, South Australia.* Clays and Clay Minerals, 2000. **48**(5): p. 537-548.

10. Williams, A.G.B. and M.M. Scherer, *Spectroscopic evidence for Fe(II)-Fe(III) electron transfer at the iron oxide-water interface.* Environmental Science & Technology, 2004. **38**(18): p. 4782-4790.

11. Handler, R.M., et al., *Atom Exchange between Aqueous Fe(II) and Goethite: An Fe Isotope Tracer Study.* Environmental Science & Technology, 2009. **43**(4): p. 1102-1107.

12. Yanina, S.V. and K.M. Rosso, *Linked reactivity at mineral-water interfaces through bulk crystal conduction.* Science, 2008. **320**(5873): p. 218-222.

13. Merola, R.B., E.D. Fournier, and M.M. McGuire, *Spectroscopic investigations of Fe2+ complexation on nontronite clay.* Langmuir, 2007. **23**(3): p. 1223-1226.

14. Jaisi, D.P., et al., *Fe2+ sorption onto nontronite (NAu-2).* Geochimica Et Cosmochimica Acta, 2008. **72**(22): p. 5361-5371.

15. Hofstetter, T.B., R.P. Schwarzenbach, and S.B. Haderlein, *Reactivity of Fe(II) species associated with clay minerals.* Environmental Science & Technology, 2003. **37**(3): p. 519-528.

16. Hofstetter, T.B., A. Neumann, and R.P. Schwarzenbach, *Reduction of nitroaromatic compounds by Fe(II) species associated with iron-rich smectites.* Environmental Science & Technology, 2006. **40**(1): p. 235-242.

17. Neumann, A., et al., *Assessing the Redox Reactivity of Structural Iron in Smectites Using Nitroaromatic Compounds As Kinetic Probes.* Environmental Science & Technology, 2008. **42**(22): p. 8381-8387.

18. Neumann, A., et al., *Reduction of Polychlorinated Ethanes and Carbon Tetrachloride by Structural Fe(II) in Smectites.* Environmental Science & Technology, 2009. **43**(11): p. 4082-4089.

19. Schultz, C.A. and T.J. Grundl, *pH dependence on reduction rate of 4-Cl-nitrobenzene by Fe(II)/montmorillonite systems.* Environmental Science & Technology, 2000. **34**(17): p. 3641-3648.

20. Gu, C., et al., *Octachlorodibenzodioxin formation on Fe(III)-montmorillonite clay.* Environmental Science & Technology, 2008. **42**(13): p. 4758-4763.

21. Anastacio, A.S., et al., *Characterization of a redox-modified clay mineral with respect to its suitability as a barrier in radioactive waste confinement.* Applied Clay Science, 2008. **39**(3-4): p. 172-179.

22. Favre, F., et al., *Changes in the CEC of a soil smectite-kaolinite clay fraction as induced by structural iron reduction and iron coatings dissolution.* Applied Clay Science, 2006. **34**(1-4): p. 95-104.

23. Lear, P.R. and J.W. Stucki, *Effects of Iron Oxidation-State on the Specific Surface-Area of Nontronite.* Clays and Clay Minerals, 1989. **37**(6): p. 547-552.

24. Stucki, J.W., D.C. Golden, and C.B. Roth, *EFFECTS OF REDUCTION AND REOXIDATION OF STRUCTURAL IRON ON THE SURFACE-CHARGE AND*

DISSOLUTION OF DIOCTAHEDRAL SMECTITES. Clays and Clay Minerals, 1984. **32**(5): p. 350-356.

25.   Yan, L.B. and J.W. Stucki, *Structural perturbations in the solid-water interface of redox transformed nontronite.* Journal of Colloid and Interface Science, 2000. **225**(2): p. 429-439.

26.   Jaisi, D.P., H.L. Dong, and J.P. Morton, *Partitioning of Fe(II) in reduced nontronite (NAu-2) to reactive sites: Reactivity in terms of Tc(VII) reduction.* Clays and Clay Minerals, 2008. **56**(2): p. 175-189.

27.   Jaisi, D.P., et al., *Reduction and long-term immobilization of technetium by Fe(II) associated with clay mineral nontronite.* Chemical Geology, 2009. **264**(1-4): p. 127-138.

28.   Peretyazhko, T., et al., *Heterogeneous reduction of Tc(VII) by Fe(II) at the solid-water interface.* Geochimica Et Cosmochimica Acta, 2008. **72**(6): p. 1521-1539.

29.   Ilton, E.S., et al., *Reduction of uranyl in the interlayer region of low iron micas under anoxic and aerobic conditions.* Environmental Science & Technology, 2006. **40**(16): p. 5003-5009.

30.   Boparai, H.K., et al., *Dechlorinating chloroacetanilide herbicides by dithionite-treated aquifer sediment and surface soil.* Environmental Science & Technology, 2006. **40**(9): p. 3043-3049.

31.   Sorensen, K.C., et al., *Alteration of mammalian-cell toxicity of pesticides by structural iron(II) in ferruginous smectite.* Environmental Science & Technology, 2004. **38**(16): p. 4383-4389.

32.   Ernstsen, V., *Reduction of nitrate by Fe2+ in clay minerals.* Clays and Clay Minerals, 1996. **44**(5): p. 599-608.

33.   Ernstsen, V., W.P. Gates, and J.W. Stucki, *Microbial reduction of structural iron in clays - A renewable source of reduction capacity.* Journal of Environmental Quality, 1998. **27**(4): p. 761-766.

34.   Murad, E. and J. Cashion, *Mössbauer Spectroscopy of Environmental Materials and their Industrial Utilization*. 2004, New York: Kluwer Academic Publishers.

35.   Dyar, M.D., et al., *Mossbauer spectroscopy of earth and planetary materials.* Annual Review of Earth and Planetary Sciences, 2006. **34**: p. 83-125.

36.   Rancourt, D.G., *Mossbauer spectroscopy in clay science.* Hyperfine Interactions, 1998. **117**(1-4): p. 3-38.

37.   Hellerkallai, L. and I. Rozenson, *The Use of Mossbauer-Spectroscopy of Iron in Clay Mineralogy.* Physics and Chemistry of Minerals, 1981. **7**(5): p. 223-238.

38.   Nano, G.V. and T.J. Strathmann, *Ferrous iron sorption by hydrous metal oxides.* Journal of Colloid and Interface Science, 2006. **297**(2): p. 443-454.

39.   Nano, G.V. and T.J. Strathmann, *Application of surface complexation modeling to the reactivity of iron(II) with nitroaromatic and oxime carbamate contaminants in aqueous TiO2 suspensions.* Journal of Colloid and Interface Science, 2008. **321**(2): p. 350-359.

40.   Gorski, C.A. and M.M. Scherer, *Influence of Magnetite Stoichiometry on Fe-II Uptake and Nitrobenzene Reduction.* Environmental Science & Technology, 2009. **43**(10): p. 3675-3680.

41.   Larese-Casanova, P. and M.M. Scherer, *Fe(II) sorption on hematite: New insights based on spectroscopic measurements.* Environmental Science & Technology, 2007. **41**(2): p. 471-477.

42.   Cornell, R.M. and U. Schwertmann, *The Iron Oxides: Structure, Properties, Reactions, Occurrence, and Uses*. 1996, New York: VCH.

43.   Hiemstra, T. and W.H. van Riemsdijk, *Adsorption and surface oxidation of Fe(II) on metal (hydr)oxides.* Geochimica Et Cosmochimica Acta, 2007. **71**(24): p. 5913-5933.

44.   Stumm, W., *Chemistry of the Solid-Water Interface: Processes at the Mineral-Water and Particle-Water Interface of Natural Systems*. 1992, New York: Wiley.

45.   Rosso, K.M., et al., *Connecting Observations of Hematite (alpha-Fe2O3) Growth Catalyzed by Fe(II).* Environmental Science & Technology, 2010. **44**(1): p. 61-67.

46.   Tor, J.M., et al., *Trifluralin degradation under microbiologically induced nitrate and Fe(III) reducing conditions.* Environmental Science & Technology, 2000. **34**(15): p. 3148-3152.

47.   Xu, J.C., et al., *Fate of atrazine and alachlor in redox-treated ferruginous smectite.* Environmental Toxicology and Chemistry, 2001. **20**(12): p. 2717-2724.

48.   Manceau, A., et al., *Oxidation-reduction mechanism of iron in dioctahedral smectites: II. Crystal chemistry of reduced Garfield nontronite.* American Mineralogist, 2000. **85**(1): p. 153-172.

49.   Jaisi, D.P., et al., *Control of Fe(III) site occupancy on the rate and extent of microbial reduction of Fe(III) in nontronite.* Geochimica Et Cosmochimica Acta, 2005. **69**(23): p. 5429-5440.

50.   Stucki, J.W., G.W. Bailey, and H.M. Gan, *Oxidation-reduction mechanisms in iron-bearing phyllosilicates.* Applied Clay Science, 1996. **10**(6): p. 417-430.

51.   Gehin, A., et al., *Reversible surface-sorption-induced electron-transfer oxidation of Fe(II) at reactive sites on a synthetic clay mineral.* Geochimica Et Cosmochimica Acta, 2007. **71**(4): p. 863-876.

52.   Schilt, A.A., *Analytical Applications of 1,10-Phenanthroline and Related Compounds*. 1st ed. 1969, Oxford: Permagon Press.

53.   Rancourt, D.G. and J.Y. Ping, *Voigt-based methods for arbitrary-shape static hyperfine parameter distributions in Mössbauer-spectroscopy.* Nuclear Instruments & Methods in Physics Research Section B-Beam Interactions with Materials and Atoms, 1991. **58**(1): p. 85-97.

54.   Ribeiro, F.R., et al., *Comparisons of structural iron reduction in smectites by bacteria and dithionite: II. A variable-temperature Mossbauer spectroscopic study of Garfield nontronite.* Pure and Applied Chemistry, 2009. **81**(8): p. 1499-1509.

55.   Komadel, P., P.R. Lear, and J.W. Stucki, *Reduction and Reoxidation of Nontronite - Extent of Reduction and Reaction-Rates.* Clays and Clay Minerals, 1990. **38**(2): p. 203-208.

56.   Larese-Casanova, P. and M.M. Scherer, *Morin transition suppression in Polycrystalline (57)Hematite (alpha-Fe2O3) exposed to Fe-56(II).* Hyperfine Interactions, 2007. **174**(1-3): p. 111-119.

57.   Murad, E. and J. Cashion, *Mossbauer Spectroscopy of Environmental Materials and their Industrial Utilization*. 2006, Dordrecht: Kluwer. 417.

58.   Cardile, C.M., J.H. Johnston, and D.P.E. Dickson, *Magnetic-Ordering at 4.2-K and 1.3-K in Nontronites of Different Iron Contents - a Fe-57 Mossbauer Spectroscopic Study.* Clays and Clay Minerals, 1986. **34**(3): p. 233-238.

59.   Murad, E. and U. Schwertmann, *The influence of crystallinity of the Mössbauer spectrum of lepidocrocite.* Mineralogical Magazine, 1984. **48**: p. 507-511.

60.   Burns, R.G., et al., *Mixed-Valence Minerals of Iron and Titanium: Correlations of Structural, Mossbauer and Electronic Spectral Data*, in *Mixed-Valence Compounds*, D.B. Brown, Editor. 1979, D. Reidel: Dordrecht: Holland. p. 295-336.

61.   Rosso, K.M. and E.S. Ilton, *Charge transport in micas: The kinetics of Fe-II/III electron transfer in the octahedral sheet.* Journal of Chemical Physics, 2003. **119**(17): p. 9207-9218.

62.   Coey, J.M.D., A. Moukarika, and C.M. McDonagh, *Electron hopping in cronstedtite.* Solid State Communications, 1982. **41**(11): p. 797-800.

63.   Charradi, K., et al., *H2O2 determination at iron-rich clay modified electrodes.* Electrochimica Acta, 2009. **54**(17): p. 4237-4244.

64.   Gan, H., J.W. Stucki, and G.W. Bailey, *Reduction of structural iron in ferruginous smectite by free-radicals.* Clays and Clay Minerals, 1992. **40**(6): p. 659-665.

65.   Nealson, K.H. and C.R. Myers, *Microbial reduction of manganese and iron: New approaches to carbon cycling.* App. Environ. Microbiol., 1992. **58**(2): p. 439-443.

66.   Lovely, D.R., *Microbial Fe(III) reduction in subsurface environments.* FEMS Microbiology Reviews, 1997. **20**: p. 305-313.

67.   Elsner, M., R.P. Schwarzenbach, and S.B. Haderlein, *Reactivity of Fe(II)-bearing minerals toward reductive transformation of organic contaminants.* Environ. Sci. Technol., 2004. **38**(3): p. 799-807.

68.   Klausen, J., et al., *Reduction of substituted nitrobenzenes by Fe(II) in aqueous mineral suspensions.* Environmental Science and Technology, 1995. **29**(9): p. 2396-2404.

69.   McCormick, M.L. and P. Adriaens, *Carbon tetrachloride transformation on the surface of nanoscale biogenic magnetite particles.* Environ. Sci. Technol., 2004. **38**(4): p. 1045-1053.

70.   Gregory, K.B., et al., *Abiotic transformation of hexahydro-1,3,5-trinitro-1,3,5-triazine by Fe^{II} bound to magnetite.* Environmental Science and Technology, 2004. **38**(5): p. 1408-1414.

71.   Gander, J.W., G.F. Parkin, and M.M. Scherer, *Kinetics of 1,1,1-trichloroethane transformation by iron sulfide and a methanogenic consortium.* Environmental Science & Technology, 2002. **36**(21): p. 4540-4546.

72.   Hofstetter, T.B., et al., *Complete reduction of TNT and other (poly)nitroaromatic compounds under iron-reducing subsurface conditions.* Environmental Science and Technology, 1999. **33**(9): p. 1479-1487.

73.   Liger, E., L. Charlet, and P. Van Cappellen, *Surface catalysis of uranium(VI) reduction by iron(II).* Geochimica et Cosmochimica Acta, 1999. **63**(19-20): p. 2939-2955.

74.   Strathmann, T.J. and A.T. Stone, *Mineral surface catalysis of reactions between Fe^{II} and oxime carbamate pesticides.* Geochimica et Cosmochimica Acta, 2003. **67**(15): p. 2775-2791.

75.   Anastasio, C. and S.T. Martin, *Atmospheric Nanoparticles*, in *Nanoparticles and the Environment*, J.F. Banfield and A. Navrotsky, Editors. 2001, The Mineralogical Society of America: Washington, D.C. p. 293-349.

76.   Penn, R.L., et al., *Iron oxide coatings on sand grains from Atlantic coastal plain: High-resolution transmission electron microscopy characterization.* Geology, 2001. **29**(9): p. 843-846.

77.   Poulton, S. and R. Raiswell, *Chemical and physical characteristics of iron oxides in riverine and glacial meltwater sediments.* Chemical Geology, 2005. **218**: p. 203-221.

78.   Swartz, C.H., A.L. Ulery, and P.M. Gschwend, *An AEM-TEM study of nanometer-scale mineral associations in an aquifer sand: Implications for colloid mobilization.* Geochim. Cosmochim. Acta, 1997. **61**(4): p. 707-718.

79.   van der Zee, C., et al., *Nanogoethite is the dominant reactive oxyhydroxide phase in lake and marine sediments.* Geology, 2003. **31**(11): p. 993-996.

80.   Navrotsky, A., *Thermochemistry of Nanomaterials*, in *Nanoparticles and the Environment*, J.F. Banfield and A. Navrotsky, Editors. 2001, Mineralogical Society of America: Washington, D.C. p. 73-104.

81.   Waychunas, G.A., C.S. Kim, and J.F. Banfield, *Nanoparticulate iron oxide minerals in soils and sediments: Unique properties and contaminant scavenging mechanisms.* Journal of Nanoparticle Research, 2005. **7**: p. 409-433.

82.   Cornell, R.M. and U. Schwertmann, *The Iron Oxides: Structure, Properties, Reactions, Occurrences and Uses* 2nd ed. 2003, Weinheim, Germany: Wiley-VCH. 664.

83.   Langmuir, D., *Particle size effect on the reaction goethite = hematite + water.* Am. J. Sci., 1971. **271**: p. 147-156.

84.   Klabunde, K.J., et al., *Nanocrystals as stoichiometric reagents with unique surface chemistry.* J. Phys. Chem., 1996. **100**: p. 12142-12153.

85.   Banfield, J.F. and H. Zhang, *Nanoparticles in the Environment*, in *Nanoparticles and the Environment*, J.F. Banfield and A. Navrotsky, Editors. 2001, The Mineralogical Society of America: Washington, D.C. p. 1-58.

86.   Anschutz, A.J. and R.L. Penn, *Reduction of crystalline iron(III) oxyhydroxides using hydroquinone: influence of phase and particle size.* Geochem. Trans., 2005. **6**(3): p. 60-66.

87.   Madden, A.S. and M.F. Hochella, Jr., *A test of geochemical reactivity as a function of mineral size: Manganese oxidation promoted by hematite nanoparticles.* Geochim. Cosmochim. Acta, 2005. **69**(2): p. 389-398.

88.   Madden, A.S., M.f. Hochella, Jr.;, and T.P. Luxton, *Insights for size-dependent reactivity of hematite nanomineral surfaces through Cu^{2+} sorption.* Geochim. Cosmochim. Acta, 2006. **70**: p. 4095-4104.

89.   Tratnyek, P.G. and R.L. Johnson, *Nanotechnologies for environmental cleanup.* Nano Today, 2006. **1**(2): p. 44-48.

90.   Brant, J., H. Lecoanet, and M.R. Wiesner, *Aggregation and deposition characteristics of fullerene nanoparticles in aqueous systems.* Journal of Nanoparticle Research, 2005. **7**: p. 545-553.

91.   Prasher, R., P.E. Phelan, and P. Bhattacharya, *Effect of aggregation kinetics on the thermal conductivity of nanoscale colloidal solutions (nanofluid).* Nano Letters, 2006. **6**(7): p. 1529-1534.

92.   Dunphy Guzman, K.A., M.P. Finnegan, and J.F. Banfield, *Influence of surface potential on aggregation and transport of titania nanoparticles.* Environmental Science and Technology, 2006. **40**(24): p. 7688-7693.

93.   Adams, L.K., D.Y. Lyon, and P.J.J. Alvarez, *Comparative eco-toxicity of nanoscale TiO_2, SiO_2, and ZnO water suspensions.* Water Research, 2006. **40**: p. 3527-3532.

94.   Nurmi, J.T., et al., *Characterization and properties of metallic iron nanoparticles: Spectroscopy, electrochemistry, and kinetics.* Environ. Sci. Technol., 2005. **39**: p. 1221-1230.

95.   Vikesland, P.J., et al., *Particle size and aggregation effects on magnetite reactivity towards carbon tetrachloride.* Environmental Science and Technology, 2007. **41**(15): p. 5277-5283.

96.   Amonette, J.E., et al., *Dechlorination of carbon tetrachloride by Fe(II) associated with goethite.* Environ. Sci. Technol., 2000. **34**: p. 4606-4613.

97.   Anderson, M.A., M.I. Tejedor-Tejedor, and R.R. Stanforth, *Influence of aggregation on the uptake kinetics of phosphate by goethite.* Environ. Sci. Technol., 1985. **19**: p. 632-637.

98.   Hansel, C.M., et al., *Secondary mineralization pathways induced by dissmilatory iron reduction of ferrihydrite under advective flow.* Geochimica et Cosmochimica Acta, 2003. **67**(16): p. 2977-2992.

99.   Pedersen, H.D., et al., *Fast transformation of iron oxyhydroxides by the catalytic action of aqueous Fe(II).* Geochimica Et Cosmochimica Acta, 2005. **69**(16): p. 3967-3977.

100.   Pedersen, H.D., D. Postma, and R. Jakobsen, *Release of arsenic associated with the reduction and transformation of iron oxides.* Geochimica et Cosmochimica Acta, 2006. **70**(16): p. 4116-4129.

101.   Tronc, E., et al., *Transformation of ferric hydroxide into spinel by Fe(II) adsorption.* Langmuir, 1992. **8**(1): p. 313-319.

102.   Williams, A.G.B. and M.M. Scherer, *Spectroscopic evidence for Fe(II)-Fe(III) electron transfer at the Fe oxide-water interface.* Environmental Science and Technology, 2004. **38**(18): p. 4782-4790.

103.   Larese-Casanova, P. and M.M. Scherer, *Fe(II) sorption on hematite: New insights based on spectroscopic measurements.* Environ. Sci. Technol., 2007. **41**: p. 471-477.

104.   Hansel, C.M., S.G. Benner, and S. Fendorf, *Competing Fe(II)-induced mineralization pathways of ferrihydrite.* Environmental Science and Technology, 2005. **39**: p. 7147-7153.

105.   Silvester, E., et al., *Redox potential measurements and Mössbauer spectrometry of Fe^{II} adsorbed onto Fe^{III} (oxyhdr)oxides.* Geochim. Cosmochim. Acta, 2005. **69**(20): p. 4801-4815.

106.   Mulvaney, P., et al., *Charge trapping in the reductive dissolution of colloidal suspensions of iron(III) oxides.* Langmuir, 1988. **4**: p. 1206-1211.

107.   Mulvaney, P., et al., *Dynamics of interfacial charge transfer in iron(III) oxide colloids.* J. Phys. Chem., 1988. **92**: p. 6732-6740.

108.   Mulvaney, P., et al., *Effect of the ζ potential on electron transfer to colloidal iron oxides.* Langmuir, 1990. **6**: p. 555-559.

109.   Schwertmann, U. and R.M. Cornell, *Iron Oxides in the Laboratory: Preparation and Characterization*. 2nd ed. 2000, New York: Wiley-VCH. 188.

110.   Burleson, D.J. and R.L. Penn, *Two-step growth of goethite from ferrihydrite.* Langmuir, 2006. **22**: p. 402-409.

111.   Penn, R.L., J.J. Erbs, and D.M. Gulliver, *Controlled growth of alpha-FeOOH nanorods by exploiting oriented aggregation.* Journal of Crystal Growth, 2006. **293**: p. 1-4.

112.   Phenrat, T., et al., *Aggregation and sedimentation of aqueous nanoscale zerovalent iron dispersions.* Environ. Sci. Technol., 2007. **41**: p. 284-290.

113.   Saleh, N., et al., *Adsorbed triblock copolymers deliver reactive iron nanoparticles to the oil/water interface.* Nano Letters, 2005. **5**: p. 2489-2494.

114.   Murad, E. and J. Cashion, *Mossbauer Spectroscopy of Environmental Materials and their Industrial Utilization*. 2004: Kluwer Academic Publishers.

115.   Nikolaev, V.I., A.M. Shipilin, and I.N. Zakharova, *On estimating the nanoparticle size with the help of the Mössbauer effect.* Physics of the Solid State, 2001. **43**(8): p. 1515-1517.

116.   Yen, S.T., S.P. Liu, and D.W. Kolpin, *Analysis of nitrate in near-surface aquifers in the midcontinental United States: An application of the inverse hyperbolic sine Tobit model.* Water Resources Research, 1996. **32**(10): p. 3003-3011.

117.   Verwey, E.J.W. and J.T.G. Overbeek, *Theory of the Stability of Lyophobic Colloids*. 1948, Amsterdam: Elsevier. 216.

118.   Li, X.-Y. and B.E. Logan, *Permeability of fractal aggregates.* Water Research, 2001. **35**(14): p. 3373-3380.

119.   Berne, B.J. and R. Pecora, *Dynamic Light Scattering: With Applications to Chemistry, Biology and Physics*. 2000, Dover, NY: Wiley.

120.   Savage, N. and M.S. Diallo, *Nanomaterials and water purification: Opportunities and challenges.* Journal of Nanoparticle Research, 2005. **7**: p. 331-342.

121.   Zhang, H., et al., *Enhanced adsorption of molecules on surfaces of nanocrystalline particles.* J. Phys. Chem. B, 1999. **103**: p. 4656-4662.

122.   Mayo, J.T., et al., *The effect of nanocrystalline magnetite size on arsenic removal.* Science and Technology of Advanced Materials, 2007. **8**: p. 71-75.

123.   Villalobos, M., M.A. Trotz, and J.O. Leckie, *Variability in goethite surface site density: Evidence from proton and carbonate sorption.* Journal of Colloid and Interface Science, 2003. **268**: p. 273-287.

124.   Rustad, J.R. and A.R. Felmy, *The influence of edge sites on the development of surface charge on goethite nanoparticles: A molecular dynamic investigation.* Geochim. Cosmochim. Acta, 2005. **69**(6): p. 1405-1411.

125.   Gaboriaud, F. and J.-J. Ehrhardt, *Effects of different crystal faces on the surface charge of colloidal goethite (α-FeOOH) particles: An experimental and modeling study.* Geochimica et Cosmochimica Acta, 2003. **67**(5): p. 967-983.

126.   Klein, C. and C.S.J. Hurlbut, *Manual of Mineralogy*. 1999, New York: Wiley.

127.   Hansel, C.M., S.G. Benner, and S. Fendorf, *Competing Fe(II)-induced mineralization pathways of ferrihydrite.* Environmental Science & Technology, 2005. **39**: p. 7147-7153.

128.   Bowell, R.J., *Sorption of arsenic by iron oxides and hydroxides in soils.* Applied Geochemistry, 1994. **9**: p. 279-286.

129.   Ulrich, H.J. and A.T. Stone, *Oxidation of chlorophenols adsorbed to manganese oxide surfaces.* Environmental Science & Technology, 1989. **23**(4): p. 421-428.

130.   Pecher, K., S.B. Haderlein, and R.P. Schwarzenbach, *Reduction of polyhalogenated methanes by surface-bound Fe(II) in aqueous suspensions of iron oxides.* Environmental Science & Technology, 2002. **36**(8): p. 1734-1741.

131.   Di-Ruggiero, J. and A.M. Gounot, *Microbial manganese reduction mediated by bacterial strains isolated from aquifer sediments.* Microb. Ecol., 1990. **20**: p. 53-63.

132.   Lovley, D.R. and E.J.P. Phillips, *Novel mode of microbial energy metabolism: organic carbon oxidation coupled to dissimilatory reduction of iron or manganese.* Applied and Environmental Microbiology, 1988. **54**(6): p. 1472-1480.

133.   Widerlund, A., Ingri, J., *Redox cycling of iron and manganese in sediments of the Kalix River estuary, Northern Sweden.* Aquatic Geochemistry, 1996. **2**(2): p. 185-201.

134.   van der Zee, C., et al., *A Mossbauer spectroscopic study of the iron redox transition in eastern Mediterranean sediments.* Geochimica et Cosmochimica Acta, 2005. **69**(2): p. 441-453.

135.   Stollenwerk, K.G., *Geochemical interactions between constituents in acidic groundwater and alluvium in an aquifer near Globe, Arizona.* Applied Geochemistry, 1994. **9**(4): p. 353-369.

136.   Villinski, J.E., et al., *In situ spectroscopic and solution analyses of the reductive dissolution of MnO2 by Fe(II).* Environmental Science & Technology, 2001. **35**(6): p. 1157-1163.

137.   Villinski, J.E., J.E. Saiers, and M.H. Conklin, *The effects of reaction-product formation on the reductive dissolution of MnO2 by Fe(II).* Environmental Science & Technology, 2003. **37**(24): p. 5589-5596.

138. Postma, D., *Concentration of Mn and separation from Fe in sediments - I. Kinetics and stoichiometry of the reaction between birnessite and dissolved Fe(II) at 10C.* Geochimica et Cosmochimica Acta, 1985. **49**: p. 1023-1033.

139. Postma, D. and C.A.J. Appelo, *Reduction of Mn-oxides by ferrous iron in a flow system: Column experiment and reactive transport modeling.* Geochimica Et Cosmochimica Acta, 2000. **64**(7): p. 1237-1247.

140. Krishnamurti, G.S.R. and P.M. Huang, *Influence of manganese oxide minerals on the formation of iron oxides.* Clays and Clay Minerals, 1988. **36**(5): p. 467-475.

141. Eary, L.E. and D. Rai, *Kinetics of chromium(III) oxidation to chromium(VI) by reaction with manganese-dioxide.* Environmental Science & Technology, 1987. **21**(12): p. 1187-1193.

142. Laha, S. and R.G. Luthy, *Oxidation of aniline and other primary aromatic amines by manganese dioxide.* Environ. Sci. Technol., 1990. **24**(3): p. 363-373.

143. Amacher, M.C. and D.A. Baker, *Redox reactions involving chromium, plutonium, and manganese in soils*, in *Institute for research on land and water resources*. 1982, The Pennsylvania State University: University Park, PA.

144. McCobb, T.D., et al., *Phosphorus in a ground-water contaminant plume discharging to Ashumet Pond, Cape Cod, Massachusetts.* U.S. Geological Survey Water Resources Investigations Report 02-4306, 1999: p. 70p.

145. Fortune, W.B. and M.G. Mellon, *Determination of iron with o-phenanthroline - A spectrophotometric study.* Industrial and Engineering Chemistry-Analytical Edition, 1938. **10**: p. 0060-0064.

146. Tamura, H., et al., *Spectrophotometric determination of iron(II) with 1,10-phenanthroline in presence of large amounts of iron(III).* Talanta, 1974. **21**(4): p. 314-318.

147. Morgan, J.J. and W.S. Stumm, *Analytical chemistry of aqueous manganese.* Journal of the American Water Works Association, 1965. **57**(1): p. 107-119.

148. Abel, R., *Scavenging of particulate and dissolved lead compounds by coprecipitation with manganese oxyhydroxides*, in 1998, Virginia Tech.

149. Coulston, G.W., E.A. Thompson, and N. Herron, *Characterization of VPO catalysts by X-ray photoelectron spectroscopy.* Journal of Catalysis, 1996. **163**(1): p. 122-129.

150. Hadnadjev, M., et al., *The iron oxidation state in Mg-Al-Fe mixed oxides derived from layered double hydroxides: An XPS study.* Applied Surface Science, 2008. **254**(14): p. 4297-4302.

151. Cornell, R.M. and U. Schwertmann, *The Iron Oxides: Structure, Properties, Reactions, Occurrence, and Uses.* 2003, New York: VCH.

152. Morgan, J.J. and W. Stumm, *Colloid-Chemical Properties of Manganese Dioxide.* Journal of Colloid Science, 1964. **19**(4): p. 347-&.

153. Morup, S., H. Topsoe, and J. Lipka, *Modified theory for Mossbauer spectra of superparamagnetic particles: Application to Fe_3O_4.* Journal de Physique, Colloque, 1976. **6**: p. 287-290.

154. Tamaura, Y., K. Ito, and T. Katsura, *Transformation of gamma-FeO(OH) to Fe_3O_4 by adsorption of iron(II) ion on gamma-FeO(OH).* Journal of the Chemical Society-Dalton Transactions, 1983(2): p. 189-194.

155. Cudennec, Y. and A. Lecerf, *Topotactic transformations of goethite and lepidocrocite into hematite and maghemite.* Solid State Sciences, 2005. **7**(5): p. 520-529.